Shape Control and Functional Properties of Copper Chalcogenide Colloidal Nanocrystals

Wenhua Li

Programa de Doctorat en Física

Shape Control and Functional Properties of Copper Chalcogenide Colloidal Nanocrystals

Tesis que presenta Wenhua Li
per obtar al títol de Doctor per la Universitat de Barcelona

Directors de la tesis:
Dr. Andreu Cabot Codina
Professor agregat

Tutor de la tesis:
Dr. Andreu Cabot Codina

Departament d'Electrònica
Grup Materials Electrònics i Energia (M-2E)
Institut de Recerca en Energia de Catalunya (IREC)

Content

Acknowledgements

Undertaking this PhD has been a truly life-changing experience for me, upon which many people have contributed and given their support. Hence, this special section is dedicated to all the people who made possible the success of this scientific project and who gave me almost four wonderful and unforgettable years.

My gratitude goes first to my research supervisor ***Dr. Andreu Cabot***, Group Leader of the Functional Nanomaterials group. He led me into the world of material chemistry, gave me the first view of the research and introduced me to the concept and method about how to make a research. I was blessed in the four years, with his guidance, encouragement, unreserved help, hospitality, motivation, enthusiasm, immense knowledge, invaluable technique and editorial advice, which really supported me through my whole PhD studies. His broad-mindedness and his professional qualities have been of fundamental help for my whole thesis, even for my whole life. I also want to thank him giving me so much freedom in which direction to go with my research and inspiring me with his original understanding and ideas. Not only in science but also in life experience, his cordial help started from the first day of this thesis and never stopped until the end of this thesis.

I gratefully thank Prof. Ramon A. Alvarez Puebla, Dr. Jessica Rodríguez-Fernández and Dr Albert Fiquerola for accepting to refer and judge this manuscript as members of my PhD jury. I would like to thank Prof. Alejandro Pérez Rodríguez, Prof. Dr. Jordi Arbiol and Dr. Javier Rubio kindly to be substitutes of members of my PhD jury.

I must also express my deepest gratitude and sincere thanks to all of the members in the past and present of Functional Nanomaterials group, Pablo, Maria, Alexey, Jiandong, Doris, Raquel,

Alex, Joost, Zhishan, Silvia, Ariadna, Joana, Jaume. They gave me a lot of instructions and technique support during my experiments. I feel very lucky and glad to have worked with these kind people.

I am very thankful to Alexey and Maria for their enormous help during these four years of my PhD study with discussions about synthesis. I did the first colloidal synthesis under Maria's patient guidance. It's because of the inspiring discussions from Alexey, I could engage my curiosity and passion towards the new synthetic strategy. I really enjoy the great benefit of his instructions concerning chemical synthesis.

I would like to thank Pablo for his kindly help to prepare the complicated documents for PhD registration in the first year. I thank Jiandong for XPS measurements and analysis. I would like thank Doris for the great help of TEM and SEM measurements, and also I appreciate Alex for the films preparation. Great gratitude goes to Raquel for purchasing the glasses for me and taking care the waste in the lab for so long time.

I wish to express my acknowledgment to all the people in IREC, Serveis Cientificotècnics and UB who were not part of our group but helped me a lot. A special acknowledgement mentions to Jordi and Reza, the TEM people. Their excellent work has made an invaluable contribution towards my PhD study. Without their amazing TEM images and thorough analysis of the crystallographic structures, my papers probably could not be published in such highly respected journals. Thank you so much for all the efforts!

My most sincere thanks go to all the professors who gave me precious chance to make a short stay in their group: Prof. Jochen Feldmann and Prof. Wolfgang Parak. Also special gratitude goes to all the people in their groups who showed me around in the lab and helped me to adapt to everything there.

I am also appreciative of the financial support I received through PhD fellowship from IREC. I gratefully acknowledge the Spanish government as well. Without their financial support provided for my PhD studies, I could not achieve this work.

I would like to thank the Chinese community in IREC, Jiandong, Weijie, Feng, Zhishan, Haibing, Xianyun, and Xuelian. I really appreciate for the happy lunch time everyday with your accompany. Special gratitude goes to Weijie and Haibing, thank you so much for your support behind me in life; I will never forget the food you cooked for me when I was terribly busy in the lab until very late.

The last but not the least, I am deeply indebted to my parents and my sister. Their never-ending support is a powerful source of inspiration and energy for me to keep going. They always believe in me and encourage me to follow my dreams. 我爱你们，亲爱的爸爸妈妈和老妹！

List of Publications

A complete list of the author's publications (as first author), up dated on July 18th is included in the Curriculum Vitae.

1. **W. Li**, R. Zamani, P. Rivera-Gil, B. Pelaz, M. Ibáñez, D. Cadavid, A. Shavel, R. A. Alvarez-Puebla, W. J. Parak, J. Arbiol, and A. Cabot; *"CuTe Nanocrystals: Shape and Size Control, Plasmonic Properties, and Use as SERS Probes and Photothermal Agents"*; *J. Am. Chem. Soc.*, **2013**, 135, 7098-7101.

2. **W. Li**, R. Zamani, M. Ibáñez, D. Cadavid, A. Shavel, J. R. Morante, J. Arbiol, and A. Cabot; "*Metal Ions to Control the Morphology of Semiconductor Nanoparticles: Copper Selenide Nanocube"*; *J. Am. Chem. Soc.,* **2013**, 135, 4664-4667.

3. **W. Li**, A. Shavel, R. Guzman, J. Rubio-Garcia, C. Flox, J. Fan, D. Cadavid, M. Ibáñez, J. Arbiol, and A. Cabot; *"Morphology Evolution of $Cu_{2-x}S$ Nanoparticles: From Spheres to Dodecahedrons"*; *Chem. Commun.*, 2011, 47, 10332-10334.

The following articles are not published yet and the author contributed as co-authors.

1. **W. Li**, M. Ibañez, J. Rubio-Garcia, J. Ramon Morante, and A. Cabot; *"Colloidal Synthesis and Functional Properties of Quaternary Cu-Based Semiconductors: $Cu_2HgGeSe_4$"* Under Review**.**
2. **W. Li**, M. Ibañez, D. Cadavid, J. Ramon Morante, and A. Cabot; *"I_2-II-IV-VI_4 Nanoparticles: The case of $Cu_2HgSnSe_4$",* submitted.

3. M. Ibáñez, D. Cadavid, U. Anselmi-Tamburini, R. Zamani, S. Gorsse, **W. Li,** A. Shavel, A. M. López, J. Arbiol, J. R. Morante, and A. Cabot; "*Colloidal Synthesis and Thermoelectric Properties of Cu_2SnSe_3 Nanocrystals*", *J. Mater. Chem. A,* **2013***,* 1, 1421-1424.

4. M. Ibáñez**,** D. Cadavid, U. Anselmi-Tamburini, R. Zamani, S. Gorsse, **W. Li**, A. Shavel, A. M. López, J. Arbiol, J. R. Morante, and A. Cabot; "*Crystallographic Control at the Nanoscale to Enhance Funcionality: Polytypic Cu_2GeSe_3 Nanoparticles as Thermoelectric Materials*", *Chem. Mater.*, **2012**, 24, 4615-4622.

5. M. Ibáñez, R. Zamani, **W. Li**, A. Shavel, J. Arbiol, J. R. Morante, and A. Cabot; "*Extending the Nanocrystal Synthesis Control to Quaternary Compositions*", *Cryst. Growth. Des.*, **2012**, 12, 1085-1090.

6. M. Ibáñez, R. Zamani, A. LaLonde, D. Cadavid, **W. Li**, A. Shavel, J. Arbiol, J. R. Morante, S. Gorsse, G. J. Snyder, and A. Cabot; "*$Cu_2ZnGeSe_4$ Nanocrystals: Synthesis and Thermoelectric Properties***",** *J. Am. Chem. Soc.,* **2012**, 134, 4060-4063.

7. M. Ibáñez, D. Cadavid, R. Zamani, N. García-Castelló, V. Izquierdo-Roca, **W. Li**, A. Fairbrother, J. D. Prades, A. Shavel, J. Arbiol, A. Pérez-Rodríguez, J. R. Morante, and A. Cabot; "*Composition Control and Thermoelectric Properties of Quaternary Chalcogenide Nanocrystals: The Case of Stannite $Cu_2CdSnSe_4$*", Chem. Mater., **2012**, 24, 562-570.

8. M. Ibáñez, J. Fan, **W. Li**, D. Cadavid, R. Nafria, A. Carrete, and A. Cabot; *"Means and limits of control of the shell parameters in hollow cadmium chalcogenides obtained by the Kirkendall effect", Chem. Mater.,* **2011**, 23, 3095-3104.

Preface

This PhD thesis is based on research work performed in Catalonia Energy Research Institute (IREC) and University of Barcelona. It has embraced the main topic of the studies on preparation and functional properties of copper chaclcogenide nanocrystals, namely copper sulfide, copper selenide and copper telluride which present in the Chapter 3, Chapter 4 and Chapter 5, respectively. Additionally, a general introduction of the nanomaterials and their applications based on the optical properties is provided (Chapter 1). In the systemic research of these compounds, the totally new procedures were proposed for each of them (Chapter 2) and it comes in various shapes and size. These size and shape-controlled nanocrystals demonstrated potential interest in applications. In this thesis, copper sulfide is used as cathodes in all-vanadium redox flow batteries. For copper telluride, it shows novel performance as SERS probes and photothermal therapy agent.

Summary of Results

The control at the nanoscale of the composition and morphology of copper chalcogenides is especially interesting, because of their stoichiometry-dependent properties and their ample range of applications which is the main part of my work done during the last three years. The objective of this thesis was to obtain shape-controlled nanocrystals with narrow size distribution via the colloidal synthesis method and exploring their novel applications based on the fundamental research.

The high quality Cu_xS nanocrystals were studied as the first system (Chapter 3) and the profound understanding and skills to prepare colloidal nanocrystals has been obtained and improved. It revealed a very simple synthetic route not only for the systematic investigation on the size control of the copper sulfide nanodisks which have drawn considerable attentions as one of the nanocrystalline semiconductors with lamellar nanostructure and anisotropic features but also for studying the influence of different stoichiometric ratios on the shape of copper sulfide nanocrystals. TEM analysis shows that the monodisperse Cu_xS nanospheres with an average size of 7.3±0.7nm were obtained in the presence of dodecanethiol (DDT) at the low Cu precursor concentration. The replacement of the DDT with di-tert-butyl disulfide (TBDS) induced the formation of nanodisks at the same condition. An increase of the Cu precursor concentration in the growth solution resulted in the formation of tetradecahedral and dodecahedral nanocrystals. As determined by XRD, these nanodisks had a similar composition close to $Cu_{1.78}S$ as spherical nanocrystals, however, the tetradecahedral and dodecahedral nanocrystals were characterized with a composition close to $Cu_{1.96}S$ as deduced from their djurleite crystal phase. An oriented attachment was proposed as partial growth mechanism which allows an accurate control of the

size and morphology of $Cu_{2-x}S$ nanocrystals, from spheres and disks to tetradecahedrons and dodecahedrons by tuning the precursor concentration from 0.05 M to 1.0 M and reaction conditions. In particular, dodecahedrons with different size (from 53 nm to 155 nm in longer axis) can be easily prepared by either elongating the reaction time from 20 min to 60min or slightly changing the Cu precursor concentration from 0.8M to 1M. These shape-controlled crystals can be used as cathodes in all-vanadium redox flow batteries and it showed a significant improvement of the cathodic reaction reversibility, especially the dodecahedrons.

Morphology is a key parameter in the design of novel nanocrystals and nonomaterials with controlled functional properties. In the second system studied (Chapter 4), Cu_xSe nanocrystals were obtained basically by the reaction of CuCl with an excess of selenium precursor (SeO_2-ODE) in the presence of hexadecylamine (HDA). The Cu_xSe nanocubes with mean edge length of 17 nm ± 0.9 nm were synthesized in the presence of Al $(NO_3)_3$. The role of various metal ions on shape of Cu_xSe nanocrystals was discussed during the synthesis and it demonstrated the potential of foreign metal ions to tune the morphology of colloidal semiconductor Cu_xSe nanoparticles. The underlying mechanism was illustrated by preparing copper selenide nanocubes in the presence of Al ions whereas there was no any Al detected on the surface or within the final cubes. The morphology control is proved to be thermodynamically directed during the ripening regime and it exemplified the shape-direction of semiconductor nanocrystals by metal ions for the first time. Of particular interest is their potential as a platform to produce cubic nanoparticles with different composition by cation exchanges which was exemplified by the production of Ag_2Te nanocubes. The plasmonic properties of the obtained nanocubes were further characterized and it demonstrated the strong plasmonic absorption peak at 950 nm.

The last research system presented in this thesis is about Cu_xTe nanocrystals. A reproducible procedure to prepare highly monodisperse copper telluride nanocubes, nanoplates and nanorods was presented in Chapter 5. The procedure is based on the reaction of a copper salt with trioctylphosphine telluride (TOP-Te) in the presence of Lithium bis (trimethylsilyl) amide ($LiN(SiMe_3)_2$), trioctylphosphine (TOP), trioctylphosphine oxide (TOPO) and oleylamine (OLA). The high reaction temperature as 220 °C was found to be necessary to obtain cube-shaped NPs with narrow size distributions. By tuning the precursor ratio of Cu to Te, the size of these nanocubes could be controlled in the range between 10 and 20 nm. When decreasing the reaction temperature to 190 °C and the growth time to 15 min, highly homogeneous copper telluride nanoplates were produced. An increase of the TOP concentration from 0.13 mL to 0.75 mL resulted in the formation of nanorods. Control experiments were carried out to make clear the role of $LiN(SiMe_3)_2$ and it was proposed to activate the formation of a Cu-oleylamido complex, which is the actual species reacting with TOP-Te to form CuTe nanocrystals. At the same time, the Cu-oleyamido complexes and/or lithium oleylamine may play a key role stabilizing the NP surface during growth. The crystal phase of CuTe nanocubes and nanoplates cannot be determined, However, from an extensive HRTEM analysis, associated it with a tetragonal $Cu_{1.25}Te$ structure with cell parameter a=b=7.50 ± 0.05 Å and c=7.65 ± 0.05 Å. Copper telluride nanocubes and nanoplates display a strong near-infrared optical absorption at 900 nm associated to localized surface plasmon resonances. This plasmon resonance, in conjunction with their particular surface composition, can be exploited for the design of surface-enhanced Raman scattering (SERS) sensors for unconventional optical probes containing oxygen based functional groups by showing ultradetection of a group of molecules here exemplified with nile red that have no affinity for classical SERS probes (gold and silver). The enhanced SERS signal provided

by cubes is slightly larger than those of plates. This is the first time the use of Cu chalcogenide as probes for SERS application and demonstrates its potential interest in future. Furthermore, preliminary analysis of the use of copper telluride nanocubes as cytotoxic and photothermal agents is also discussed herein. The copper telluride nanocubes were firstly stabilized in water by coating them with an amphiphilic polymer before incubation. An increase in the fluorescence intensity of the nucleus is a result of plasma and nuclear membrane damage, which in turn indicates disruption of cell viability. It also represents the first exploration of the use of copper telluride nanoparticles for biological applications.

Resum en Català

Els calcogenurs de coure son uns materials de gran importància, degut a l'ampli ventall d'aplicacions que tenen. El control a la nanoescala de la seua composició i morfologia es un punt clau per explotar moltes d'aquestes propietats, degut a que aquestes depenen fortament de la estequiometria final. En aquesta tesis l'objectiu principal ha estat dissenyar síntesis per produïr nanocristalls de calcogenurs de coure binaris amb control de la forma i/o tamany. Amb els nanocristalls produits s'han explorat algunes de les aplicacions mes rellevants.

Com a primer sistema es va estudiar la producció de nanocristalls de sulfur de coure (Capítol 3). Es va desenvolupar una metedologia per sintetizar nanodiscs de Cu_xS i consecutivament es va realitzar un estudi sistemàtic sobre com controlar la seua forma i tamany. Sorprenentment, es descubrir que un parametre clau era la concentració relativa entre els precursors i el solvent durant la síntesis. Un increment de la concentració dels precursors ens va permetre obtenir nanocristalls en forma tetradecahédrica i dodecahédrica. Els patrons de difracció d'aquests nanocristalls ens van permetre determinar la seua estructura cristal·logràfica i la seua composició. Per als nanodiscs vam determinar que la seua composició era bastant propera a $Cu_{1.78}S$ tal i com teníem amb les partícules esfèriques. En canvi, els tertadecahedres i dodecahedres van resutar ser una estructura cristal·logràfica diferent, la djurleite, amb una composició propera a $Cu_{1.96}S$. Com a mecanisme de creixement es va proposar el que es coneix amb el nom d'*oriented attachment*. En el qual els nanocristalls s'uneixen en una determinada orientació per formar altres formes mes complexes. Establint les condicions en les quals es donava aquest mecanisme podíem produïr nanocristall de $Cu_{2-x}S$ amb un acurat control sobre la seua composicio i/o forma, anant de partícules esfèriques, passant per nanopartícules en forma de disc o be acanat amb partícules amb

forma tetradecahedríca o dodecahedríca. Aquest control es va aconseguir simplement variant la concrentració del precuros i les condicions de reacció. En particular, dodecahedres amb diferents tamanys van poder ser preparants simplement canviant el temps de reacció. Els cristalls més grans s'obtenien allargant el temps de reacció. Finalment es van utilizar aquests nanocristalls com a càtodes en bateries redox de vanadi i es va observar que, depenent de la forma, la reacció catòdica de reversivilitat es veia altament millorada, especialmente per als dodecahedres. Part dels resultats presentats en aquest capítol es van publicar en la revista *Chemical Communication* in 2011.

El segon sistema que es va estudiar va ser la producció de nanocristalls de seleniur de coure (Capítol 4). Fins al momento a la bibliografía hi havia reportats nanopartícules de Cu_xSe, totes elles amb formes quasi'esfèriques, en el nostre treball preteniem descubrir nous procediments per sintetitzar nanocristalls de Cu_xSe controlant la seua morfologia. Despres d'extensives proves es va descubrir que es podia controlar la forma final dels nanocristall de Cu_xSe simplement introduint ions metallics a la solucio. En particular, en presencia d'ions d'alumini es van produir nanocubs amb una longitude lateral de 17 nm ± 0.9 nm. Aquest resultat es de significativa importancia, ja que fins al moment aquesta tècnica només s´havia utilitzat per partícules metàl·liques i mai en semiconductors. Es va provar que la forma de les nanopartícules era dirigida termodinàmicament durant el que es coneix com el *Ripening regime*. Adicionalment es van estudiar les propietats plasmòniques d'aquest nanocubs. Tambe es van utilizar aquest cubs de seleniur de coure com a base per produir cubs d'altres semiconducors a través del intercanvi catiònic. Com a exemple es va produir cubs de Ag_2Te.

Finalment, es va estudiar l'últim calcogenur binari que ens quedava, el telur de coure (Capítol 5). Es va desenvolupar un mètode de síntesis per produïr nanocubs, nanoplaques i nanorods

altament monodispersos. Es va observar que els parametres clau per controlar la forma era la temperatura i la quantitat de surfacatnts. En canvi per controlar el tamany es va observar que el parametre més important era la proporció entre Cu i Te present a la solución. Concretament, a 220 °C es van aconseguir produir nanocubs, reduint la temperatura a 190 °C s'obtenien nanoplaques o nanorods en funció de la quantitat de surfactant present. Es va observar, que un increment de surfactant bloquejava el creixement d'una de les direccions, proporcionant partícules asímetriques en forma de nanorods. En el cas dels nanocubs, es va veure que el tamany dels nanocristalls podía ser controlat variant la proporció entre Cu i Te dintre del rang entre 10 i 20 nm. La fase cristal·logràfica dels nanocubs i nanoplaques produits amb aquest mètod no es va poder determinar per XRD, degut a la falta d'estructures amb les mateixes reflexions a la base de dades. En canvi, extenius anàlisis d'alta resolució de microscopia electrònica ens van permetre determinar que es tractava d'una estructura tetragonal amb els següents paràmeters de xarxa a=b=7.50±0.05 Å and c=7.65±0.05 Å. Aquest nanocristalls posseïen propietats plasmòniques amb un pic d'absorpció al voltant dels 900 nm. Les seues propietats plasmòniques, juntament amb les seues característiques superficials ens van permetre explorar la seua utilització com a sensors SERS (Surface-Enhanced Raman Scattering) per determiner grups de molècules no detectable amb alters tipus de partícules plasmòniques, com ara or o plata. L'increment dels senyal SERS obtingut amb els nanocubs va ser lleugereament més intens que no pas l'obtingut amb les nanoplaques. Per primera vegada, es van utilitar calcogenurs de coure com a sondes SERS i es va demostrar el gran potencial que tenen com tals. Adicionalment, fent ús de les seues propietats plasmòniques, els nanocristalls produits es van fer servir com a agents fototermics en cel·lules. Per aquesta darrera aplicació es van recobrir les partícules amb un polímer amfilític abans d'incubar-les a les cel·lules. Un increment en la intensitat de la fluorescencia del nucli va

resultar en un dany cel·lular. Per primera vegada es va probar la utilització de particules de telur de coure per aplicacions biològiques.

Chapter 1

General Introduction

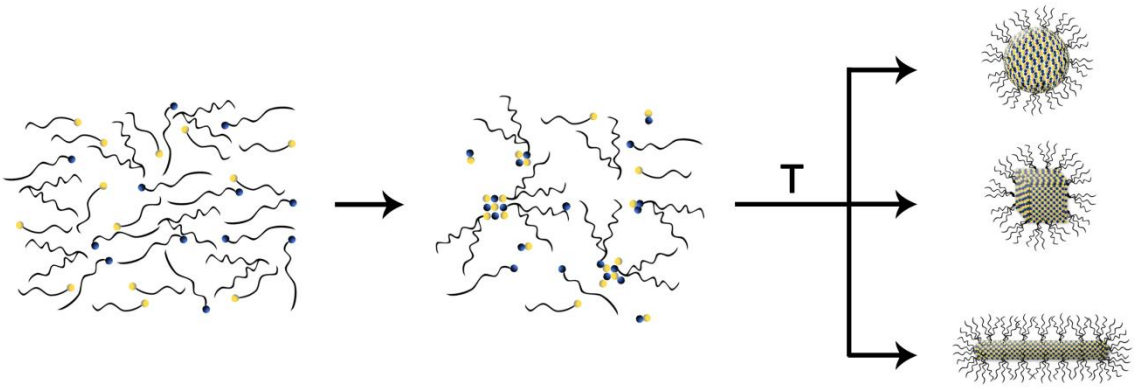

1.1 Colloidal Nanocrystals

Inorganic Colloidal Nanocrystals (NCs) are of great importance in materials physics and chemistry. They are currently being exploited as active components in a wide range of technological applications in various fields, such as composite materials[1,2] chemical sensing,[3] biomedicine,[4-6] optoelectronics,[7-9] and nanoelectronics.[10-12] In other hand, they are promising candidates as building blocks for new electronic and optical nanodevices such as quantum computers,[13-16] light-emitting diodes,[7,17,18] solar cells,[8,19,20] or lasers.[21-23]

These solids consist of hundreds to a few thousand atoms each and are stabilized by a layer of surfactant attached to their surface. Their size usually ranges from 2-3 to about 100 nm. This allows tuning of the electronic structure and the resultant optical properties and meanwhile, some related new phenomena such as size dependent band gap,[24-26] shifted plasmon resonance[27-29] can take place. When the material size is physically changed to be in the similar magnitude as the Bohr radii, quantum confinement effects are observed[30] and the new properties emerged at this

scale length can be controlled by tuning the density of their electronic states. In this regime, the adjustable properties arise through systematic transformations in the density of electronic energy levels as a function of the size of the interior, known as quantum size effects.[48,31,32]

Various shapes such as symmetry-controlled spheres, cubes, discs [33 - 38] and anisotropic geometries like rods, disks, arrows, [39] nanowires [40 - 42] and tetrapods [43 - 47] can be obtained successfully by delicately adjusting the equilibrium between thermodynamic parameters (e.g., structure stability and surface energy of the seeds) and kinetic limited growth regime (e.g., active species diffusion, facet-selective surfactant adhesion).[48,49] In addition to the common dot-shaped NCs that can be prepared with a desirable control over their size and size distribution,[50] the other shapes with higher complexity are required due to their distinguishable role in fundamental studies and technical applications.[51,52] The physical properties of these colloidal nanocrystals can be widely and easily tuned by adjusting the crystal's size, shape and composition. The combination of size- and shape-dependent physical properties and ease of fabrication and flexible processing chemistry makes NCs promising building blocks for materials with designed functions.[53,54]

1.2 Colloidal synthesis of NCs

The solution-based colloidal syntheses of various inorganic NCs has been studied extensively and gained much attention during the past two decades and impressive progress has been made towards the tailored synthesis of colloidal NCs that have well-defined structures. This method gives us the ability to control the size, shape and elemental composition of NCs with high uniformity in an ease and flexible way. In general, a typical synthesis system consists of three components: precursors, organic surfactants and solvent. NCs formation can be simply

understood as three-step processes: 1) the burst nucleation initiated by sudden increase of monomer concentration up to super-saturation levels; 2) the subsequent growth from the nuclei "seed" with progressive consumption of monomers in precursor solution; 3) the isolation of particles with a desired size from the reaction mixture. Among them, the key point is to accomplish the balance between nucleation and growth kinetically; otherwise bulk crystals or molecular species could be produced. The proper balance of these two different processes is usually addressed empirically by choosing the suitable chemicals (precursors, surfactants and solvents) combined with the optimized reaction conditions (injection temperature, reaction temperature and growth time). To be specific, the identification of suitable precursor molecules such as organometallic compounds is recognized as an important step in the generation of colloidal inorganic NCs.[55,56] The precursors need to rapidly decompose or react at the required growth temperature to yield reactive atomic or molecular species (the monomers) which is considered as the first essential prerequisite for colloidal NCs synthesis. In this case, the temperature also plays an important role not only because it benefits "dissolving" the precursor in the hot solvent, but also considered as the significant factor in determining optimal conditions for growing NCs generated only if the constituent atoms can rearrange and anneal during growth. Additionally, the colloidal nanocrystal growth is strongly dependent on the organic surfactants molecules which hold the potential for the creation of new materials[24,57] due to their propensity to adhere to the growing NCs. The typical surfactants contain both long-chain and metal coordinating groups, namely functional groups and the most used organic surfactants include alkyl phosphine oxides, alkyl phosphonic acid, alkyl phosphines, fatty acids and amines, and some nitrogen-containing aromatics. These metal coordinating groups in the surfactants bonding on the surface of NCs prevent further growth and aggregation and the other end of the surfactants

molecules extends to the solvent. So the organic surfactants determine the NCs' solubility, their ability to adhere to a substrate, and their surface charge as well. In general, they present a significant steric barrier[58] to the addition of materials to the surface of one-layer protected NCs, slowing the growth kinetics and therefore can be used to tune the kinetics of growth process of NCs. Judicious selection of surfactants for a particular synthesis is necessary. Furthermore, being able to understand the interaction between these molecules and cation, anion and crystals faces are strongly required, owing to their influence on the size, shape and structure of NCs.

1.2.1 Basics of colloidal synthesis: Nucleation event

Synthesis of high-quality colloidal semiconductor NCs is of great fundamental and technological interest based on the structural, magnetic, electronic, optical, and catalytic properties of many materials. In the regime of typical colloidal synthesis, the desirable separation in time of nucleation event from the growth of the nuclei has been demonstrated as the essentially critical parameter to obtain NCs with narrow size distribution. [50,59-62] This means that nucleation must occur on a short time scale. It may be achieved by the so-called hot-injection technique whereas the nucleation takes place rapidly right after injection of the precursor molecules into a hot solvent. In this approach, the nucleation process continues until the temperature and monomer concentration drop below a critical threshold and then only the growth event occurs at a lower temperature. The final geometry of the NCs obtained is determined not only by the growth process, but also by several parameters such as the crystalline phase of seed formed,[49] nucleation rate[61] and monomer concentration during the nucleation process. To date, the microscopic mechanism and kinetics of nucleation of real colloidal nanoparticles are still not well understood. [63] But there are some general features inherent to the homogeneous nucleation

phenomenon regarding to the spheres that have already been studied. As shown the diagram in Figure 1, in a supersaturated solution, the excess volume free energy ΔG_v (the excess free energy between a very large particle and the solute in the solution per unit volume) is a negative quantity which is proportional to r^3 (r represents the radius of a spherical particle); on the other hand, the excess surface free energy ΔG_s (the excess free energy between the surface of particle and the bulk of the solution) is a positive quantity proportional to r^2. The overall excess free energy as well as the activation energy for the nucleation process ΔG (Equation 1, γ is the solid-liquid interfacial tension, henceforth referred to as "surface energy" for the case of NCs) passes through a maximum as defined as ΔG_{crit} due to the opposite signs for ΔG_s and ΔG_v. Herein, the critical nucleus $r_c=-2\gamma/\Delta G_v$ and $\Delta G_{crit}=4\pi\gamma\ (r_c)^2/3$ can be obtained by setting $dG/dr=8\pi r\gamma+4\pi r^2\Delta G_v=0$. Hence, particles smaller than r_c will dissolve while the particle bigger will grow to reduce the free energy. For example, Peng et al. observed that the solubility of crystals increases as the size of the NCs decreases.[64]

$$\Delta G=\Delta G_s+\Delta G_v=4\pi r^2\gamma+4\pi r^3\Delta G_v/3 \qquad (1)$$

Then the rate of nucleation J can be expressed as following:

$J=A \exp(-\Delta G/kT)$ (k is the Boltzmann constant)

Considering the basic Gibbs-Thomson relationship for a non-electrolyte is given by

$\ln S=2\gamma v/kTr$ (S is the ratio of solution concentration to that of equilibrium saturation concentration at a given temperature; v is the molar volume)

Finally we can get $J=A \exp[-16\ \pi v^2\gamma^3/3k^3T^3\ (\ln S)^2]$ which clearly indicates that the rate of nucleation is determined by the three main variables, namely temperature (T), degree of supersaturation (S) and interfacial tension (γ). Among them, the nucleation rate is much more sensitive to the change of temperature compared to the growth rate because of the much higher

activation energy needed for the nucleation process than that for particle growth.[65] This makes the balance between nucleation and growth rate be tuned via changing of the temperature.

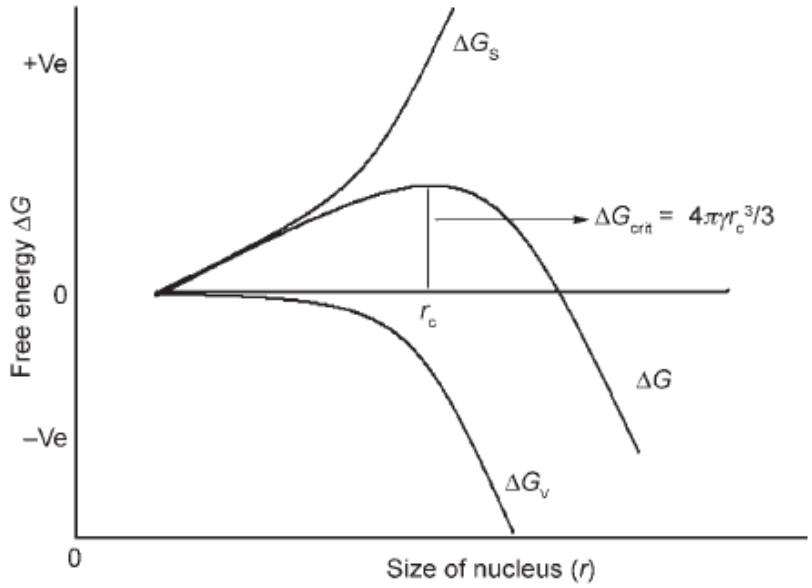

Figure 1. Free-energy diagram for nucleation processes, which explains the existence of a "critical nucleus".[66]

1.2.2 Basics of colloidal synthesis: Growth event

The NCs growth can occurs via the following two regimes: growth by consuming molecular precursors from surrounding solution known as "focusing of size distribution" and Ostwald ripening or coarsening when large particles grow at the expense of dissolving smaller ones that is also known as "defocusing of the size distribution". Because highly monodisperse NCs with narrow size distributions are always favored for different application as we stressed in previous section and the first regime of focusing the size meets this requirement, so the most of the colloidal NCs with high quality have been produced. To understand this mode, a diagram (Figure 2) illustrating the dependence of the growth rate on NCs radius can be used.

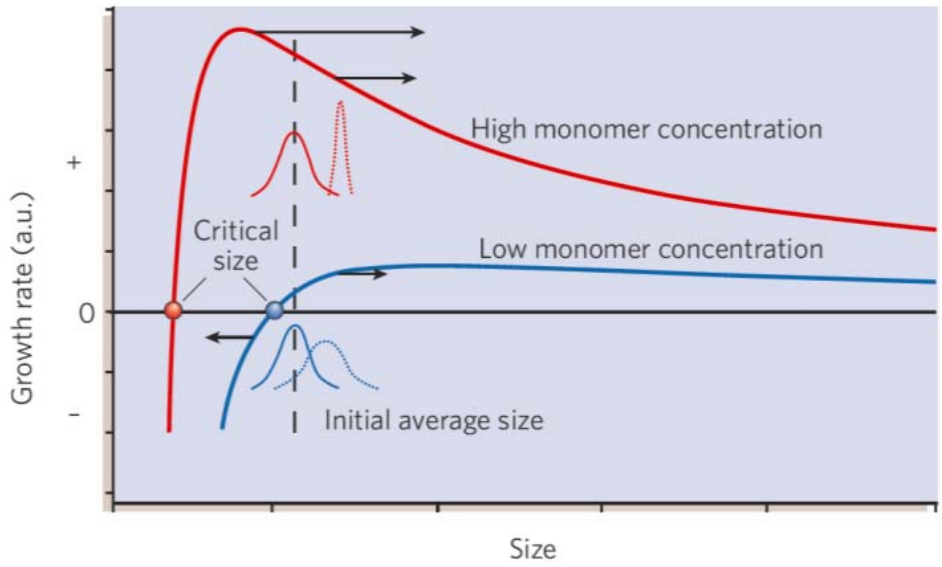

Figure 2. Growth rate dependence on the nanoparticle size for low and high concentration of monomers. [67]

In the left-hand side of the curve, negative growth rate is observed for the very small NCs. This means the crystals are not stable due to the large fraction of active surface atoms and they need to keep growing which is accompanied by the decreased surface-to-volume ratio until the critical size is achieved and the crystals become relatively stable. At this critical size, the NCs neither grow nor shrink (dG/dr=0). Herein the critical size and growth rate are determined by the equation as following:

$$r_c=2\gamma v/kTlnS \qquad (2)$$

S presents the monomer concentration as discussed before, v means the molecular volume of the NCs, k stands for the Boltzmann constant. Apparently, the critical size strongly depends on the monomer concentration. Specifically, low monomer concentration favors the larger critical size and vice versa. In this case, the depletion of monomers due to the NCs growth eventually result in the critical size falling within the distribution of NCs' average size present (blue peak, Figure 2). The resultant Oswald-ripening broadens the size distribution and occurs which means the smaller NCs with higher chemical potential evolve monomer and dissolve whereas larger NCs

consume monomer and grow. It can happen only if the addition of a monomer to a NC is a reversible process, namely a NC can both consume and release molecular species.

The concept of "focusing of size distribution" is intensively used to obtain NCs with narrow size distributions based on the previous work of Howard Reiss[68] and now has been clearly demonstrated experimentally.[69] They proposed that an optimal growth sequence involved continuous monitoring and adjustment of the monomer concentration, so that the average size present is always just slightly larger than the critical size. In other words, the high enough concentration of monomers is required for the smaller NCs to grow faster than the bigger ones and the size distribution can get narrow.

1.2.3 Nanocrystal shape and morphology engineering

As shown in the Figure 3, NCs with different shapes such as spheres, disks, plates, rods, wires, cubes, arrows, pine-tree-shaped NCs, teardrop-shaped NCs, tetrapods, star-shaped NCs and other complex morphologies can be produced in high quantities by searching for a good combination of molecular precursors, surfactants, solvent, and the reaction conditions (temperature, reaction time, etc.). These shapes are formed either under thermodynamic or kinetic control of growth process which is decided by the equilibrium between thermodynamic parameters and kinetic limited growth regime. If the particles are formed in thermal equilibrium, their shape results from minimizing the surface energy. If kinetics dominates, then the shape can be controlled by the different growth rate at selective crystal facet.

In the first case of thermodynamic growth regime, the NCs go through under a sufficient supply of thermal energy (kT) and low flux of monomer. Therefore, there are usually zero-dimensional structures with low aspect ratios are obtained because the monomers grow

isotropically from the nucleating seeds.[70] The final NCs are faceted as well; however, the low-energy facets are relatively close to each other in energy which explain them as equilibrium NCs. This mode is studied based on the Gibbs-Wulff theorem and it successes in explaining the morphologies control of many NCs. But for some advanced shapes of NCs with anisotropic geometry, they possess larger surface areas compared with equilibrium NCs. This means they only can exist in a meta-stable form and it's impossible to process under thermodynamic control. Interestingly, it can be achieved by the second theory: the kinetic control. In general, several factors including the crystalline phase of nucleating seeds, surface energy, and control of the growth regime are known to be related to anisotropic growth of NCs.[71] Among them, the crystalline phase of nucleating seeds at the nucleating stages is initially critical for directing the

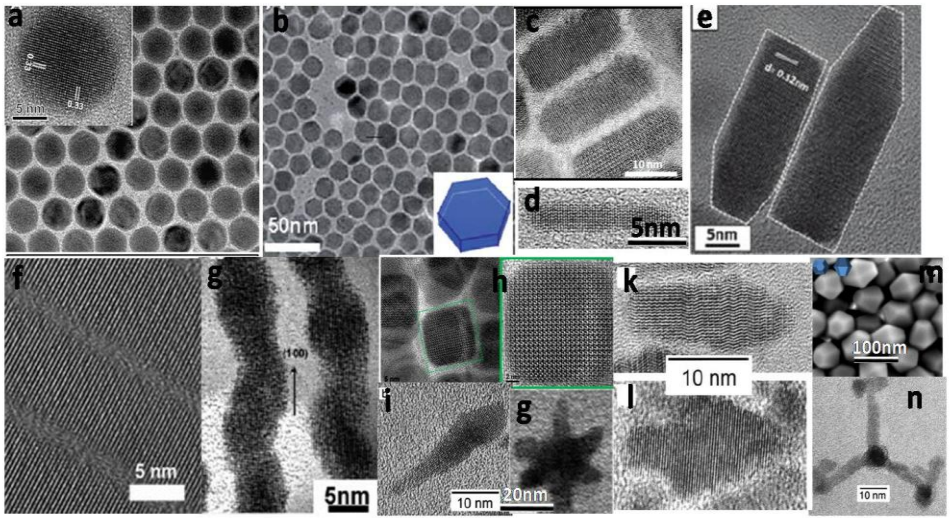

Figure 3. Microscope pictures of (a) spherical shaped, [72] (b) disk shaped,[38] (c) plate shaped,[73] (d-e) rod shaped, [39,74] (f-g) wire shaped, [36,40] (h) cube shaped,[75] (i) teardrop-shaped,[39] (g) star shaped,[36] (k) arrow shaped,[39] (l) pine-tree-shaped,[39] (m) polyhedral shaped,[76] (n) tetrapod shaped NCs.[39]

intrinsic shapes of NCs due to its characteristic unit cell structure. For example, the seeds with an isotropically cubic structure induce the isotropic growth of NCs whereas anisotropic unit cell

lead to the anisotropic growth along crystallographic reactive direction.[77,78] In the case of multi-armed

CdS rods, the tetrapods are formed at the low temperature where the formation of the four arms proceeds evenly on the four different {111} surfaces of CdS ZB core to form {001} facet of WZ-phased arms.[78,79]

The other key factor is about the intrinsic crystallographic surface energy. The growth rate of a crystal facet is closely related to the nanocrystal surface energy which renders the high-energy facets growing faster than lower ones, so that the surface energy related parameters are required to be invested intensively. The widely adjusted modulation can be contributed to the introduction of different surface capping molecules, namely organic surfactants. These molecules can influence the growth patterns of NCs by selectively adhering to a particular crystal facet. The adhesions make these non-polar lateral facets "stable" by lowering the energy effectively and therefore considerably reduce the growth rate at these facets compared to the others which leads to different crystallographic growth along these planes. For example, this effect has been observed in the anisotropic NCs growth of semiconductors such as CdSe,[39] CdTe[52] and ZnSe[45], metal like Co[80] and some rod-shaped metal oxide NCs as well.[81] In the case of hexagonally structured CdSe, rod-shaped NCs are obtained in the presence of alkylphosphonic acids which suppress the growth of the other directions except the {001}. The formation of disk shaped Co NCs[80] can attribute to the strong binding of alkylamines onto the {001} surface, and therefore growth along this direction is inhibited whereas the growth rate along the other two directions of {100} and {110} are relatively higher. This effect can be exemplified and elaborated typically on the formation of CdSe/Te tetrapods. The surface energy of cubic zincblende (ZB) ABC stacking of planes is slightly higher than the hexagonal wurtzite (WZ) ABAB stacking. After injection of

precursors, the pyramidal seeds with a ZB structure favor to form due to the kinetically preferential propensity in the high concentration of monomers. As the concentration drops, the shared {111} crystal facets between the ZB and WZ structure switch to ABAB growth in the {1000} direction of the hexagonal phase due to the "block" effect raised from the selective adhesion on the sidewall facets of the hexagonal rods. In general, nanocrystal growth rates are in turn exponentially correlated to the crystal surface energy, and therefore anisotropic nanocrystal growth can result by enhancing or reducing the surface energy by surfactant adhesion. The surfactant molecules adhered to different crystal facets can allow the NCs growth kinetics to be tuned precisely.

In the kinetic growth regime, it is also possible to create intricate shaped NCs by oriented attachment probably via dipole-induced self-assembly.[82-84] Even the detailed mechanism of orientated attachment is unclear, the coalescence of faceted NCs is observed to eliminate two high-energy facets.[36] The most common products of oriented attachment are nanorods[85] and wires.[36,40]

The NPs shape plays a distinguishable role in determining of their properties based on the quantum confinement effect.[52,86] The electronic and optical properties of the NCs can be tuned by physically changing the dimensional structures. In Figure 4, basic motifs of the zero-dimensional (spheres, cubes, and polyhedrons), 1D (rod and wire) and 2D (disk, plates, tetrapods) NCs was classified. In addition, the variation of density of state (DOS) versus energy is shown on the right to explain clearly how the shape-dependent properties behavior differently as the dimensionality changes. The confinement happens in all directions for 0D, and along two and one direction, respectively for 1D and 2D NCs.

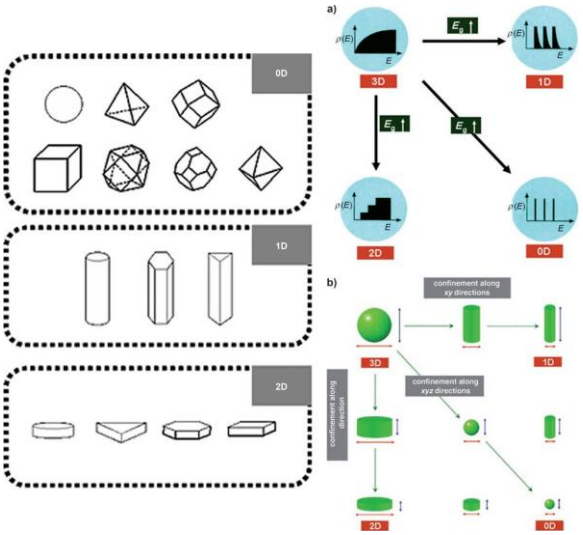

Figure 4. Basic motifs of inorganic NCs (on the left) and Shape evolution of crystals and their shape-dependent properties (on the right). a) The plot of density of state (DOS) versus energy is a continuous curve for 3D crystals and changes to a discrete line for 0D crystals. b) Confinement of 3D crystals along one- (z), two- (xy), three (xyz) directions results in 2D, 1D, and 0D NCs, respectively.

1.2.4 Metal chalcogenide NCs

Nowadays, metal chalcogenide NCs are undergoing extensive investigation for their potential applications in photovoltaic,[87, 88] optoelectronic devices,[89 - 92] biological[93 - 95] and thermoelectric[96-100] field owing to their tunable electronic and optoelectronic properties. As an example, copper-based ternary and quaternary chalcogenides have recently attracted a great deal of attention as low-cost alternatives to conventional absorber materials in photovoltaics.[101,102] Optimizing the band gap and energy levels of $Cu(InGa)Se_2$ (CIGS) via the precise control of composition and deposition conditions can increase the solar cell efficiencies up to >20 %.[88] Cu_2ZnSnS_4 (CZTS) and $Cu_2ZnSnSe_4$ (CZTSe) are emerging solar cell materials, which have similar band gaps (1.0-1.5 eV),[103] p-type conductivity and a high absorption coefficients[104] (up to 10^5 cm^{-1}) to $CuInS_2$[105] and $CuInSe_2$.[106] Their main advantage is that they do not contain indium whose natural resources are prognosticated to become scarce in the near future. Some other

novel quaternary chalcogenide such as $Cu_2CdSnSe_4$ (CCTSe)[107], CZTSe [108] and Cu_2SnSe_3,[109,110] have been found to have reasonable thermoelectric properties at medium temperatures.

In binary metal chalcogenide regime, CdS[111], CdSe,[35,112] and PdS[113], PdSe,[114] PdTe[115] have been studied extensively. Their size can be tuned by adjusting the concentrations of surfactants, reaction temperature, and duration of the particle growth which means the tunable electronic structures and optical, optoelectronic properties. They are typically used as fluorescence probes in biological applications where their high quantum yield (QY) is important for efficient sensing and imaging (Figure 5). For example, CdSe/ZnS core-shell particles exhibit a high quantum efficiency (above 50 %) at room temperature as well as a narrow size distribution (<5 %).

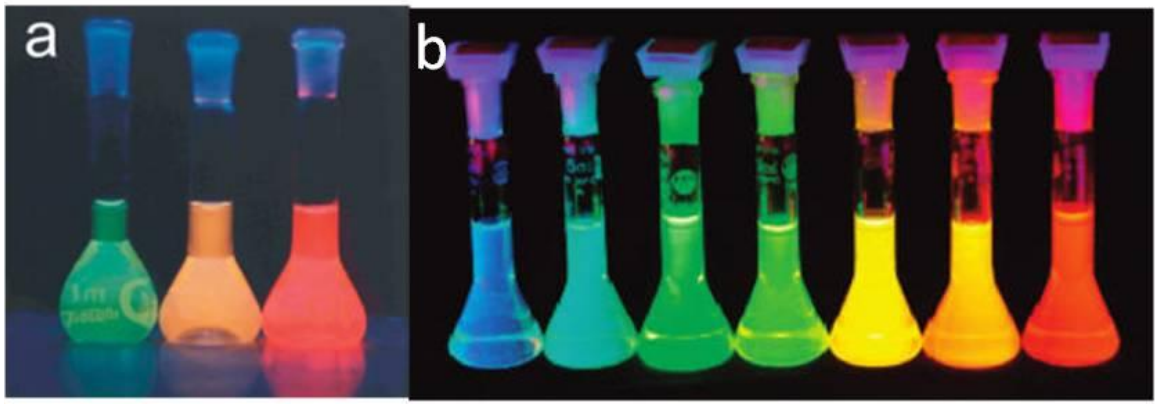

Figure 5. Size-dependent change of the photoluminescence color of colloidal solutions of NCs a) thiol-capped CdTe NCs synthesizes in aqueous solution emit green, yellow, or red light depending on size (2.5, 3.0 and 4.0 nm,correspongdingly) with room temperature quantum yield of up to 40 %; b) hexadecylamine-trioctylphosphine oxide-trioctylphosphine capped CdSe/ZnS core-shell NCs are soluble in non-polar organic solvents and emit in the whole visible spectral region depending on size with a quantum efficiency of 40-70 %.[116]

Copper-based binary chalcogenides are especially interesting type of NCs. The control at the nanoscale of the composition and morphology of these NCs results in their stoichiometry-dependent properties and their ample range of applications.[117-120] These NCs can be not only used as p-type semiconductor due to the copper vacancies in the lattice, which is the reason for their

use in applications like photovoltaic, photonic devices[121-124] and thermoelectric[125] due to the presence of copper vacancies which is highly dependent on the composition,[126] but also showed tunable optical absorption behavior due to the modified density of holes via controlling the copper deficiency as being discussed later.

1.3 Optical property of NCs

1.3.1 Absorption and Emission properties

The absorption and emission properties of semiconductor NCs are characterized by photoluminescence color, photo-stability and photoluminescence quantum yield that depends on the size, surface functionality and shape of the nanocrystal. These characteristics are raised by the absorption of a photon of particular wavelength with energy greater than band gap energy *E*g, which lead to an electron excited and leave behind an orbital hole in the valence band. Relaxation of the excited electron back to the valence band would be accompanied by the emission of a photon, a process known as radiative recombination. NCs with dimensions smaller than the Bohr exciton diameter-*a*B demonstrate quantum size effects of size-dependent absorption and fluorescence spectra with discrete electronic transitions and result in the shifted band gap in emission spectra. Figure 6a and b displays these effects for quasi-spherical NCs showing that the wavelengths of absorption and fluorescence can be tuned by nanocrystal size. The illumination of photoluminescence color and photoluminescence quantum yield can refer to Figure 5 as discussed in the previous section. The shape of NCs affects the electronic structure and distribution of electrons within the NCs by confining the exciton in different dimensions and band gap can be tuned to a precise energy depending on the dimensionality and degree of confinement (Figure 6c). Growth of NCs confined in from all three dimensions (0D) to 2D or 1D

causes a shift in emission spectra and a change in Stokes shift.[127] Elongation of short rods induces extra length dependent properties such as dipole moment, conductivity and linearly polarized emission along the c-axis whereas the diameter dependent properties such as band gap can be largely preserved.[128] Since up to half the atoms making up a NC may be on its surface as the crystal becomes smaller, the optical properties of NCs can be impacted by the surface properties as well[129] which probably arises from the modulation of surface energy states formed by the "dangling orbital".

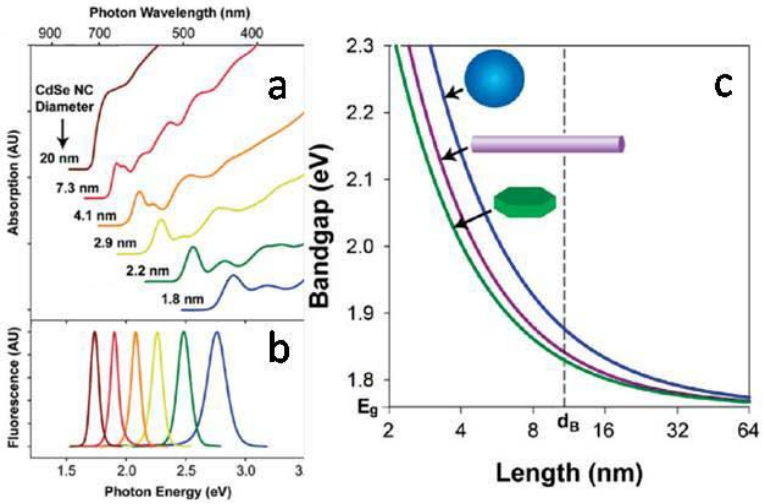

Figure 6. Absorption (a) and fluorescence (b) spectra of CdSe semiconductor NCs showing quantum confinement and size tunability. AU=arbitrary units. (c) Impact of shape on the electronic of semiconductor NCs-band gaps of CdSe quantum wells, wires, and dots are plotted against the length of the confined dimension.[130]

1.3.2 Plasmonic properties

The other manifestation of the light-matter interaction between NCs and incident light at a very fundamental level is addressed as plasmonics. It is an optical phenomenon arising from the interaction between an electromagnetic wave and the conduction electrons in the NCs. The conduction electrons are induced to oscillate upon interaction with incident light on the NCs and can keep oscillate collectively with a resonant frequency that depends on the NCs' size, shape

and composition. As noble metals are reduced in size to tens of nanometers, a new very strong absorption is observed resulting from the collective oscillation of the electrons in the conduction band. This is called surface plasmon absorption. The oscillation occurs at a frequency that can span from the visible to IR region depending on NCs size, shape and composion, etc. The strong oscillation can be achieved if the oscillation is in resonance with the incident light. At this resonant frequency, the incident light is absorbed by the nanostructure. Some of these photons will be released with the same frequency in all directions and this process is known as scattering. At the same time, some of these photons will be converted into phonons or vibrations of the lattice and this process is referred to as absorption.

Silver and gold NCs are the most commonly used materials with localized surface plasmons resonance (LSPR) mode due to their enhanced and geometrically tunable absorption and scattering across the visible and NIR ranges. For example, single Au and Ag NCs can be easily observed by eye using dark-field microscopy.[131, 132] This enables them to be attractive in a rich variety of research applications such as extremely intense labels for immunoassays,[132, 133] surface-enhanced spectroscopy[134,135] and chemical-biological sensing.[136-139]

LSPR are not limited to metal NCs and also can be achieved in semiconductor NCs with appreciable free carrier concentrations. Recently, considerable studies have been done to address the optical properties of $Cu_{2-X}Se$ or $Cu_{2-X}S$ because they can form many stoichiometries with the influence on the optical response as plasmonic in the infrared region (NIR). Burda et al. reported the NIR valance band plasmon absorption of compositionally controlled $Cu_{2-X}S$ NCs and elucidated the carrier concentration dependence.[140] A recent work by Alivisatos et al on spherical $Cu_{2-X}S$ NCs with different size smaller than 10nm interpreted LSPR arising from p-type carriers in vacancy-doped semiconductor quantum dots (QDs) and also demonstrated that by increasing

degree of copper deficiency, much more holes in the valence band of $Cu_{2-X}S$ were created which led to the emergency of an IR plasmonic peak.[141] $Cu_{2-X}Se$ has the similar optical properties as $Cu_{2-X}S$.[142] These NCs were explored for photothermal therapy,[143] although with reportedly limited photothermal transduction efficiency for $Cu_{2-x}S$.[144]

1.4 References

(1) Morris, C. A.; Anderson, M. L.; Stroud, R. M.; Merzbacher, C. I.; Rolison, D. R. *Science* **1999**, *284*, 622-624.

(2) Caruso, F. *Chem. Europ. J.* **2000**, *6*, 413-419.

(3) Kong, J.; Franklin, N. R.; Zhou, C.; Chapline, M. G.; Peng, S.; Cho, K.; Dai, H. *Science* **2000**, *287*, 622-625.

(4) Bruchez, M.; Moronne, M.; Gin, P.; Weiss, S.; Alivisatos, A. P. *Science* **1998**, *281*, 2013-2016.

(5) Chan, W. C. W.; Nie, S. M. *Science* **1998**, *281*, 2016-2018.

(6) Taton, T. A.; Mirkin, C. A.; Letsinger, R. L. *Science* **2000**, *289*, 1757-1760.

(7) Colvin, V. L.; Schlamp, M. C.; Alivisatos, A. P. *Nature* **1994**, *370*, 354-357.

(8) Huynh, W. U.; Dittmer, J. J.; Alivisatos, A. P. *Science* **2002**, *295*, 2425-2427.

(9) Klimov, V. I.; Mikhailovsky, A. A.; Xu, S.; Malko, A.; Hollingsworth, J. A.; Leatherdale, C. A.; Eisler, H. J.; Bawendi, M. G. *Science* **2000**, *290*, 314-317.

(10) Fuhrer, M. S.; Nygrd, J.; Shih, L.; Forero, M.; Yoon, Y.; Mazzoni, M. S. C.; Choi, H. J.; Ihm, J. S. G.; Zettl, A.; McEuen, P. L. *Science* **2000**, *288*, 494-497.

(11) Duan, X. F.; Huang, Y.; Cui, Y.; Wang, J. F.; Lieber, C. M. *Nature* **2001**, *409*, 66-69.

(12) Gudiksen, M. S.; Lauhon, L. J.; Wang, J.; Smith, D.; Lieber, C. M. *Nature* **2002**, *415*, 617-620.

(13) Kroutvar, M.; Ducommun, Y.; Heiss, D.; Bichler, M.; Schuh, D.; Abstreiter, G.; Finley, J. J. *Nature* **2004**, *432*, 81-84.

(14) Lee, S.; Allmen, P. V.; Oyafuso, F.; Klimeck, G. *J. Appl. Phys.* **2005**, *97*, 043706.

(15) Kawabata, S. *Sci. Tech. Adv. Mater.* **2004**, *5*, 295-299.

(16) Loss, D.; Divincenzo, D. P. *Phys. Rev. A* **1998**, *57*, 120-126.

(17) Dabbousi, B. O.; Bawendi, M. G.; Onitsuka, O.; Rubner, M. F. *Appl. Phys. Lett.* **1995**, *66*, 1316-1318.

(18) Tessler, N.; Medvedev, V.; Kazes, M.; Kan, S. H.; Banin, U. *Science* **2002**, *295*, 1506-1508.

(19) Kumar, S.; Nann, T. *J. Mater. Res.* **2004**, *19*, 1990-1994.

(20) Sun, B.; Marx, E.; Greenham, N. C. *Nano. Lett.* **2003**, *3*, 961-963.

(21) Sunder, V. C.; Eisler, H. J.; Deng, T.; Chan, Y.; Thomas, E. L.; Bawendi, M. G. *Adv. Mater.* **2004**, *16*, 2137-2141.

(22) Eisler, H. J.; Sunder, V. C.; Bawendi, M. G.; Walsh, M.; Smith, H. I.; Klimov, V. *Appl. Phys. Lett.* **2002**, *80*, 4614-4616.

(23) Chan, Y.; Steckel, J. S.; Snee, P. T.; Caruge, J. M.; Hodgkiss, J. M.; Nocera, D. G.; Bawendi, M. G. *Appl. Phys. Lett.* **2005**, *86*, 073102.

(24) Alivisatos, A. P. *Science* **1996**, *271*, 933-937.

(25) Alivisatos, A. P.; Harris, A. L.; Levinos, N. J.; Steigerwald, M. L.; Harris, L. E. *J. Chem. Phys.* **1988**, *89*, 4001-4011.

(26) Alivisatos, A. P. *J. Phys. Chem.* **1996**, *100*, 13226-13239.

(27) Eustis, S.; El-Sayed, M. A. *Chem. Soc. Rev.* **2006**, *35*, 209-217.

(28) Link, S.; El-Sayed, M. A. *J. Phys. Chem. B* **1999**, *103*, 4212-4217.

(29) Sherry, L. J.; Chang, S. H.; Schatz, G. C.; Van Duyne, R. P.; Wiley, B. J.; Xia, Y. *Nano. Lett.* **2005**, *5*, 2034-2038.

(30) Rogach, A. *Springer* **2008**.

(31) Murray, C. B.; Sun, S. H.; Doyle, H.; Betley, T. *MRS. Bull.* **2001**, *26*, 985-991.

(32) Brus, L. *J. Phys. Chem.* **1986**, *90*, 2555-2560.

(33) Ahmadi, T. S.; Wang, Z. L.; Green, T. C.; Henglein, A.; El-Sayed, M. A. *Science* **1996**, *272*, 1924-1926.

(34) Yu, Y. Y.; Chang, S.; Lee, C. J.; Wang, C. R. C. *J. Phys. Chem. B* **1997**, *101*, 6661-6664.

(35) Li, W.; Shavel, A.; Guzman, R.; Rubio-Garcia, J.; Flox, C.; Fan, J.; Cadavid, D.; Ibáñez, M.; Arbiol, J.; Cabot, A. *Chem. Commun.* **2011**, *47*, 10332-10334.

(36) Cho, K. S.; Talapin, D. V.; Gaschler, W.; Murray, C. B. *J. Am. Chem. Soc.* **2005**, *127*, 7140-7147.

(37) Chen, S.; Fan, Z.; Carroll, D. L. *J. Phys. Chem. B* **2002**,*106,*10777-10781.

(38) Shen, H.; Wang, H.; Yuan, H.; Ma, L.; Li, L. S. *Cryst. Eng. Comm.* **2012**, *14*, 555-560.

(39) Manna, L.; Scher, E. C.; Alivisatos, A. P. *J. Am. Chem. Soc.* **2000**, *122*, 12700-12706.

(40) Sun, J.; Wang, L. W.; Buhro, W. E. *J. Am. Chem. Soc.* **2008**, *130*, 7997-8005.

(41) Penn, R. L.; B, J. F. *Science* **1998**, *281*, 969-971.

(42) Banfield, J. F.; Welch, S. A.; Zhang, H.; Ebert, T. T.; Penn, R. L. *Science* **2000**, *289*, 751-754.

(43) Cozzoli, P. D.; Snoeck, E.; Garcia, M. A.; Giannini, C.; Guagliardi, A.; Cervellino, A.; Gozzo, F.; Hernando, A.; Achterhold, K.; Ciobanu, N.; Parak, F. G.; Cingolani, R.; Manna, L. *Nano. Lett.* **2006**, *6*, 1966-1972.

(44) Teng, X.; Yang, H. *Nano. Lett.* **2005**, *5*, 885-891.

(45) Cozzoli, P. D.; Manna, L.; Curri, M. L.; Kudera, S.; Giannini, C.; Striccoli, M.; Agostiano, A. *Chem. Mater.* **2005**, *17*, 1296-1306.

(46) Hu, J.; Bando, Y.; Goldberg, D. *Small* **2005**, *1*, 95-99.

(47) Milliron, D. J.; Hughes, S. M.; Cui, Y.; Manna, L.; Li, J.; Wang, L. W.; Alivisatos, A. P. *Nature* **2004**, *430*, 190-195.

(48) Burda, C.; Chen, X.; Narayanan, R.; El-Sayed, M. A. *Chem. Re*v. **2005**, *105*, 1025-1102.

(49) Jun, Y. W.; Lee, J. H.; Choi, J. S.; Cheon, J. *J. Phys. Chem. B.* **2005**, *109*, 14795-14806.

(50) Cao, M.; Lian, H.; Hu, C. *Nanoscale* **2010**, *2*, 2619-2623.

(51) Peng, Z. A.; Peng, X. *J. Am. Chem. Soc.* **2002**, *124*, 3343-3353.

(52) Manna, L.; Milliron, D. J.; Meisel, A.; Scher, E. C.; Alivisatos, A. P. *Nat. Mater.* **2003**, *2*, 382-385.

(53) Alivisatos, A. P. *Endeavour* **1997**, *21*, 56-60.

(54) El-Sayed, M. A. *Acc. Chem. Res.* **2004**, *37*, 326-333.

(55) Stuczynski, S. M.; Brennan, J. G.; Steigerwald, M. L. *Inorg. Chem.* **1989**, *28*, 4431-4432.

(56) Steigerwald, M. L. *Polyhedron* **1994**, *13*, 1245-1252.

(57) Nirmal, M.; Brus, L. *Acc. Chem. Res.* **1999**, *32*, 407-414.

(58) Murray, C. B.; Norris, D. J.; Bawendi, M. G. *J. Am. Chem. Soc.* **1993**, *115*, 8706-8715.

(59) De Mello Donega, C.; Liljeroth, P.; Vanmaekelbergh, D. *Small* **2005**, *1*, 1152-1162.

(60) Peng, Z. A.; Peng, X. G. *J. Am. Chem. Soc.* **2001**, *123*, 183-184.

(61) Shevchenko, E. V.; Talapin, D. V.; Schnablegger, H.; Kornowski, A.; Festin, O.; Svedlindh, P.; Haase, M.; Weller, H. *J. Am. Chem. Soc.* **2003**, *125*, 9090-9101.

(62) Peng, X. *Adv. Mater.* **2003**, *15*, 459-463.

(63) Auer, S.; Frenkel, D. *Nature*, **2001**, *409*, 1020-1023.

(64) Peng, X.; Manna, L.; Yang, W.; Wickham, J.; Scher, E.; Kadavanich, A. *Nature* **2000**, *404*, 59-61.

(65) Sugimoto, T. *Monodisperse Particles*.po Elsevier: **2001**.

(66) Kumar, S.; Nann. T. *Small* **2006**, *2*, 316-329.

(67) Yin, Y.; Alivisatos, A. P. *Nature* **2005**, *437*, 664-670.

(68) Reiss, H. *J. Chem. Phys*. **1951**, *19*, 482-487.

(69) Peng, X.; Wickham, J.; Alivisatos, A. P. *J. Am. Chem. Soc*. **1998**, *120*, 5343-5344.

(70) Biacchi, A. J.; Schaak, R. E. *ACS. Nano.* **2011**, *5*, 8089-8099.

(71) Lee, S. M.; Cho, S. N.; Cheon, J. *Adv. Mater.* **2003**, *15*, 441-444.

(72) Yarema, M.; Kovalenko, M. V.; Hesser, G.; Talapin, D. V.; Heiss, W. *J. Am. Chem. Soc.* **2010**, *132*, 15158-15159.

(73) Li, W. H.; Zamani, R.; Gil, P. R.; Pelaz, B.; Ibáñez, M.; Cadavid, D.; Shavel, A.; Alvarez-Puebla, R.; Parak, W.; Arbiol, J.; Cabot, A. *J. Am. Chem. Soc.* **2013**, 135, 7098-7101.

(74) Singh, A.; Geaney, H.; Laffir, F.; Ryan, K. M. *J. Am. Chem. Soc.* **2012**, *134*, 2910-2913.

(75) Li, W. H.; Zamani, R.; Ibáñez, M.; Cadavid, D.; Shavel, A.; Morante, J. R.; Arbiol, J.; Cabot, A. *J. Am. Chem. Soc.* **2013**, *135*, 4664-4667.

(76) Li, W. H.; Shavel, A.; Guzman, R.; Garcia, J. R.; Flox, C.; Fan, J. D.; Cadavid, D.; Ibáñez, M.; Arbiol, J.; Morante, J. R.; Cabot, A. *Chem. Commun.* **2011**, *47*, 10332-10334

(77) Jun, Y.; Jung, Y.; Cheon, J. *J. Am. Chem. Soc.* **2002**, *124*, 615-619.

(78) Jun, Y.; Lee, S. M.; Kang, N. J.; Cheon, J. *J. Am. Chem. Soc.* **2001**, *123*, 5150-5151.

(79) Zelaya-Angel, O.; Alvaradi-Gol, J. J.; Lozada-Morales, R.; Vargas, H.; Ferreira da Silva, A. *Appl. Phys. Lett.* **1994**, *64*, 291-294.

(80) Puntes, V. F.; Zanchet, D.; Erdonmez, C.; Alivisatos, A. P. *J. Am. Chem. Soc.* **2002**, *124*, 12874-12880.

(81) Jun, Y.; Casula, M. F.; Sim, J. H.; Kim, S. Y.; Cheon, J.; Alivisatos, A. P. *J. Am. Chem. Soc.* **2003**, *125*, 15981-15985.

(82) Tang, Z. Y.; Kotov, N. A.; Giersig, M. *Science* **2002**, *297*, 237-240.

(83) Schliehe, C.; Juarez, B. H.; Pelletier, M.; Jander, S.; Greshnykh, D.; Nagel, M.; Meyer, A.; Foerster, S.; Kornowski, A.; Klinke, C.; Weller, H. *Science* **2010,** *329*, 550-553.

(84) Liao, H. G.; Cui, L.; Whitelam, S.; Zheng, H. *Science* **2012**, *336*, 1011-1014.

(85) Li, L. S.; Walda, J.; Manna, L.; Alivisatos, A. P. *Nano. Lett.* **2002**, *2*, 557-560.

(86) Li, L. S.; Hu, J.; Yang, W.; Alivisatos, A. P. *Nano. Lett.* **2001**, *1*, 349-351.

(87) Niki, S.; Contreras, M.; Repins, I.; Powalla, M.; Kushiya, K.; Ishizuka, S.; Matsubara, K. *Prog. Photovoltaics.* **2010**, *18*, 453-466.

(88) Green, M. A.; Emery, K.; Hishikawa, Y.; Warta, W.; Dunlop, E. D. *Prog. Photovoltaics.* **2012**, *20*, 606-614.

(89) Saipulaeva*a*, L. A.; Gabibov*a*, F. S.; Mel'nikova, N. V.; Alibekov, A. G.; Kheifets, O. L.; Babushkin, A. N.; Kurochka, K. V. *J. Exp. Theor. Phys.* **2012**, *115*, 918-924.

(90) Klimov, V. I. *J. Phys. Chem. B* **2006**, *110*, 16827-16845.

(91)Klimov, V. I.; Ivanov, S. A.; Nanda, J.; Achermann, M.; Bezel, I.; McGuire, J. A.; Piryatinski, A. *Nature* **2007**, *447*, 441-446.

(92) Ai, G.; Sun, W.; Gao, X.; Zhang, Y.; Peng, L. *J. Mater. Chem.* **2011**, *21*, 8749-8755.

(93) Fan, H. M.; Olivo, M.; Shuter, B.; Yi, J. B.; Bhuvaneswari, R.; Tan, H. R.; Xing, G. C.; Ng, C. T.; Liu, L.; Lucky, S. S.; Bay, B. H.; Ding, J. *J. Am. Chem. Soc.* **2010**, *132*, 14803-14811.

(94) Delehanty, J. B.; Susumu, K.; Manthe, R. L.; Algar, W. R.; Medintz, I. L. *Analytica . Chimica. Acta.* **2012**, *750*, 63-81.

(95) Ruedas-Ramaa, M. J.; Walters, J. D.; Orte, A.; Hall, E. A. H. *Analytica. Chimica. Acta.* **2012**, *751*, 1-23.

(96) Fan, F. J.; Yu, B.; Wang, Y. X.; Zhu, Y. L.; Liu, X. J.; Yu, S. H.; Ren, Z. *J. Am. Chem. Soc.*

2011, *133*, 15910-15913.

(97) Ibáñez, M.; Cadavid, D.; Zamani, R.; García-Castelló, N.; Izquierdo-Roca, V.; Li, W.; Fairbrother, A.; Prades, J. D.; Shavel, A.; Arbiol, J.; Pérez-Rodríguez, A.; Morante, J. R.; Cabot, A. *Chem. Mater.* **2012**, *24*, 562-570.

(98) Ibáñez, M.; Zamani, R.; LaLonde, A.; Cadavid, D.; Li, W.; Shavel, A.; Arbiol, J.; Morante, J. R.; Gorsse, S.; Snyder, G. J.; Cabot, A. *J. Am. Chem. Soc.* **2012**, *134*, 4060-4063.

(99) Ibáñez, M.; Cadavid, D.; Anselmi-Tamburini, U.; Zamani, R.; Gorsse, S.; Li, W.; Shavel, A.; López, A. M.; Arbiol, J.; Morante, J. R.; Cabot, A. *Chem. Mater.* **2012**, *24*, 4615-4622.

(100) Ibáñez, M.; Gorsse, S.; Zamani, R.; Arbiol, J.; Morante, J. R.; Cabot, A. *ACS. Nano.* **2013**, *7*, 2573-2586.

(101) Todorov, T. K.; Reuter, K. B.; Mitzi, D. B. *Adv. Mater.* **2010**, *22*, 156-159.

(102) Guo, Q.; Ford, G. M.; Yang, W. C.; Walker, B. C.; Stach, E. A.; Hillhouse, H. W.; Agrawal, R. *J. Am. Chem. Soc.* **2010**, *132*, 17384-17386.

(103) Chen, S.; Gong, X. G.; Walsh, A.; Wei, S. *Appl. Phys. Lett.* **2009**, *94*, 041903.

(104) Babu, G. S.; Kumar, Y. B. K.; Bhaskar, P. U.; Raja, V. S. *J. Phys. D: Appl. Phys.* **2008**, *41*, 205305.

(105) Pan, D.; An, L.; Sun, Z.; Hou, W.; Yang, Y.; Yang, Z.; Lu, Y. *J. Am. Chem. Soc.* **2008**, *130*, 5620-5621.

(106) Koo, B.; Patel, R. N.; Korgel, B. A. *J. Am. Chem. Soc.* **2009**, *131*, 3134-3135.

(107) Liu, M. L.; Chen, I. W.; Huang, F. Q.; Chen, L. D. *Adv. Mater.* **2009**, *21*, 3808-3812.

(108) Shi, X. Y.; Huang, F. Q.; Liu, M. L.; Chen, L. D. *Appl. Phys. Lett.* **2009**, *94*, 122103.

(109) Shi, X. Y.; Xi, L. L.; Fan, J.; Zhang, W. Q.; Chen, L. D. *Chem. Mater.* **2010**, *22*, 6029-6031.

(110) Ibáñez, M.; Cadavid, D.; Anselmi-Tamburini, U.; Zamani, R.; Gorsse, S.; Li, W.; Shavel, A.; López, A. M.; Arbiol, J.; Morante, J. R.; Cabot, A. *J. Mater. Chem. A* **2013**, *1*, 1421-1431.

(111) Li, H. Q.; Wang, X.; Xu, J. Q.; Zhang, Q.; Bando, Y.; Golberg, D.; Ma, Y.; Zhai, T. Y. *Adv. Mater.* **2013**, *25*, 3017-3037.

(112) Talapin, D. V.; Rogach, A. L.; Kornowski, A.; Haase, M.; Weller, H. *Nano. Lett.* **2001**, *1*, 207-211.

(113) Abel, K. A.; Shan, J. N.; Boyer, J. C.; Harris, F.; van Veggel, F. *Chem. Mater.* **2008**, *20*, 3794-3796.

(114) Talapin, D. V.; Murray, C. B. *Science* **2005**, *310*, 86-89.

(115) Urban, J. J.; Talapin, D. V.; Shevchenko, E. V.; Murray, C. B. *J. Am. Chem. Soc.* **2006**, *128*, 3248-3255.

(116) Rogach, A. L.; Talapin, D. V.; Shevchenko, E. V.; Kornowski, A.; Haase, M.; Weller, H. *Adv. Funct. Mater.* **2002**, *12*, 653-664.

(117) Xu, J.; Zhang, W.; Yang, Z.; Ding, S.; Zeng, C.; Chen, L.; Wang, Q.; Yang, S. *Adv. Funct. Mater.* **2009**, *19*, 1759-1766.

(118) Zhao, Y.; Pan, H.; Lou, Y.; Qiu, X.; Zhu, J.; Burda, C. *J. Am. Chem. Soc.* **2009**, *12*, 4253-4261.

(119) Choi, J.; Kang, N.; Yang, H. Y.; Kim, H. J.; Son, S. U. *Chem. Mater.* **2010**, *22*, 3587-3588.

(120) Gurin, V. S.; Prokopenko, V. B.; Alexeenko, A. A.; Wang, S.; Yumashev, K. V.; Prokoshin, P. V. *Int. J. Inorg. Mater.* **2001**, *3*, 493-496.

(121) Deka, S.; Genovese, A.; Zhang, Y.; Miszta, K.; Bertoni, G.; Krahne, R.; Giannini, C.; Manna, L. *J. Am. Chem. Soc.* **2010**, *132*, 8912-8914.

(122) Choi, J.; Kang, N.; Yang, H. Y.; Kim, H. J.; Son, S. U. *Chem. Mater.* **2010**, *22*, 3586-3588.

(123) Riha, S. C.; Johnson, D. C.; Prieto, A. L. *J. Am. Chem. Soc.* **2011**, *133*, 1383-1390.

(124) Xu, J.; Zhang, W.; Yang, Z.; Ding, S.; Zeng, C.; Chen, L.; Wang, Q.; Yang, S. *Adv. Funct. Mater.* **2009**, *19*, 1759-1766.

(125) Liu, H.; Shi, X.; Xu, F.; Zhang, L.; Zhang, W.; Chen, L.; Li, Q.; Uher, C.; Day, T.; Snyder, G. J. *Nat. Mater.* **2012**, *11*, 422-425.

(126) GarcmHa, V. M.; Nair, P. K.; Nair, M. T. S. *J. Cryst. Growth* **1999**, *203*, 113-124.

(127) Hu, J.; Li, L.-S.; Yang, W.; Manna, L.; Wang, L.-W.; Alivisatos, A. P. *Science* **2001**, *292*, 2060-2063.

(128) Li, L. S.; Alivisatos, A. P. *Phy. Rev. Lett.* **2003**, *90*, 097402.

(129) Underwood, D. F.; Kippeny, T.; Rosenthal, S. J. *J. Phys. Chem. B* **2001**, *105*, 436-443.

(130) Smith, A. M.; Nie, S. M. *Acc. Chem. Res.* **2010**, *43*, 190-200.

(131) Willets, K. A.; Van Duyne, R. P. *Annu. Rev. Phys. Chem.* **2007**, *58*, 267-297.

(132) Schultz, S.; Smith, D. R.; Mock, J. J.; Schultz, D. A. *Proc. Natl Acad. Sci. USA* **2000**, *97*, 996-1001.

(133) Nam, J. M.; Thaxton, C. S.; Mirkin, C. A. *Science* **2003**, *301*, 1884-1886.

(134) Chen, Y.; Munechika, K.; Ginger, D. S. *Nano. Lett.* **2007**, *7*, 690-696.

(135) Freeman, R. G.; Grabar, K. C.; Allison, K. J.; Bright, R. M.; Davis, J. A.; Guthrie, A. P.; Hommer, M. B.; Jackson, M. A.; Smith, P. C.; Walter, D. G.; Natan, M. J. *Science* **1995**, *267*, 1629-1632.

(136) Haes, A. J.; Van Duyne, R. P. *J. Am. Chem. Soc.* **2002**, *124*, 10596-10604.

(137) Nam, J. M.; Thaxton, C. S.; Mirkin, C. A. *Science* **2003**, *301*, 1884-1886.

(138) Elghanian, R.; Storhoff, J. J.; Mucic, R. C.; Letsinger, R. L.; Mirkin, C. A. *Science* **1997**, *277*, 1078-1081.

(139) Raschke, G. *Nano. Lett.* **2003**, *3*, 935-938.

(140) Zhao, Y. X.; Pan, H. C.; Lou, Y. B.; Qiu, X. F.; Zhu, J. J.; Burda, C. *J. Am. Chem. Soc.* **2009**, *131*, 4253-4261.

(141) Luther, J. M.; Jain, P. K.; Ewers, T.; Alivisatos, P. A. *Nat. Mater.* **2011**, *10*, 361-366.

(142) Dorfs, D.; Hartling, T.; Miszta, K.; Bigall, N. C.; Kim, M. R.; Genovese, A.; Falqui, A.; Povia, M.; Manna, L. *J. Am. Chem. Soc.* **2011**, *133*, 11175-11180.

(143) Hessel, C. M.; Pattani, V. P.; Rasch, M.; Panthani, M. G.; Koo, B.; Tunnell, J. W.; Korgel, B. A. *Nano. Lett.* **2011**, *11*, 2560-2566.

(144) Li, Y. B.; Lu, W.; Huang, Q. A.; Huang, M. A.; Li, C.; Chen, W. *Nanomedicine* **2010**, *5*, 1161-1171.

Chapter 2

Cu_xM (M=S, Se, Te) nanocrystals preparation and characterization techniques

This chapter presents the main techniques used for i) preparing the copper based bimetallic nanoparticles and ii) characterizing them and the way that the respective procedures are implemented

2.1 Cu_xM (M=S, Se, Te) nanoparticles preparation

2.1.1 Cu_xS nanospheres

For the preparation of copper sulfide nanospheres, we proposed two different synthetic approaches:

(a) In a typical preparation, 0.08 g of $CuCl_2 \cdot 2H_2O$ (0.5 mmol) and 10 g of OLA were introduced inside a four-neck flask and heated to 200 ºC under an argon atmosphere. The yellowish transparent solution produced was maintained at 200 ºC for 1 h for purification, i.e. to remove oxygen, water and other low-boiling point impurities. Afterwards, the temperature was set to 220 ºC and 0.5 mL TBDS (2.5 mmol, containing 5 mmol elemental S) was injected through a septum. Solution was slowly (during few minutes) turning brownish. The mixture was maintained at the reaction temperature for up to 10 min to allow the nanoparticles growth. Then, the flask was rapidly cooled down to room temperature and the resulting nanocrystal suspension was centrifuged and the precipitate was washed and centrifuged three times with toluene and isopropanol. The nanocrystals were re-dispersed in toluene and stored in an Ar filled glove-box.

(b) Alternatively, copper sulfide nanospheres were synthesized by the procedure described as following: CuCl (50 mg; 0.50 mmol), Dodecanethiol (DDT, 1 g), Oleylamine (OLA, 1 g) and 10 g of 1,2-dichlorobenzene (DCB) was placed in a four neck flask and heated up to 150 ºC under an Argon flow until yellow transparent solution was formed. The reaction mixture was kept at that temperature for 1 h for purification. Then the solution was heated to 180 ºC and 0.5 mL (2.5 mmol, containing 5 mmol elemental S) of TBDS was injected by syringe. Solution was slowly (during few minutes) turning brownish. The reaction mixture was kept at 180 ºC during the appropriate period of time (about 1 h) to allow the nanoparticles growth. Finally the solution was cooled to room temperature. The same procedures were used to clean the particles.

2.1.2 Cu_xS nanodisks

For the synthesis of copper sulfide nanodisks, 0.08 g of $CuCl_2 \cdot 2H_2O$ (0.5 mmol) and 12 g of OLA (15 mL) were loaded into a four-neck flask and heated to 200 ºC at a rate of 17 ºC/min under an argon flow to produce a yellowish transparent solution. The solution was maintained at 200 ºC for 1 h for the purification. After that, temperature was set up to the desired values for the injection (between 180 ºC – 210 ºC) and 1ml TBDS (5 mmol, containing 10 mmol elemental S) was injected. Finally the solution was cooled down to room temperature and the resulting nanocrystal suspension was washed out with the standard precipitation/re-dispersion procedures. It is worth to mention that the control experiments under the condition of different temperatures were also carried out using the same procedure. In addition, several aliquots were extracted from the reacting solution at different times in order to study the shape and size evolution of the obtained nanocrystals.

2.1.3 Cu_xS polyhedrons

(a) Cu_xS tetradecahedral nanocrystals: the tetradecahedrons were obtained from the reaction of more copper chloride (1 mmol, 2 mmol or 5 mmol) with the same amount of di-tert-butyl disulfide (TBDS) inside a heated OLA solution. In a typical preparation, 0.85 g of $CuCl_2 \cdot 2H_2O$ (5 mmol) and 12 g of OLA were introduced inside a four-neck flask and heated to 200 ºC under an argon flow. The yellowish transparent solution produced was maintained at 200 ºC for 1 h for purification, i.e. to remove oxygen, water and other low-boiling point impurities. Afterwards, 1 ml TBDS (5 mmol, containing 10 mmol elemental S) was injected through a septum. The mixture was maintained at the reaction temperature for up to 1 h to allow the nanoparticles growth. Then, the flask was rapidly cooled down to room temperature. The nanoparticles were washed by multiple precipitation and dispersion steps using toluene as a solvent and ethanol as the precipitating agent. Here the shown synthesis procedure, characterized by a low nucleation rate as discussed as following, produced highly monodisperse nanocrystals, thus not requiring any size selection process.

(b) Cu_xS dodecahedral nanocrystals: the dodecahedrons were obtained from the reaction of much more copper chloride (8 mmol or 10 mmol) with the same amount of di-tert-butyl disulfide (TBDS) inside a heated OLA solution. In a typical preparation, 1.36 g of $CuCl_2 \cdot 2H_2O$ (8 mmol) and 12 g of OLA were introduced inside a four-neck flask and heated to 200 ºC under an argon flow. The yellowish transparent solution produced was maintained at 200 ºC for 1 h for purification, i.e. to remove oxygen, water and other low-boiling point impurities. Afterwards, 1 ml TBDS (5 mmol, containing 10 mmol elemental S) was injected through a septum. The mixture was maintained at the reaction temperature for up to 1 h to allow the nanoparticles

growth. Then, the flask was rapidly cooled down to room temperature. The nanoparticles were washed by multiple precipitation and dispersion steps using toluene as a solvent and ethanol as the precipitating agent. No additional size-selection procedures were needed either due to the homogeneity of the nanocrystals.

2.1.4 Cu_3Se_2 nanocubes

Selenium precursor solution (ODE-Se): Selenium (IV) oxide (8.87 g, 80 mmol) was dissolved under argon atmosphere at 180 °C in 100 mL of ODE. The mixture was additionally stirred at 180 °C for 6 h to obtain a perfectly clear brownish orange solution.

We produced Cu_xSe NCs by reacting CuCl with an excess of selenium precursor in the presence of hexadecylamine (HDA). In a typical preparation, Copper (I) chloride (0.05 g, 0.50 mmol), $Al(NO_3)_3 \cdot 9H_2O$ (0.0375 g, 0.1 mmol) and HDA (5 mmol) were dissolved in 10 mL ODE. The solution was heated under argon flow to 200 °C and maintained at this temperature during 1 h to remove water and other low-boiling point impurities. Afterwards, the mixture was cooled down to 180 °C and ODE-Se (4 mL, 3 mmol) was rapidly injected through a septum into the reaction flask. The solution was allowed to react for 5 min and afterwards was quickly cooled down. The formation of Cu_3Se_2 could be qualitatively followed by the color change of the mixture from an initial light orange to eventually the deep green color of the solution containing Cu_3Se_2 nanoparticles. 3 mL of OA were added to the mixture during the cooling step, at ~70 °C, to replace the weakly bound HDA. The NCs were isolated and purified using the standard solvent/non-solvent precipitation/re-dispersion procedure. Namely, the crude solution was mixed with 5 mL of chloroform and sonicated for 5 min. The Cu_3Se_2 nanoparticles were isolated by

centrifugation at 6000 rpm during 6 min. The deep green precipitate was redispersed in chloroform (~ 5 mL) and sonicated for 1 min. Then the product was precipitated once more by centrifuging in the presence of isopropanol (~ 10 mL). The nanoparticles were re-dispersed in chloroform (~5 mL) and stored until their posterior use.

To quantitatively monitor the reaction process, aliquots were extracted at successive reaction times after the Se precursor injection. Aliquots were rapidly cooled down to quench the nanocrystal growth by dissolving them in chloroform. The excess of selenium and surfactants from the prepared nanocrystal solution was immediately removed by multiple precipitation-dispersion steps using a mixture of isopropanol for precipitation and chloroform for re-dispersion.

2.1.5 CuTe nanocubes

In a typical synthesis, 0.25 mmol (0.03 g) of CuCl was mixed with 1 mmol of TOPO (0.39 g) and 6 mL of OLA in a 25 mL three-neck flask. The reaction mixture was kept under vacuum (~ 0.1 mbar) in the Schlenk line for 20 min at room temperature and then heated to 100 °C to obtain a clear blue solution. To remove low boiling point impurities, the solution was maintained at 100 °C under vacuum for 30 min and it was periodically flushed with argon. Then temperature was increased to 160 °C under argon and a light clear yellow solution was obtained. At this temperature, 0.13 mL of TOP was added and temperature was allowed to recover to 160 °C. In parallel, a tellurium precursor solution was prepared inside the glovebox by mixing 0.13 mL of a 2 M TOPTe (0.25 mmol) solution with 0.5 mL of a 0.5 M $LiN(SiMe_3)_2$ solution in dried ODE.

The tellurium precursor solution was rapidly injected to the copper solution maintained at 160 °C, which immediately changed color, from light yellow to deep green. Upon injection, the temperature of the reaction mixture dropped to 152 °C. At this point, temperature was set to 220 °C and nanoparticles were allowed to grow for 30 min. Afterward, the colloidal solution was rapidly cooled to room temperature with a water bath at the rate of ~ 80 °C/min. When temperature reached approximately 70 °C, 2 mL of oleic acid were added to replace the weakly bound OLA molecules. The crude solution was mixed with 5 mL of chloroform and sonicated for 5 min. The CuTe nanoparticles were isolated by centrifugation at 6000 rpm during 6 min. The deep green precipitate was redispersed in chloroform (~ 5 mL) and sonicated for 1 min. Then the product was precipitated once more by centrifugation in the presence of isopropanol (~10 mL). The nanoparticles were re-dispersed in chloroform (~5 mL) and stored in glovebox until their posterior use.

The same procedures were carried out to get the nanocubes with different size, except that different amount of CuCl was used instead of 0.25 mmol (Cu:Te as 1:1) as described above. The lower the nominal Cu:Te ratio, the smaller the nanocube size. The Cu amounts used were: 0.19 mmol (Cu:Te = 3:4), 0.16 mmol (Cu:Te = 1:2). Herein, it is worth to mention that the optimal amount of Te precursor is 0.25 mmol to obtain the monodisperse nanocubes.

2.1.6 CuTe nanoplates

Optimized copper telluride nanoplates were prepared following the same procedure but reducing the reaction temperature to 190 °C and the growth time to 15 min.

2.1.7 CuTe nanorods

Optimized copper telluride nanorods were obtained following the procedure but adding 0.75 mL TOP instead of 0.25 mL and setting the growth temperature to 190 °C and the growth time to 2 min.

Synthesis of tris[bis(trimethylsilyl)amido] copper(I)

$CuN(SiMe_3)_2$ is a light-yellow powder, soluble in hydrocarbons and ethers. Its synthesis by a metathesis reaction between CuCl and $LiN(SiMe_3)_2$ was inspired by the originally proposed preparation of $Bi[N(SiMe_3)_2]_3$ by C. J. Carmalt et al.[1] All steps of synthesis by a metathesis reaction between CuCl and $LiN(SiMe_3)_2$ were carried under air-less conditions using anhydrous solvents. 10 mmol (1.67 g) of $LiN(SiMe_3)_2$ was dissolved in 20 mL of diethyl ether, and cooled to 0 °C. An exactly equimolar amount of CuCl (3 mmol, 0.30 g) dissolved in a mixture of diethylether (20 mL) and tetrahydrofuran (10 mL) were then slowly added, resulting in a yellow turbid solution. The mixture was stirred additionally for 2 h, centrifuged to remove LiCl and filtered through a PTFE filter (pore size 450 nm). All solvents were removed by vacuum for at least 1 h. The resulting yellow powder was re-dissolved in pentane (15 mL). The solution was filtered and evaporated using vacuum again. The obtained $CuN(SiMe_3)_2$ was stored inside the glovebox.

2.2 Characterization techniques

2.2.1 Transmission Electron Microscopy (TEM) and High-resolution Transmission Electron Microscopy (HRTEM)

The size, shape and crystallographic structure of the prepared nanocrystals were characterized using transmission electron microscopy (TEM) and high-resolution TEM (HRTEM). For TEM and HRTEM characterization, samples were prepared by placing a drop of the colloidal solution containing the nanoparticles onto a carbon coated copper grid at room temperature and ambient atmosphere. TEM micrographs were obtained using Zeiss (blade) microscope, operating at 120 kV. Images were digitally acquired using a MegaviewIII scanning CCD camera with a soft imaging system. The morphological, chemical and structural characterizations of the nanoparticles were carried out by HRTEM and electron energy loss spectroscopy (EELS) with a Nickel grid. HRTEM images were obtained using a Jeol 2010F field-emission gun microscope with a 0.19 nm point- to-point resolution at 200 keV with an embedded Gatan image filter for EELS analyses. Images were analyzed by means of Gatan Digital micrograph software. The Particle size distributions were obtained by measuring at least 150 NPs per each sample. Samples were prepared by suspending the nanoparticles in isopropanol and agitating in an ultrasonic bath. Several drops of the suspended nanoparticles were applied to carbon-coated copper grids (Ted-Pella) and silicon substrates, respectively.

2.2.2 Scanning Electron Microscopy (SEM) and High-resolution Scanning Electron Microscopy (HRSEM)

The SEM measurement was performed using a FEI Nova NanoSEM 230 SEM with an energy dispersive X-ray spectroscopy (EDX) detector at 20 kV to study the composition of

nanoparticles. The HRSEM pictures were taken by FEI Quanta 200F. The particles were cleaned very well and dissolved in chloroform. The samples were prepared by dropping the solution on the clean Silicon substrates.

2.2.3 X-ray Diffraction (XRD)

The powder XRD patterns were obtained with Cu Kα (λ = 1.5406 Å) radiation in reflection geometry on a Bruker D8 operating at 40 kV and 40 mA.

2.2.4 Surface Enhanced Raman Spectroscopy

SERS experiments were carried out on 250 μL solutions containing 0.17 g L^{-1} of particles (either CuTe or Au) alone (Chapter 5, Figure 14) or with minute concentrations of analytes. Briefly, 2.5 μL of analyte in acetone (10^{-5} M) were added to 1 mL of particles in chloroform giving rise to a final concentration of 10^{-7} M. Samples were studied in solution by using a macrosampler adaptor with 15 mm working distance macro-objective. The inelastic scattering was collected with a Renishaw Invia system by exciting the samples with 830 nm laser lines for 10 s and a power at the sample of 89 mW. Gold nanostars were produced by following standard methods (Chapter 5, Figure 15).[2]

For a given excitation wavelength, the SERS intensity is related to the absolute square electromagnetic field outside the particle and is enhanced, with respect to the Raman intensity, by a factor (EF):

$$EF_{(\lambda)} = \frac{\left|E_{out(\lambda)}\right|^2 \left|E_{out(\lambda-\lambda s)}\right|^2}{E_0^4} = \frac{I_{SERS}}{I_R} f \qquad (1)$$

Where Eout(λ) and Eout(λ- λs) are the electromagnetic fields generated by the incident excitation and the Stokes' shifted Raman. The use of the first term of the equation for the calculation of the enhancement factor results difficult, thus, experimentally, EF is usually calculated by direct comparison of the intensities provided by the SERS and Raman experiments and normalized by the total number of molecules (N) in each experiment (f =NR/NSERS).[3] In our case, a concentrated solution of nile red (10^{-2} M in acetone) was measured under the same conditions that the experiments carried out nanoparticles.

2.2.5 Test of Cu_xS nanocrystals as cathodes in all-vanadium redox flow batteries (VRB)

Due to their flexibility and fast response, flow batteries are one of the most promising solutions for load leveling and peak shaving of renewable energies such as solar and wind.[4-6] In a flow battery, the energy is chemically stored in two independent solutions containing each of them a redox couple. Unlike in other energy storing devices, such as Li-ion batteries or electrochemical capacitors, in the redox battery, energetic capacity and power are independent. Among redox batteries, better performances in terms of life time and cost are obtained when using solutions of vanadium ions for both semi-reactions: $[VO]^{2+}/[VO_2]^{+}$,[7] positive cell; and V^{3+}/V^{2+}, negative cell. In this case, the battery is known as an all-vanadium redox flow battery (VRB).

Carbon-based electrodes, such as graphite felts,[8] carbon nanotubes,[9] carbon fibers[10] or mesoporous carbon[11] are typically used in VRB because of their relative low cost, high surface area, chemical stability and good electrical conductivity. However, their kinetic reversibility is rather poor, which is especially critical at the cathode. The efficiency of VRB is usually limited

by the rate and potential of the $[VO]^{2+}/[VO_2]^{+}$ cathodic reaction.[7] Thus, the introduction of catalytic elements to improve the efficiency of these reactions has been widely studied.[11]

$Cu_{2-x}S$ nanocrystals were thoroughly purified by multiple precipitation and redisperion cycles. Subsequently, 1 mg of nanoparticles was supported on 1 cm^2 planar graphite substrate by drop casting. The remaining organic ligands were removed using an aqueous solution of hydrazine. Then, the material was dried in vacuum at 100 ºC. Afterwards, the supported particles were covered by a solution of Nafion (10 %) in water. Upon evaporation of the solvent, the electrochemical activity was characterized by means of cyclic voltametry using a Biologic VMP-3 potentiostat linked to a 50 mL glass thermostated electrochemical cell. The cell was equipped with a platinum counter electrode and a Luggin capilar $Hg/Hg_2SO_4/K_2SO_4$ (sat) reference electrode. The VRB cathode was used as a working electrode. Measurements were performed in an inert atmosphere using 30 mL of a 0.5 M $VOSO_4$ and 1 M H_2SO_4 solution.

The electrocatalytic activity (peak currents and potentials of redox reactions) and the reversibility of the cathodic reaction $[VO]^{2+}/[VO_2]^{+}$ are the key parameters to evaluate an electrode performance in redox flow batteries. In particular, the energy storage efficiency of a battery is proportional to the ratio of its discharge and charge voltages.[7] The lower the oxidation potential, the lower the voltage needed to charge the battery, and thus the higher its efficiency.

2.2.6 Polymer coating CuTe nanoparticles

The cubic CuTe nanoparticles (NPs) with length of 16 nm were transferred to the aqueous phase using the polymer coating methodology, as previously described by Pellegrino et al.[12] This methodology was adapted based on the overall surface area of the CuTe NPs, aiming effectively

to coat all the NPs. That is, it has to be adjusted taking into consideration the surface area per single cubic CuTe NP (A_0) and then, the total surface area (A) to coat. To calculate the surface area for single NP, an effective length was used (d_{eff}). This length is the result of the addition of the length observed in the TEM measurements (d_{core}= 16 nm) and two times the assumed thickness of the surfactant shell ($d_{surfactant}$= 1 nm). The amount of polymer needed to stabilize the NPs was optimized, yielding best results using 1000 polymer monomers per nm^2 ($r_{P/Np}$). (*Formulas (2) and (3)*)

$$A_0 = 6 \times \left(d_{core} + 2d_{surfactant}\right) \times \left(d_{core} + 2d_{surfactant}\right) = 6 \times d_{eff}^2 \quad (2)$$

$$A = C \times V \times N_A \times A_0 \quad (3)$$

Where: A_0 is the surface area of single cubic nanoparticle (nm^2); A is the total surface area of all the colloidal nanoparticles in the solution (nm^2); d_{core} is the length of the side of the particles; $d_{surfactant}$ corresponds with thickness of the surfactant layer on NPs surface; d_{eff} is the total length; V refers to the volume of solution of NPs (L) and N_A is the Avogadro constant.

The amphiphilic polymer used is formed by a backbone of poly (isobutylene-*alt*-maleic anhydride) (PMA) derivatized with dodecylamine in order to have an aliphatic domain. The polymer presents a 75 % of the anhydrides modified with dodecylamine. The procedure was described by Lin et al.[13] The amount of polymer which is needed to coat the particles was estimated by *formula (4)*.

$$V_P = \frac{N_P}{C_P} = \frac{A \times r_{P/Np}}{N_A Cp} \quad (4)$$

Where, V_P is the volume of polymer needed to coat the NPs; N_P, number of NPs mol (mol); C_P, concentration of polymer (M); A is the total surface area of nanoparticles to coat (nm^2)and $r_{P/Np}$ is

the ratio of monomer per nm^2 needed to stabilize efficiently the particles and N_A is the Avogadro constant.

In the case of the coating 500 µL (V) of the CuTe NPs with 16 nm in length (d_{core}; d_{eff}= (d_{core} + 2 $d_{surfactant}$)= (16+2)= 18 nm) with a concentration of 0.1 µM (C), taking a ratio of the monomer as 1000 monomer per nm^2, the surface per NP (A_0) will be equal to 1944 nm^2 and the total surface area (A) in the 500 µL of CuTe NPs solution will be 5.85 x 10^{16} nm^2. It was determined experimentally that 1000 monomer/ nm^2 ($r_{P/Np}$) represents a good value to provide the NPs with colloidal stability. Finally, using the Formula 3, the volume required for polymer (V_P) of 0.05 M (C_P) is 1.95 mL.

The NPs and the polymer were placed together in a round flask, and diluted with chloroform. After 10-20 min, the chloroform was slowly evaporated under reduced pressure by a rotavapor system (Laborota 4000, Heidolph) using 70 °C in the bath.[14] The resulting solids were quickly dissolved in basic buffer solution (0.1 M NaOH) to drive the nanoparticles to the aqueous phase. To remove any big aggregate, the solution was filtrated through a syringe membrane filter (Roth # P818.1, 0.22 µm pore size). Then the buffer was changed to water by the use of 100 kDa MWCO Amicon centrifuge filters (Millipore, Amicon Ultra-15, #UFC9100). The empty micelles generated by the excess of polymer were removed by gel electrophoresis (Sub-Cell GT electrophoresis cells, Bio-Rad). The previously concentrated nanoparticles were loaded into wells of a 2 % agarose gel (Invitrogen #15510027) in 0.5 x TBE solution and gel electrophoresis was performed for one hour applying 100 V. The band which contained the nanoparticles was cut. The particles were extracted running again the electrophoresis, but this time, the gel-band was previously placed in a dialysis membrane (3500 Da MWCO, Roth). Finally, the NPs

solution was filtered again by a syringe filter (0.22 μm pores) to remove small gel pieces, and concentrated by 100 kDa MWCO Amicon centrifuge filters.

2.2.7 UV-Vis absorption spectra

Figure 18a in Chapter 5 shows the absorption spectra of the NPs before (black line) and after (red line) the polymer coating of the NPs. Figure 18b corresponds with the gel electrophoresis in agarose 2 % (100 V, 1 h) of the coated NPs and they were compared with a control sample, *i.e.* 10 nm gold NPs (see in the bottom). Finally Figure 18c presents a photograph of the final solution of the polymer coated CuTe NPs.

2.2.8 ζ–potential measurement

The hydrodynamic radius and the ζ–potential value of the particles were also evaluated using a Malvern ZetaSizer. Particles showed a final hydrodynamic radius in number results 22.5 nm and a ζ- potential value of – 55.6 mV. In both cases the standard deviation was less than a 5 %. (Chapter 5, Figure 19)

The concentration of the NPs was estimated as previously described by Rivera_Gil et al[15] for any inorganic NP of known size, geometry and density. Taking into consideration size, shape and the density, the molecular weight of the NPs can be determined in good approximation. In this particular case, particles are cubes of 16 nm of length composed by CuTe (ρ_{CuTe}= 7.1 g/cm^3). The weight of one NP can be calculated using the density of the material and the volume of the particle. For a cubic NP the volume equation is the edge length (d_{core}) to the cubic power. In this case the volume for one particle in cm^3 is 5.088 x 10^{-18} cm^3. This volume of one NP multiplied

by the density of the material will give us the weight of one single NP. In this case, one NP weight 3.61 x 10^{-17} g. The molecular weight for this NP will be the product of the weight of one NP by the Avogadro constant, *e.g.* 2.17 x 10^{7} g/mol. Thus, a weighted mass of inorganic material (NPs in grams) can be used to give an approximated concentration (mol/L) of the NPs solution. For example, if 18.5 mg of CuTe NPs were dissolved in 8.5 mL of $CHCl_3$, the final concentration of NPs will be approximately 0.1 μM.

Once the concentration is determined, using the absorption spectra, a standard curve can be done. In the actual sample, the standard curve was obtained using the absorbance of NPs solutions of known concentration of CuTe NPs at their maximum (950 nm). The standard curve to calculate the concentration is presented (Chapter 5 Figure 20). So, using this approximation, it is possible to estimate the concentration of any solution of these NPs.

2.2.9 Cell culture and laser irradiation

3T3 embryonic fibroblasts were incubated over night at 37 °C, 5 % CO_2 in growth medium (DMEM-F12 basal medium supplemented with 10 % FBS, 1 % L-glutamine, 1 % penicillin/streptomycin). The next day the cells were incubated with water soluble CuTe nanocubes at a final concentration of 75 nM for 3h. Afterwards, the medium was washed away to remove free nanoparticles and the cells were placed in a solution of 100 μM DAPI (4',6-diamidino-2-phenylindole) in PBS. DAPI is an impermeant dye commonly used to stain the nucleus. DAPI enters the cell faster when the cellular and nuclear membrane are damaged than when the cells are viable. We took advantage of this and incubated the cells in a solution of

DAPI. Immediately after addition and within 10 min the images before and after NIR laser irradiation were taken.

The microscopic set up consisted of a wide-field fluorescence microscope coupled to a continuous diode laser emitting at 830 nm. The maximum output of the laser is 130 mW. However the maximum light power reaching the sample using a 100x/1.3 oil immersion objective was measured to be around 19 mW. The area of the spot was 38 μm^2. With a tunable power supply the output power of the laser can be varied smoothly from 0 to 19 mW effective light power on the sample plane.

Cells containing the CuTe nanocubes were irradiated with 90 % maximum intensity during 1-2 s with the laser. The final intensity of the laser was 0.5 $mW/\mu m^2$. As a control for laser illumination, cells free of nanoparticles were treated as described before.

2.3 References:

(1) Carmalt, C. J.; Compton, N. A.; Errington, R. J.; Fisher, G. A.; Moenandar, I.; Norman, N. C.; Whitmire, K. H. *In Inorganic syntheses; Alan, H. C., Ed.* **1997**, *98*.

(2) Rodríguez-Lorenzo, L.; Álvarez-Puebla, R. N. A.; Pastoriza-Santos, I.; Mazzucco, S.; Stéphan, O.; Kociak, M.; Liz-Marzán, L. M.; García de Abajo, F. J. *J. Am. Chem. Soc.* **2009**, *131*, 4616-4618.

(3) Álvarez-Puebla, R. A. *J. Phys. Chem. Lett.* **2012**, *3*, 857-866.

(4) Huang, K. L.; Li, X. G.; Liu, S. Q.; Tan, N.; Chen, L. Q. *Renew. Energ.* **2008,** *33*, 186-192

(5) Fabjan, C.; Garche, J.; Harrer, B.; Jorissen, L.; Kolbeck, C.; Philippi, F.; Tomazic, G.; Wagner, F. *Electrochim. Acta.* **2001,** *47*, 825-831

(6) Skyllaskazacos, M.; Rychcik, M.; Robins, R. G.; Fane, A. G.; Green, M. A. *J. Electrochem. Soc.* **1986**, *133*, 1057-1058.

(7) Ponce de Leon, C.; Frias-Ferrer, A.; Gonzalez-Garcia, J.; Szanto, D. A.; Walsh, F. C.. *J. Power Sources.* **2006**, *160*, 716-732.

(8) Zhong, S.; Padeste, C.; Kazacos, M.; Skyllas-Kazacos, M. *J. Power Sources.* **1993**, *45*, 29-41.

(9) Zhu, H. Q.; Zhang., Y. M.; Yue, L.; Li, W. S.; Li, G. L.; Shu, D.; Chen, H. Y. *J. Power Sources.* **2008**, *184*, 637-640.

(10) Sun, B.; Skyllas-Kazacos, M. *Electrochim. Acta.* **1991**, *36,* 513-517.

(11) Shao, Y.; Wang, X.; Engelhard, M.; Wang, C.; Dai, S.; Liu, J.; Yang, Z.; Lin, Y. *J. Power Sources.* **2010**, *195*, 4375-4379.

(12) Pellegrino, T.; Manna, L.; Kudera, S.; Liedl, T.; Koktysh, D.; Rogach, A. L.; Keller, S.; Radler, J.; Natile,G.; Parak, W. J. *Nano. Lett.* **2004**, *4*, 703-707.

(13) Lin, C. A. J.; Sperling, R. A.; Li, J. K.; Yang, T.-Y.; Li, P.-Y.; Zanella, M.; Chang, W. H.; Parak, W. J. *Small* **2008**, *4*, 334-341.

(14) Guardia, P.; Di Corato, R.; Lartigue, L.; Wilhelm, C.; Espinosa, A.; Garcia-Hernandez, M.; Gazeau, F.; Manna, L.; Pellegrino, T. *ACS. Nano.* **2012**, *6*, 3080-3091.

(15) Rivera_Gil, P.; Jimenez De Aberasturi, D.; Wulf, V.; Pelaz, B.; Del Pino, P.; Zhao, Y.; De La Fuente, J. M.; Ruiz De Larramendi, I.; Rojo, T.; Liang, X. J.; Parak, W. J. *Acc. Chem. Res.* **2013**, *46*, 743–749.

Chapter 3

Synthesis of Shape, Size controlled Cu_xS nanoparticles and the Morphology Evolution From Spheres to Dodecahedrons.

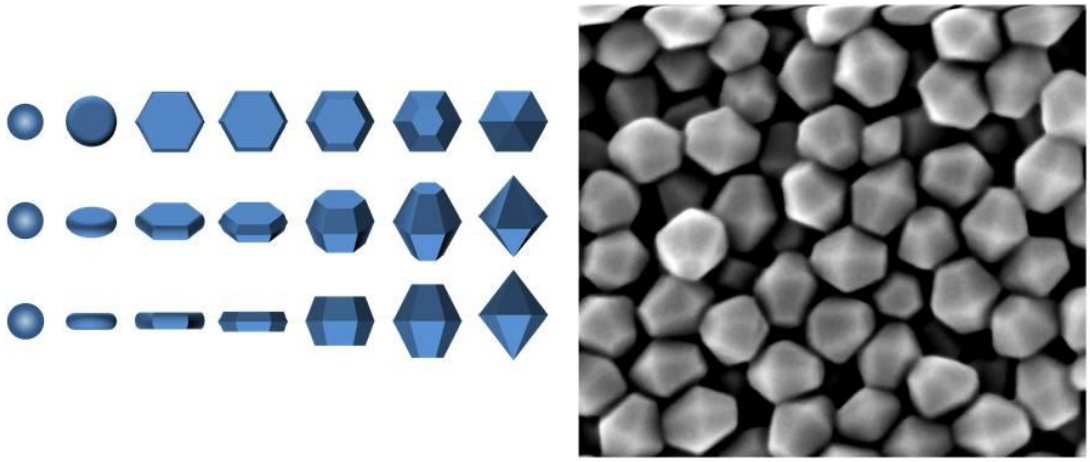

3.1 Introduction

The ability to control the nanocrystals composition, [1-3] size, [4] shape,[5-9] crystal phase[10] and surface planes allows tuning their optical and optoelectronic properties and their activity and selectivity towards specific catalytic and photocatalytic reactions. The control at the nanoscale of the composition and morphology of copper chalcogenides is an especially interesting case, because of their stoichiometry-dependent properties and their ample range of applications.[11-14] However, the rich phase diagrams of copper chalcogenides make their growth mechanisms also especially challenging to uncover and control. The equilibrium phase diagram of copper sulfide

exhibits at least seven phases: i) monoclinic low-chalcocite Cu_2S;[15] ii) hexagonal high-chalcocite Cu_2S;[16] iii) monoclinic djurleite $Cu_{1.96}S$; [15] iv) hexagonal digenite $Cu_{1.8}S$;[17] v) monoclinic roxbyite $Cu_{1.78}S$; vi) orthorhombic anilite $Cu_{1.75}S$;[18] vii) hexagonal covellite CuS.[19] Such variety of crystallographic phases has allowed the preparation of nanoparticles with different morphologies and compositions: i) spherical chalcocite[20] and djurleite[21] nanoparticles; ii) chalcocite nanowires;[22-23] iii) chalcocite,[24-26] roxbyite[27-28] and covellite[29-30] nanodisks; iv) anilite hollow nanocages;[11] v) djurleite and digenite irregular nanocrystals.[30-31]

As a promising, well-known p-type semiconductor material, copper sulfide has an attractive application in many fields such as solar cell material[31] and optoelectronic devices[32] due to a suitable band gap of 1.2–1.8 eV, low cost, p-type conductivity[33-34]and high absorption coefficient.[35] By far, a lot of methods have been developed for the synthesis of nanostructured copper sulfide. [36-39] For example, Korgel et al. presented a solventless synthetic technique for size- and shape-controlled Cu_2S nanocrystals from single-source metal thiolate precursors.[40-41]Ghezelbash et al. synthesized copper sulfide nanocrystals by a high temperature solution phase method.[16] Other methods like the hydrothermal approach via decomposition of Cu $(acac)_2$ and S in oleylamine[30] and the aqueous colloidal capping methods have also been introduced into the synthesis of copper sulfide nanoparticles[37]. These copper sulfide obtained possesses variety of the crystallographic structures with very different electronic and optical properties. From synthetic point of view, considerable efforts have been devoted to the shape controlled synthesis of nanostructured copper sulfides like nanorobs, [40] nanotubes, [42] nanofiber, [43] hollow spheres[44] and so on. However, up to now, few studies have reported on the novel shape formation of copper sulfide like rhombus. Herein, we proposed a very simple route not only for the

systematic investigation on the size control of the copper sulfide nanodisks which have drawn considerable attentions as one of the nanocrystalline semiconductors with lamellar nanostructure and anisotropic features but also for studying the influence of different stoichiometric ratios on the shape of copper sulfide nanoparticles. In further, the goal of the present work is to provide the mechanisms to extend the control of the $Cu_{2-x}S$ nanoparticles morphology to a wider range: from spherical to tetradecahedral and dodecahedral geometries (Scheme 1). Herein we reveal the synthetic routes and discuss the growth mechanisms allowing tuning the nanoparticle morphology in such extended range.

3.2 Results and Discussion

3.2.1 Shape, size control and the corresponding investigations on the reaction mechanism

$Cu_{2-x}S$ Nanospheres:

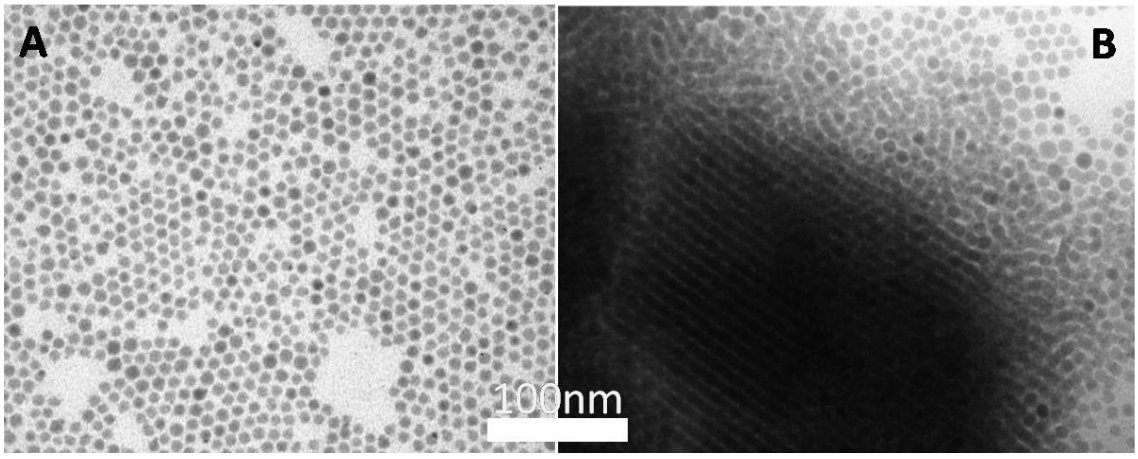

Figure 1. TEM images of the $Cu_{2-x}S$ nanoparticles: Spheres (A) and self-assembly (B).

The monodisperse $Cu_{2-x}S$ nanospheres with an average size of 7.3 ± 0.7 nm were obtained in the presence of dodecanethiol (DDT) as shown in Figure 1. Herein, these spherical nanoparticles allowed size control only within narrow range (between 6 and 10 nm) just by changing duration of the synthesis. Temperature increasing is not helping because of the DDT instability at the elevated temperature (It starts to decompose at 180 ºC with un-favourite influence on the particle size distribution). Duration of the synthesis also cannot be longer than 1 h without broadening of the size distribution.

$Cu_{2-x}S$ Nanodisks:

The reaction of copper chloride with an excess of TBDS resulted in the nanodisks formation as shown in the Figure 2.

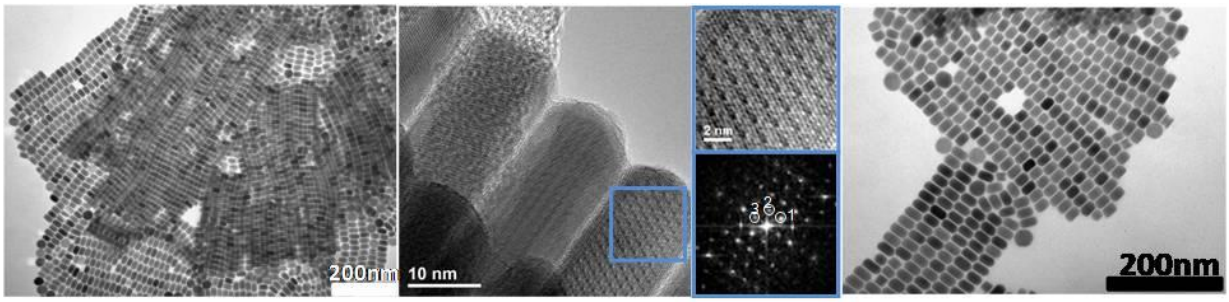

Figure 2. TEM images of the $Cu_{2-x}S$ nanodisks obtained with TBDS (left) and DDT (right) as S precursor. In the middle are the HRTEM image and the corresponding power spectrum.

Considering the reaction temperature and time both affect the morphology of the copper sulfide nanocrystals, we conducted a set of parallel experiments to gain further inside into the growth process of the nanodisks. The typical TEM images shown in Figure 3 illustrate how the size of copper sulfide nanodisks evolve with increased reaction time. As we can see, in Figure 3A-D, TEM images of nanodisks obtained at 180 ºC reveal the size evolution from 15.9 ± 0.78 to

25.9 ± 0.82 nm and 10.3 ± 0.56 to 13.1 ± 0.41 nm for the diameter and thickness, respectively. For the sample of 20 min in Figure 3A, the prepared quasi-spherical nanoparticles are fairly monodisperse and the platelets have a favorite tendency to lie flat on the substrate compared to

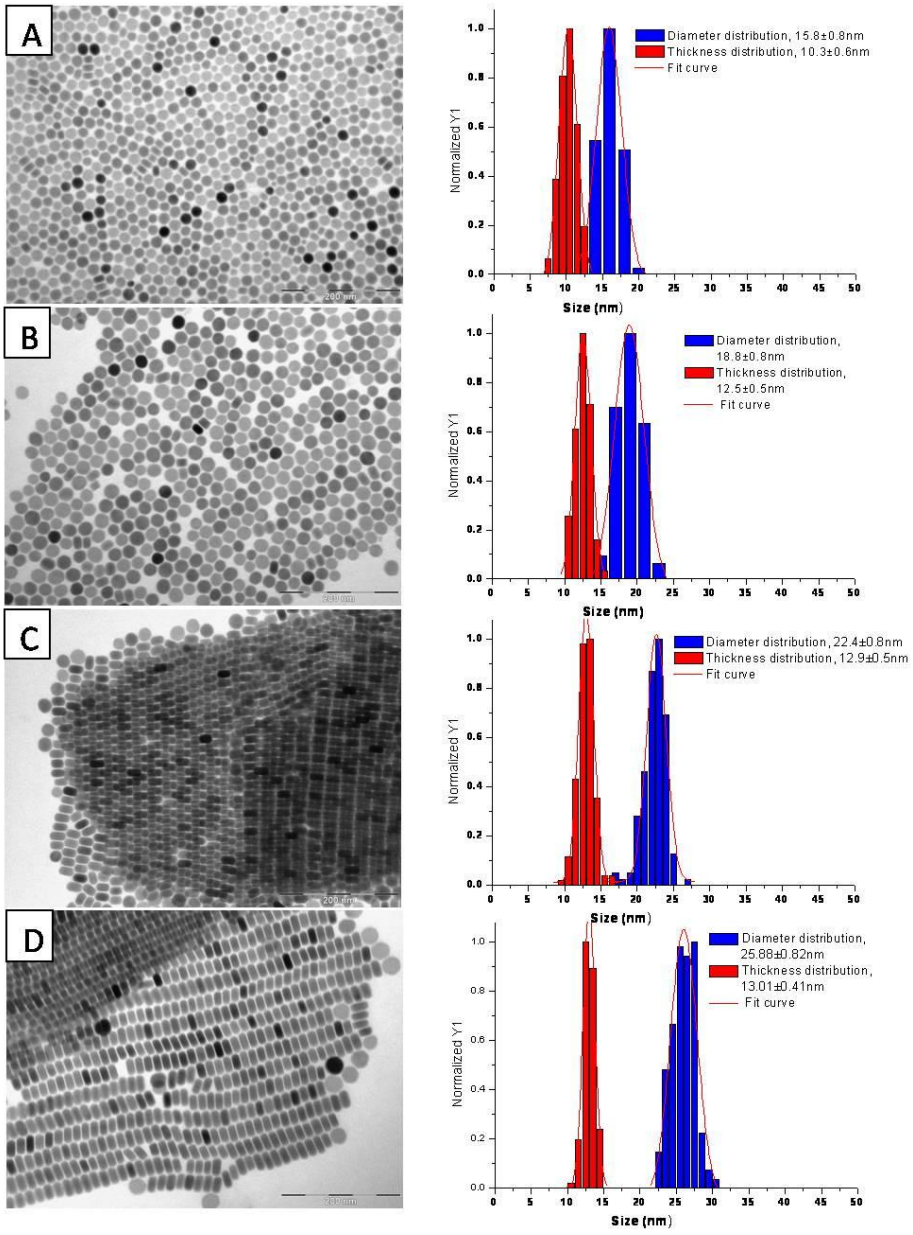

Figure 3. TEM images of the copper sulfide nanoparticles synthesized at different time for 180 ºC. (A) 20, (B) 30, (C) 40, and (D) 60 min. Corresponding size distributions are put by side and the histograms on the left represent the thickness distribution and on the right diameter distribution

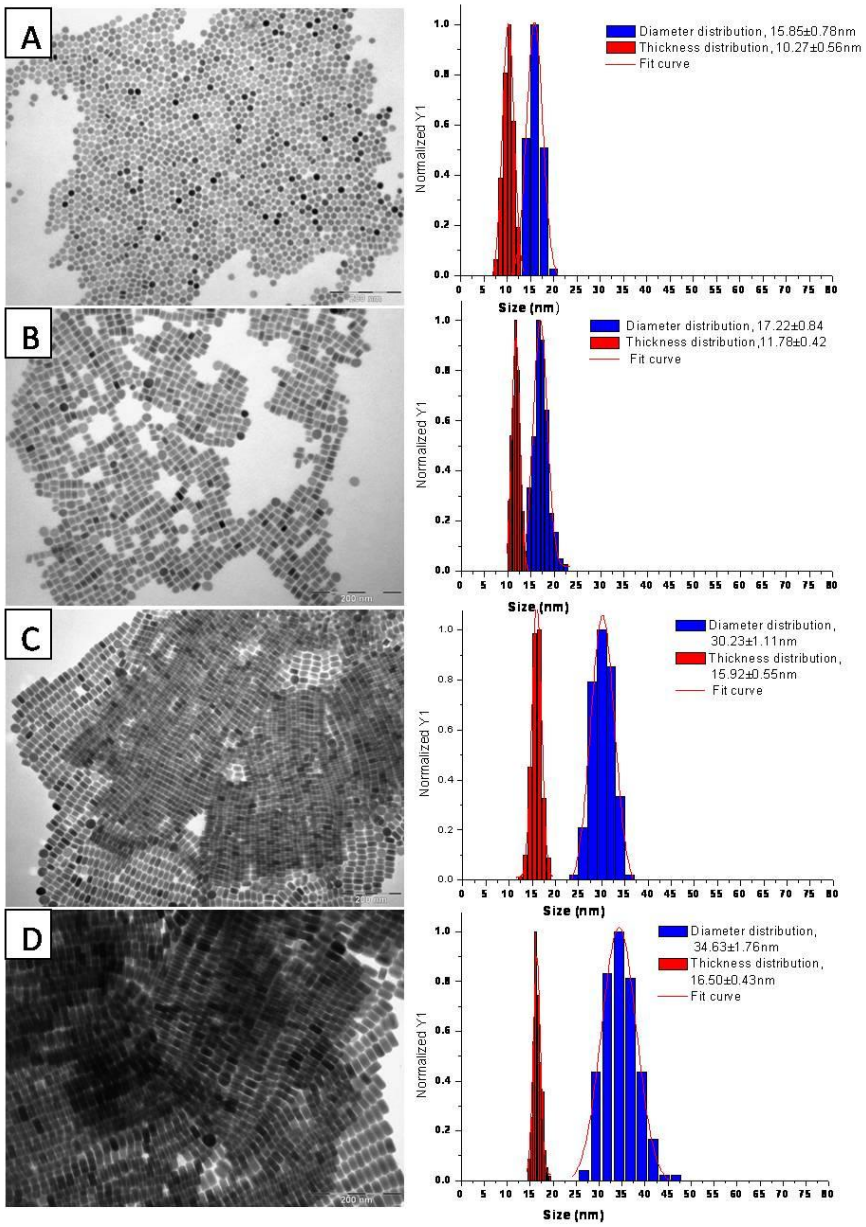

Figure 4. TEM images of the copper sulfide nanoparticles synthesized at different temperature for 20 min. (A) 180 ºC, (B) 190 ºC, (C) 200 ºC, and (D) 210 ºC. Corresponding size distributions are put by side and the histograms on the left represent the thickness distribution and on the right diameter distribution.

the few part of disks as seen to be perpendicular to the substrate. After 30 min (Figure 3B), the disk diameter increases by 3 nm relative to 20 min and the thickness exhibits relatively 'great' change from 10.3 ± 0.56 to 12.5 ± 0.50 nm. Prolonging the reaction time, the disks tend to stack together by face-to-face which look like rods and self-assemble into multilayer structure as shown in Figure3C and D. During this period, the particles keep growing gradually; however for the thickness of the particles, there is no significant increase during the synthesis. It is really worth to mention here that the particles we prepared mostly have an excellent narrow size distribution as shown clearly in the presented histograms although the size distribution undergoes different change with time going. Herein, the average size was measured by randomly counting about 150-200 particles in the images by Image Tool software.

The further investigation on the size evolution of disks was also produced over a range of temperature from 180 to 210 ºC (Figure 4). As similarly discussed before, for the particles we synthesized at elevated temperature with same reaction time for 20 min, the size increases simultaneously but there is no obviously qualitative effect on the morphological evolution of the nanodisks. In general, most of the particles prefer to keep lying flat on the substrate rather than standing-up at relatively low temperature (Figure 4A). In Figure 4B, conversely, large quantities of stacked particles are observed although they are a little small (17.2 ± 0.84 and 11.8 ± 0.42 nm for diameter and thickness, respectively). At higher temperature, larger disks can be got and they are well ordered into multilayer (bilayer in Figure 4C and multilayer in Figure 4D) which could be reasonable because of the enhanced growth rate.

In order to get a clear observation on the nanodisks growth with the different time and temperature, an effective profile was made in Figure 5. In order to determine the mean

nanoparticles size (D for diameter and T for thickness) and the corresponding size distribution S, more than 150 particles were measured for each sample as we mentioned before. The corresponding size distribution, S, is defined as the ratio S/D and S/T. The half standard deviation, σ, is calculated according to $\sigma = 1/2\{[P (Di- D)^{2}]/ [n - 1]\}^{1/2}$ and error rate is defined as σ /D and σ /T.

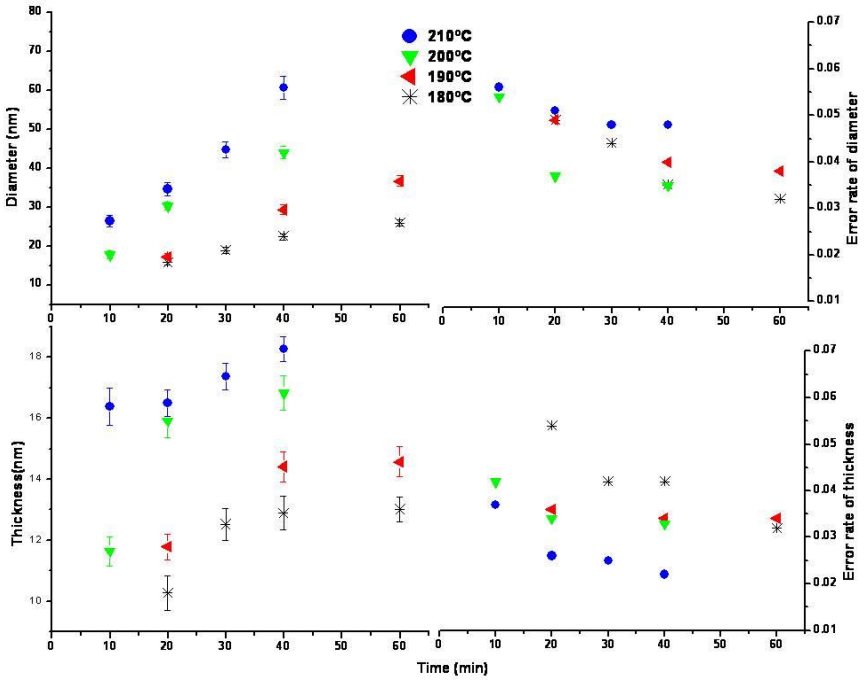

Figure 5. The profile made from the temperature influence on the size of the nanodisks and the corresponding error rate.

Herein, only OLA is used instead of thiol and other solvent additions which are normally employed to produce uniform $Cu_{2-x}S$ nanodisks on a large scale. So the OLA not only serves as the solvent but also the capping ligand that stabilizes nanodisk size and shape. It is interesting to notice that the space between the face-to-face stacked nanodisks is about 1.5 nm, (Figure 2, in

the middle) which is equal to the length of OLA molecules.[53] This indicates that the nanodisks are capped by the absorbed one layer OLA on the surface which can provide steric stabilization and prevent aggregation of the nanoparticles. In addition, we know that the OLA has a preferential binding to the [001] facets of hexagonal metals so as to inhibit [001] directed growth as Puntes et al. observed for Co nanodisks grown in the presence of amine capping ligands.[54] This is really consistent with the evidently increase in diameter but the negligible change in thickness with prolonged reaction time or increasing temperature as shown in Figure 3 and 4. Longer reaction times (Figure 3) and higher reaction temperatures (Figure 4) increased the nanodisks diameter and crystallinity which will be discussed in next section, but only modified slightly their thickness (Figure 5) and not perceptibly their crystallographic phase and composition. However, excessively temperature increasing higher than 210 ºC and duration of the synthesis longer than 1 h are not beneficial to the narrow size distribution.

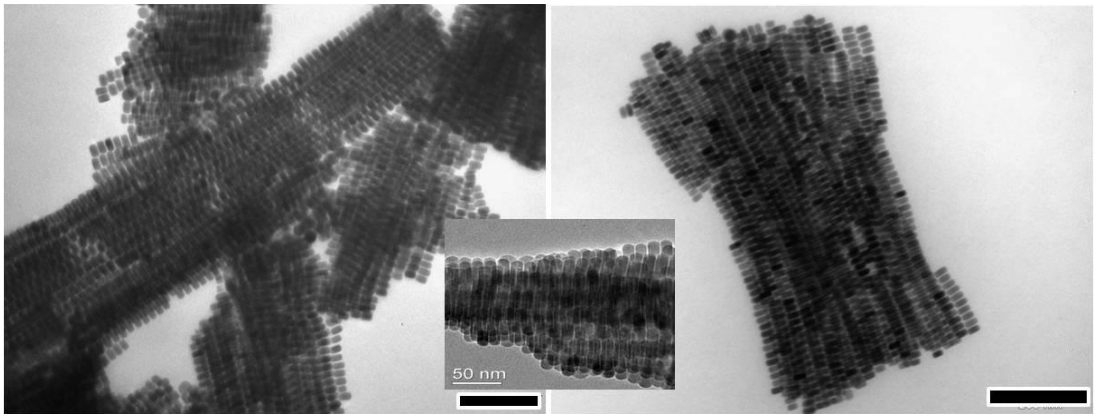

Figure 6. TEM images of self-assembled $Cu_{2-x}S$ nanodisks. (a) 180 ºC for 60 min, (b) 200 ºC for 20 min. Scare bars correspond to 200 nm.

Over all the reaction temperature examined, the self-assembled nanodisks into multilayer formed corn-like structures are observed (Figure 6) due to the dipole-dipole interaction and van der Waals force during solvent evaporation, as proposed for Cu_2S.[55]

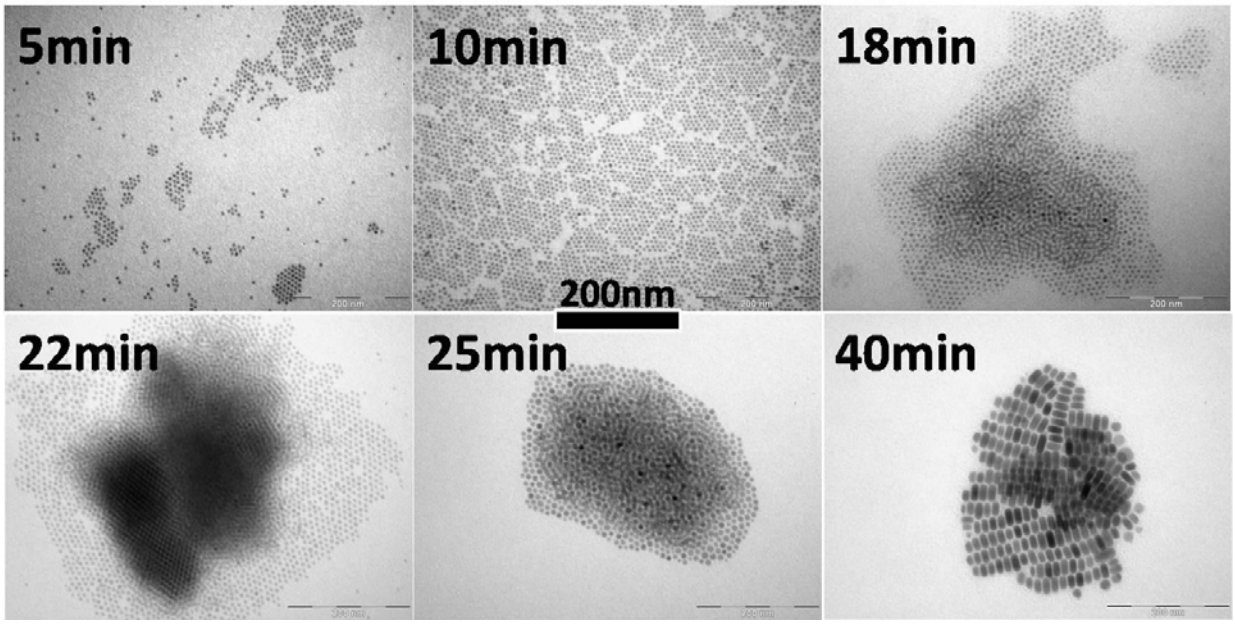

Figure 7. The particles obtained at the different reaction time and the TEM pictures showing the morphology evolution of the nanodisks.

In order to understand better how the disks were formed, the aliquots were taken out at the different reaction time as shown in the Figure 7. As discussed earlier, for the synthesis of spheres, the DDT is quite essential to get the narrow size distribution. However, its presence delayed or even suppressed the disk formation which depends on strongly on the reaction temperature as well. At higher temperature as 220 ºC, there were still nanodisks formed with the elongated reaction time. However, the quality of the disks was much worse than that obtained in the presence of TBD. On the other hand, the suppression of DDT slowed down the transition of spheres to disks which allowed monitoring the reaction process. At the beginning, the process

was dominated by a rapid nucleation and a large quantity of $Cu_{2-x}S$ nuclei was produced. These nuclei collided each other and combined together through Ostwald ripening process to form small spheres. The initially formed spheres kept growing and then the Ostwald ripening predominated the reaction again induced the formation of nanodisks.

Thin tetra-decahedrons of $Cu_{2-x}S$:

It's noticeable that the use of TBDS as S precursor only resulted in the formation of nanodisks when the Cu concentration is relatively low as 0.05 M. The double concentration of Cu as 0.1 M (1 mmol Cu precursor in the system) finally produced the thin tetradecahedrons (Figure 8). As shown in Figure 9, the pilled nanoplates were formed initially rather the nanodisks. Based on the probable dipole-dipole interactions,[26] these thin nanoplates assemblies face to face into dimmers and the relatively low growth rate allowed the dimmers to continue growing until the concentration was decreased below the crucial point and thin tetradecahedrons were obtained finally.

Tetra-decahedrons of $Cu_{2-x}S$:

The increasingly higher Cu precursor concentration from 0.1 M to be 0.2 M induced the formation of "thicker" tetradecahedrons as shown in Figure 10. In this process, the initially formed nanoplates assembled into trimers (in 20 min, Figure 11) and due to the relatively high concentration of Cu precursor in the solution, these trimers continued growing along the <100> direction as to be explained in details in next section.

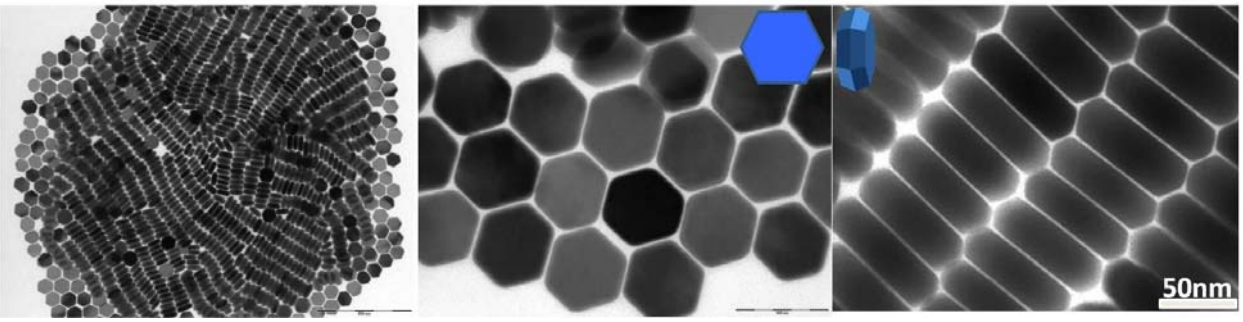

Figure 8. TEM pictures of thin tetradecahedrons obtained in the concentration of Cu as 0.1 M.

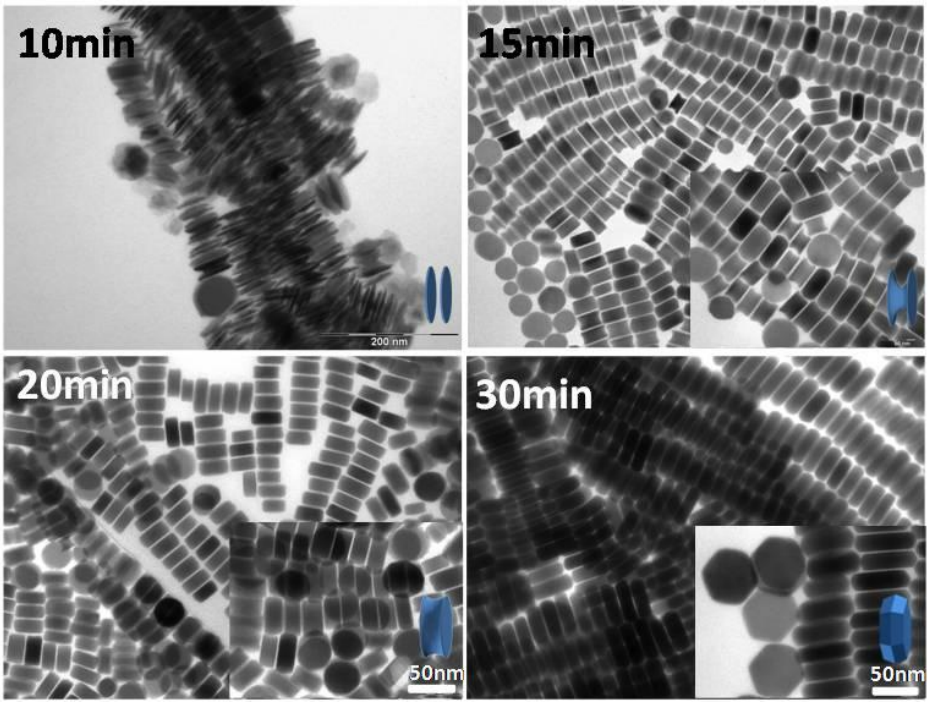

Figure 9. The particles obtained at the different reaction time and the TEM pictures showing the morphology evolution of the thin tetradecahedrons.

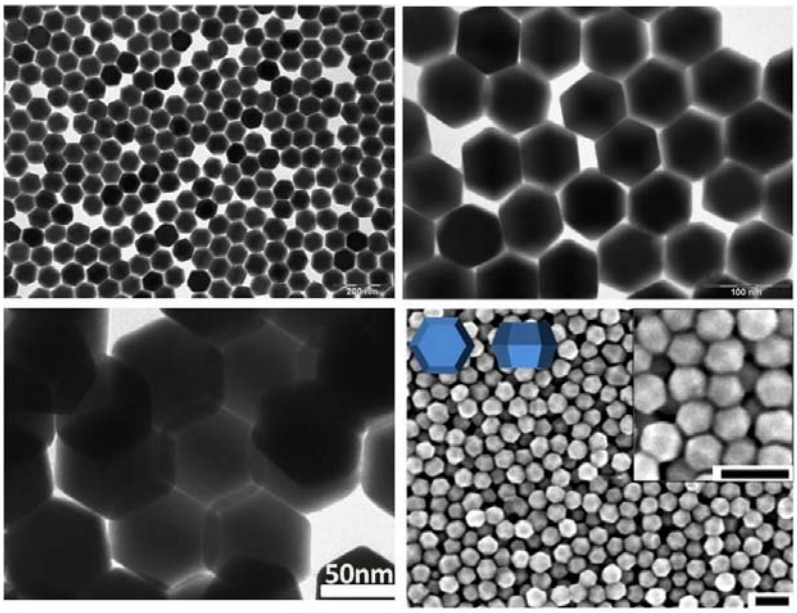

Figure 10. The tetradecahedral nanocrystals obtained in the concentration of Cu as 0.2 M.

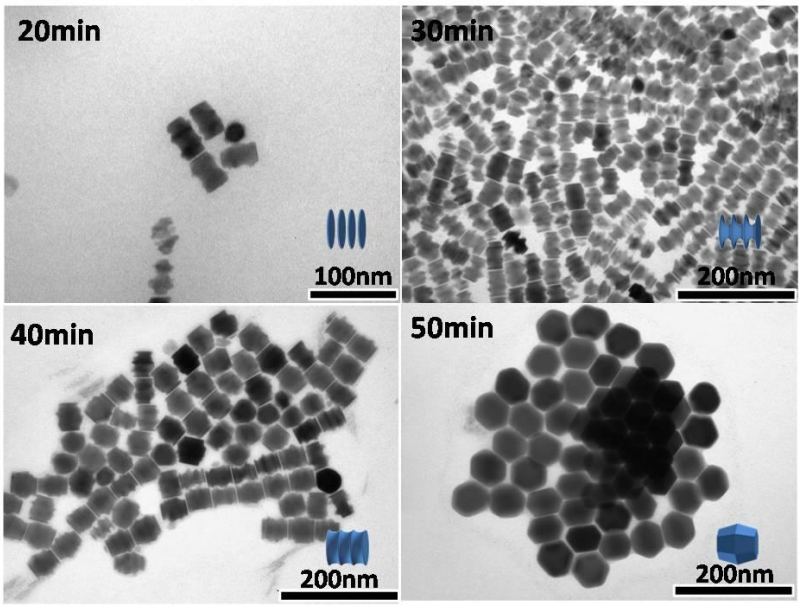

Figure 11. The particles obtained at the different reaction time and the TEM pictures showing the morphology evolution of the tetradecahedrons

Elongated Tetra-decahedrons of $Cu_{2-x}S$:

When the introduced amount of Cu precursor was increased to 5 mmol in the synthesis, namely, the concentration as 0.5 M, the elongated tetradecahedrons were obtained as shown in the Figure 12. The elongation of the tetradecahedrons can be assigned to the initially formed quadrumers (Figure 12, 20 min). These quadrumers gradually became faceted in the sustained growth due to the higher Cu precursor concentration around the particles.

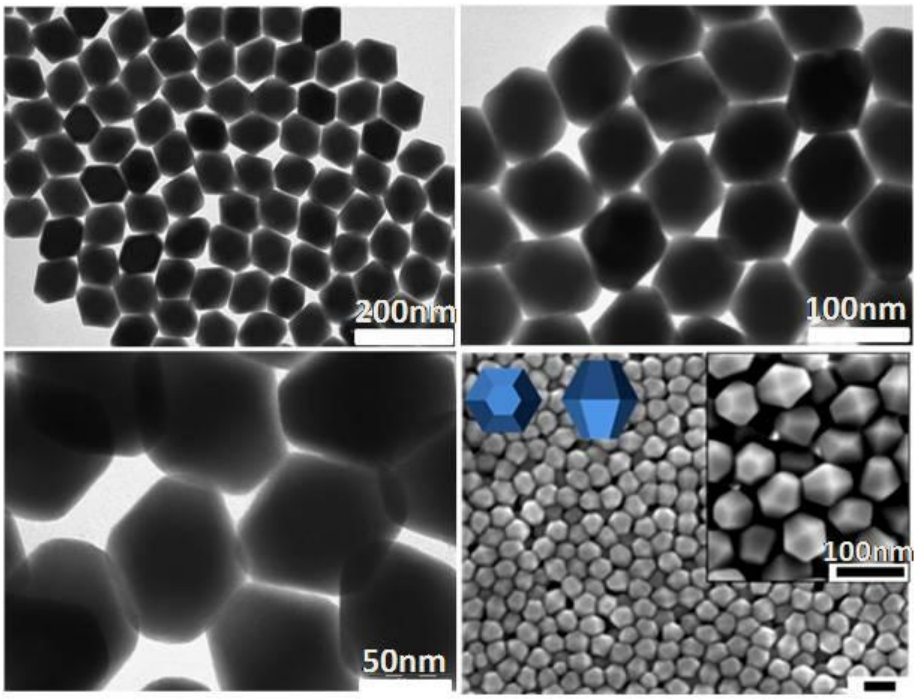

Figure 12. The elongated tetradecahedral nanocrystals obtained in the concentration of Cu as 0.5 M.

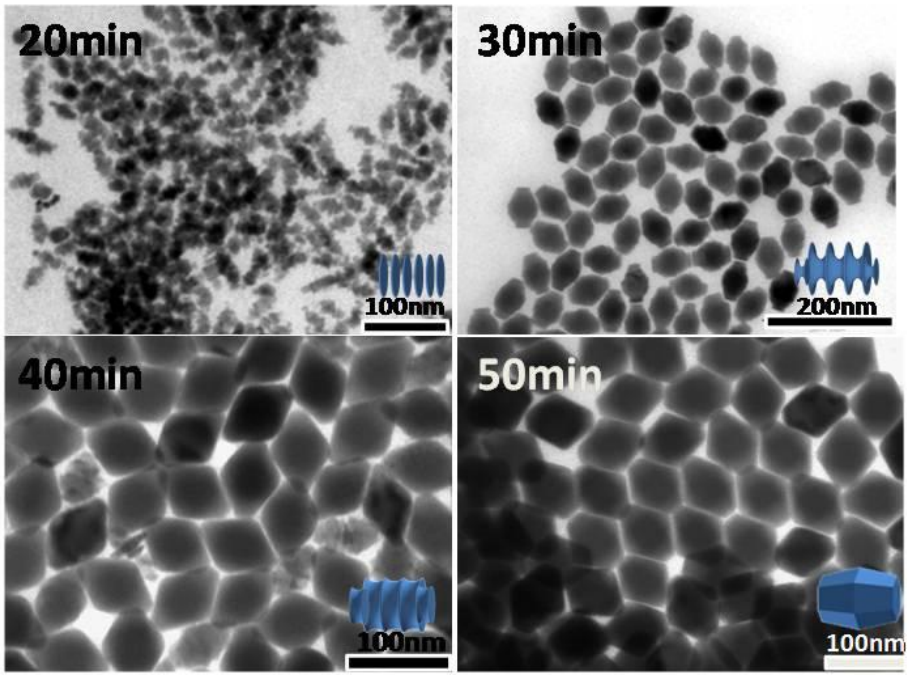

Figure 13. The particles obtained at the different reaction time and the TEM pictures showing the morphology evolution of the elongated tetradecahedrons.

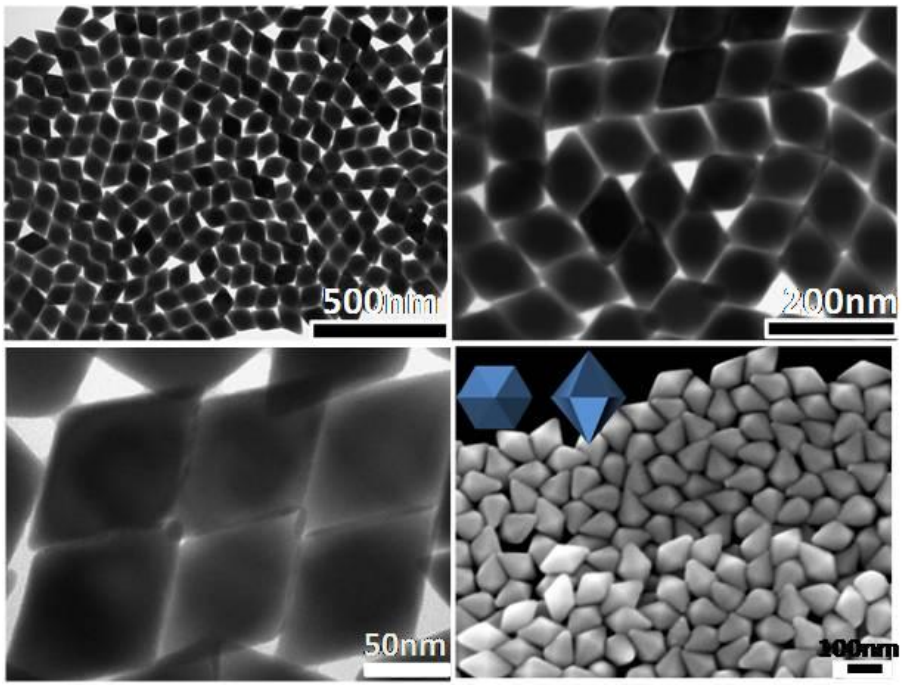

Figure 14. The elongated tetradecahedral nanocrystals obtained in the concentration of Cu as 0.5 M.

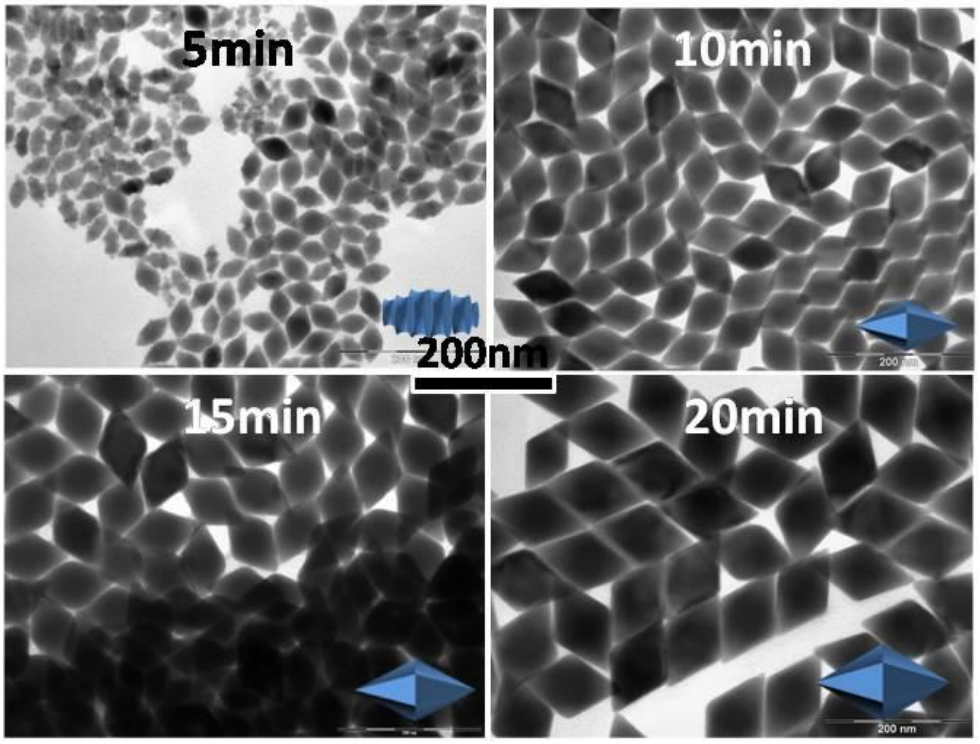

Figure 15. The particles obtained at the different reaction time and the TEM pictures showing the morphology evolution of the elongated tetradecahedrons.

Decahedrons of $Cu_{2-x}S$:

It's obviously observed that at increasingly higher Cu precursor concentrations like 0.5 M, large assemblies of polymers were initially formed and thus, more elongated tetradecahedrons were finally obtained. In this case, the ratio between Cu and S precursor was 1:2 which means there is still room to increase the concentration of Cu precursor. When 8mmol or 10mmol Cu precursor added in the synthesis, big dodecahedrons were observed in the TEM images as shown in Figure 14. Now the ratio reached the limit as 1:1 and the relatively saturated Cu concentration induced the formation of large enough assemblies (Figure 15, 20 min) which resulted in dodecahedrons.

Due to the low nucleation rate of the present synthetic route, the relatively high monomer concentration remaining in solution after nucleation ensured a moderately slow but continuous growth of the nanoparticles. Such slow growth rates allowed an accurate size control of the prepared nanocrystals by altering the Cu concentration, reaction time and temperature, as shown in Figure 16.

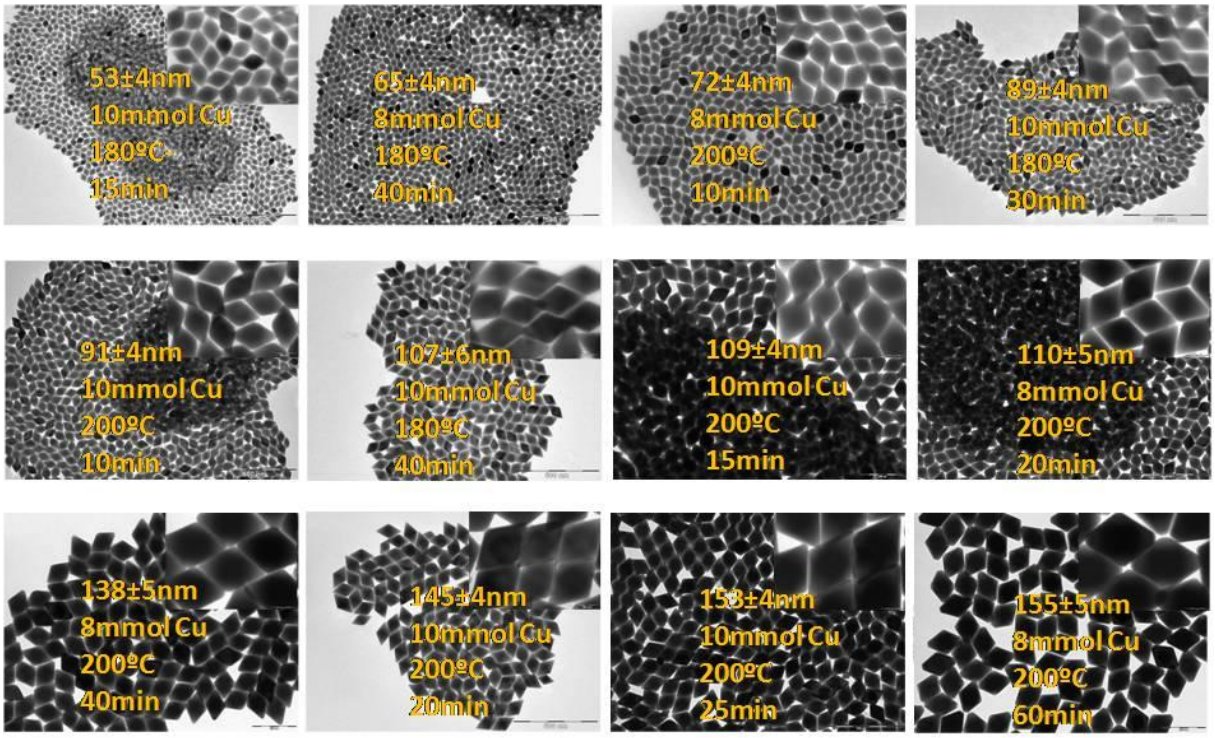

Figure 16. The TEM images of dodecahedral nanocrystals with varied size obtained at the different reaction times, reaction temperatures and in the condition with different Cu concentrations.

3.2.2 The morphology evolution and the growth mechanism from spherical to polyhedral geometries

In general, we can prepare the shape-controlled $Cu_{2-x}S$ nanoparticles by simply tuning the precursor concentration and synthesis conditions as additionally summarized in table 1.

$CuCl_2 \cdot 2H_2O$ (mmol)	0.5	0.5	1	2	5	8
TBDS (mmol)	0	5	5	5	5	5
DDT (mmol)	5	0	0	0	0	0
Total amount of S(mmol)	10	10	10	10	10	10
Cu:S ratio	0.05:1	0.05:1	0.05:1	0.2:1	0.5:1	0.8:1
OLA (g)	10	12	12	12	12	12
Reaction T (^oC)	180	210	200	200	200	200
Reaction time (min)	60	20	40	60	60	60
Morphology	Sphere	Disks	Thin Tetradecahedron	Tetradecahedron	Elongated Tetradecahedron	Dodecahedron

The reaction of copper chloride with an excess of TBDS initially yields $Cu_{2-x}S$ spherical nanoparticles (Figure 17A) as well. Due to their low crystallinity, their phase could not be unambiguously identified. X-ray diffraction pattern could be matched with that of chalcocite (Cu_2S), as previously assigned,[20] but also with that of roxbyite ($Cu_{1.78}S$). The determination of the chemical composition of the nanocrystals by spectroscopy techniques was particularly imprecise because of the large concentration of sulfur and copper complexes which remained un-

reacted and were extremely difficult to remove. The slow nanoparticle growth rates obtained by the present route at relatively low temperatures (≤ 200 ºC) and precursor concentrations (0.05 M) allowed following their gradual morphology evolution.

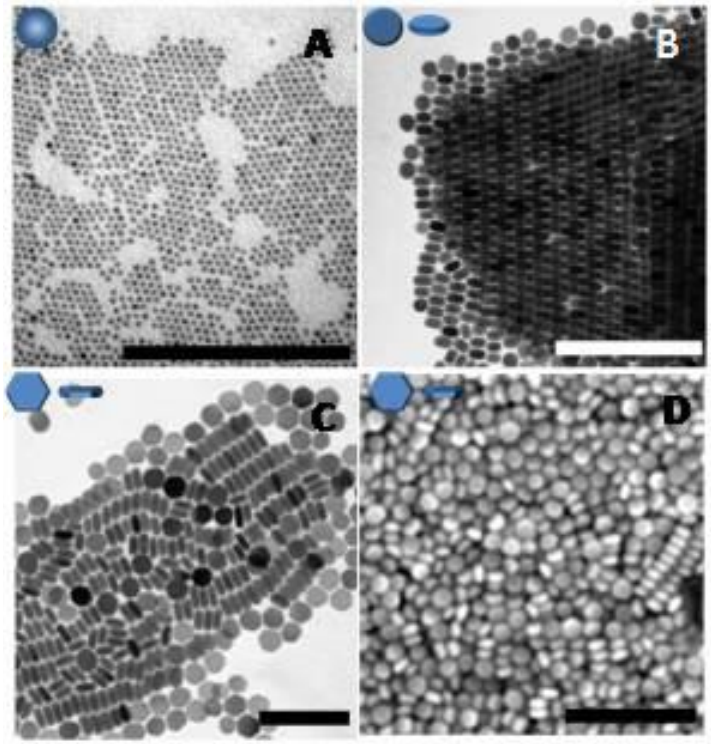

Figure 17. TEM (A-C) and SEM (D) images of $Cu_{2-x}S$ nanoparticles with various morphologies: (A) spherical; (B) circular nanodisks; (C) and (D) hexagonal nanodisks. Scale bars = 200 nm.

Spherical nanocrystals evolved into circular nanodisks (Figure 17B) at early reaction times. Here it is worth to note that the sphere to disk transition could be delayed and even suppressed by introducing thiols in the reaction mixture as we showed in the previous discussion. With the reaction time, circular nanodisks became faceted in 6 equivalent directions, resulting in hexagonal nanodisks (Figure 17C). The improved crystallinity of the nanodisks allowed the identification of their crystal phase as roxbyite ($Cu_{1.78}S$) as indicated in Figure 18. For thick

enough nanodisks, the faceting of their lateral surface was also thermodynamically favoured, and the nanodisks became thin tetradecahedrons.

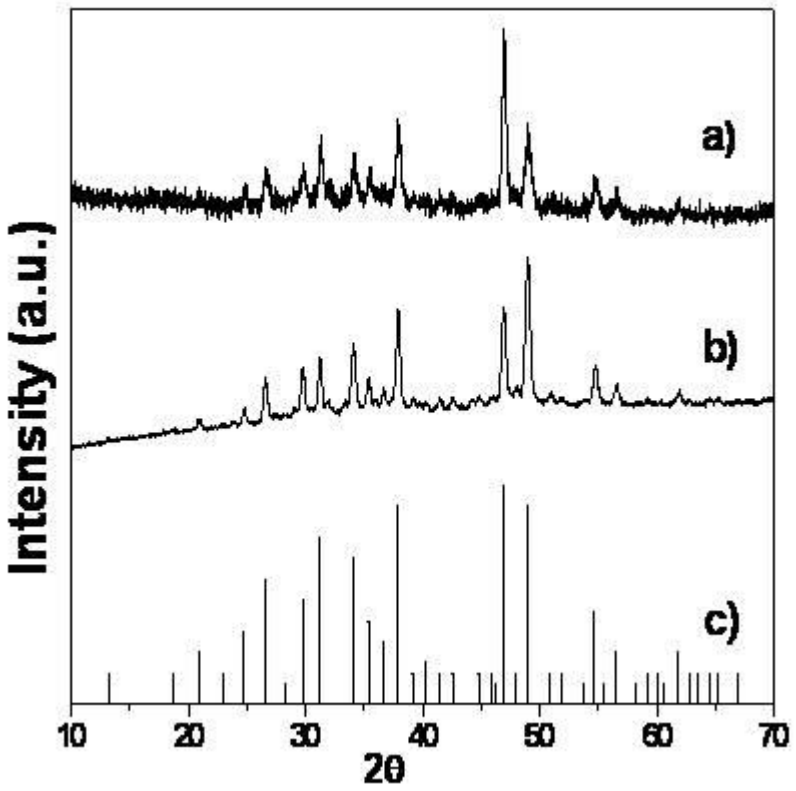

Figure 18. XRD patterns of the nanodisks synthesized at a) 180 ºC, 40 min and b) 200 ºC, 20 min. c) Reference pattern corresponding to monoclinic roxbyite (JCPDS no. 23-958)

As we shown in the above section, the amount of Cu precursor used for the preparation of spheres and nanodisks are always 0.5 mmol which means the very low concentration of Cu as 0.05 M. A change of scenario was obtained when modifying the Cu concentration in solution. In the presence of relatively elevated Cu concentrations (0.1–1 M), high densities of thin nanoplates were initially formed. Probably driven by dipole–dipole interactions,[26] thin nanoplates assembled face-to-face into dimers, trimers or quadrumers, depending on their concentration

(Figure 19A and B). In Figure 20 of the HRTEM images, it is clearly seen how the particles are composed of multiple crystals in perfect epitaxy but clearly separated by junctions or planar defects (white arrows in the image). Also as revealed by the FFTs of each respective crystal, no disorientation is appreciated respect to the common longitudinal axis. It's necessary to point out that some holes were created during an oxygen plasma treatment applied to clean the samples from organics.

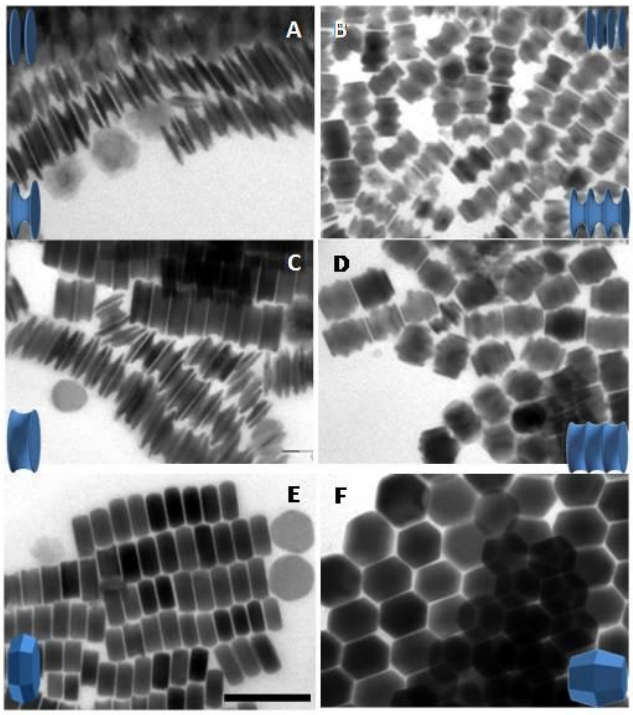

Figure 19. TEM images showing the morphology evolution of $Cu_{2-x}S$ nanoparticles with the reaction time; from nanoplates assembled in dimmers and quadrumers to tetradecahedral and dodecahedral nanocrystals. (A),(C) and (E) [Cu]=0.1 M; (B), (D) and (F) [Cu]=0.2 M. All figures have the same scale bar = 100 nm.

The relatively low growth rate of the present system allowed the formed assemblies to continue growing in a still rather concentrated solution. In such assemblies, the crystal growth took place preferentially in between the pilled nanoplates, fusing them together into single

nanoparticles (Figure 19C and D). With the reaction time elongated, these polycrystalline nanoparticles restructured into single-crystal domains. Such nanocrystals gradually became faceted, adopting a tetrahedral shape (Figure 19E and F).

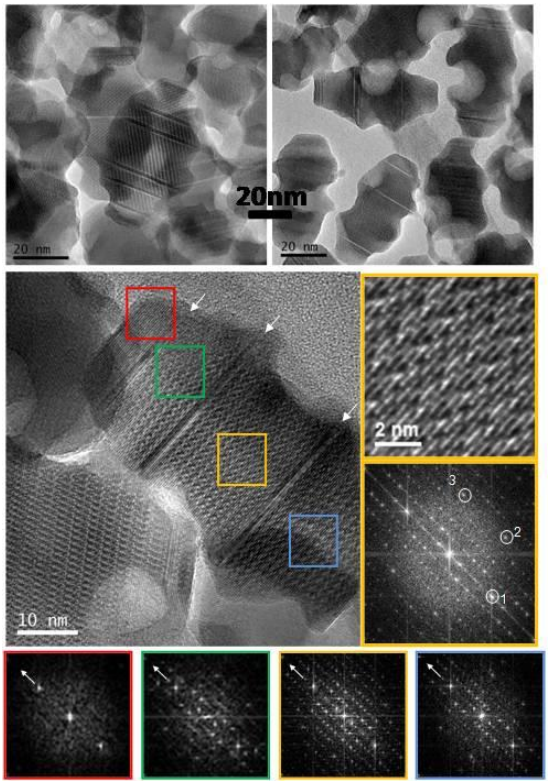

Figure 20. HRTEM images of the nanoparticles obtained from the assembly of thin nanoplates at the early stages of formation of $Cu_{2-x}S$ tetrahedrons. The holes were induced by an oxygen plasma treatment in order to clean the samples from organics as we mentioned in the text.

At increasingly higher precursor concentrations, larger assemblies were initially formed and thus, more elongated tetradecahedrons were finally obtained (Figure 21C and D). In the limit, large enough assemblies resulted in the formation of dodecahedrons (Figure 21E and F).

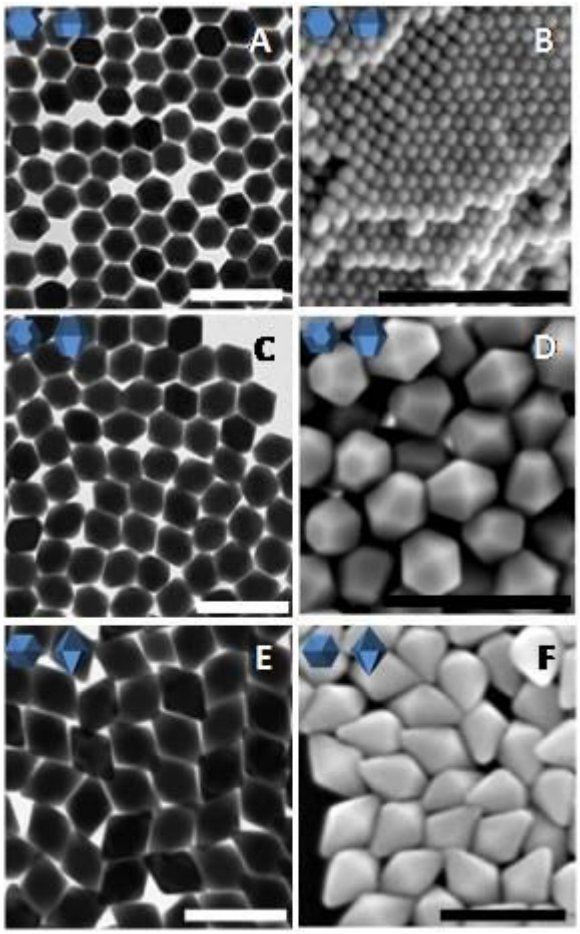

Figure 21. TEM (left) and SEM (right) images of $Cu_{1.96}S$ nanoparticles: (A) and (B) small tetradecahedrons; (C) and (D) elongated tetradecahedrons; (D) and (E) dodecahedrons. Scale bars = 200 nm.

However, the increase of the copper precursor concentrations not only influenced the particle size and morphology, but also promoted a higher incorporation of this element in the nanocrystal structure. This increase of the copper uptake by the nanoparticles translated into a change of crystal phase, from the monoclinic roxbyite $Cu_{1.78}S$ identified in the faceted nanodisks obtained at relatively low copper concentrations (as shown in Figure 18), to the still monoclinic djurleite $Cu_{1.96}S$ observed in the tetrahedral and dodecahedral nanoparticles obtained at precursor concentrations above 0.1 M (Figure 22).

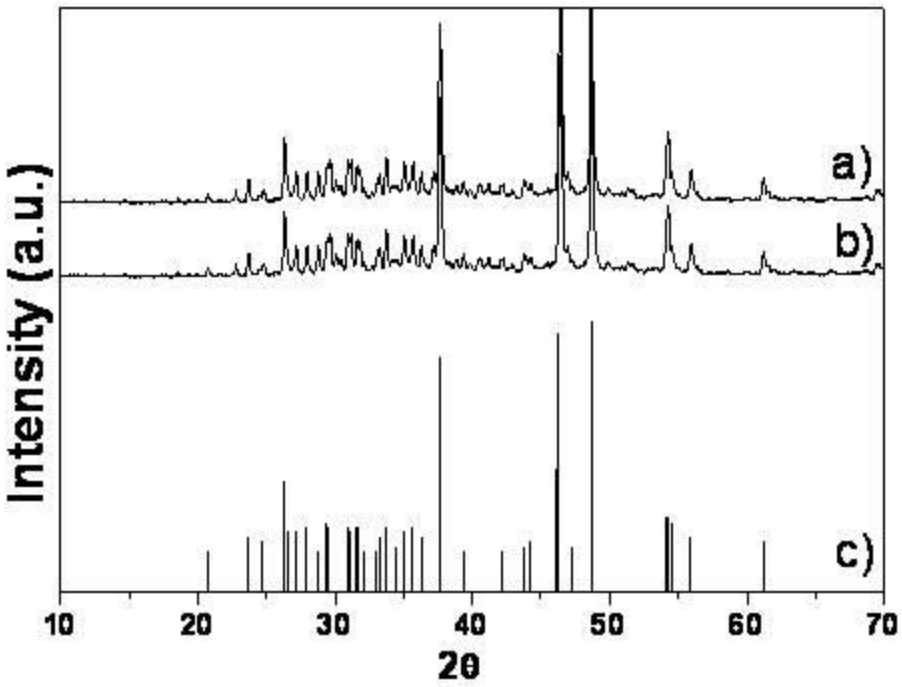

Figure 22. XRD patterns of the dodecahedron and tetradecahedrons obtained in the higher jconcentration of [Cu] as (a) 0.8 M and (b) 0.5 M, respectively. (c) Reference pattern corresponding to the monoclinic Djurleite (JCPDS No. 23-959).

HRTEM analysis of the thin tetradecahedrons showed them to be strongly faceted along the <100> top and bottom planes and having <111> and <120> lateral facets (Figure 23, the bottom line). Tetradecahedron elongation took place along the <100> direction. (Figure 24 and 25) In the limit, dodecahedrons were obtained when the elongation of the tetradecahedons in the <100> direction resulted in the suppression of the <100> facets (Figure 23, the top line). Here the 3D atomic models are created by software called "Rhodius" from the University of Cadiz (UCA).[56]

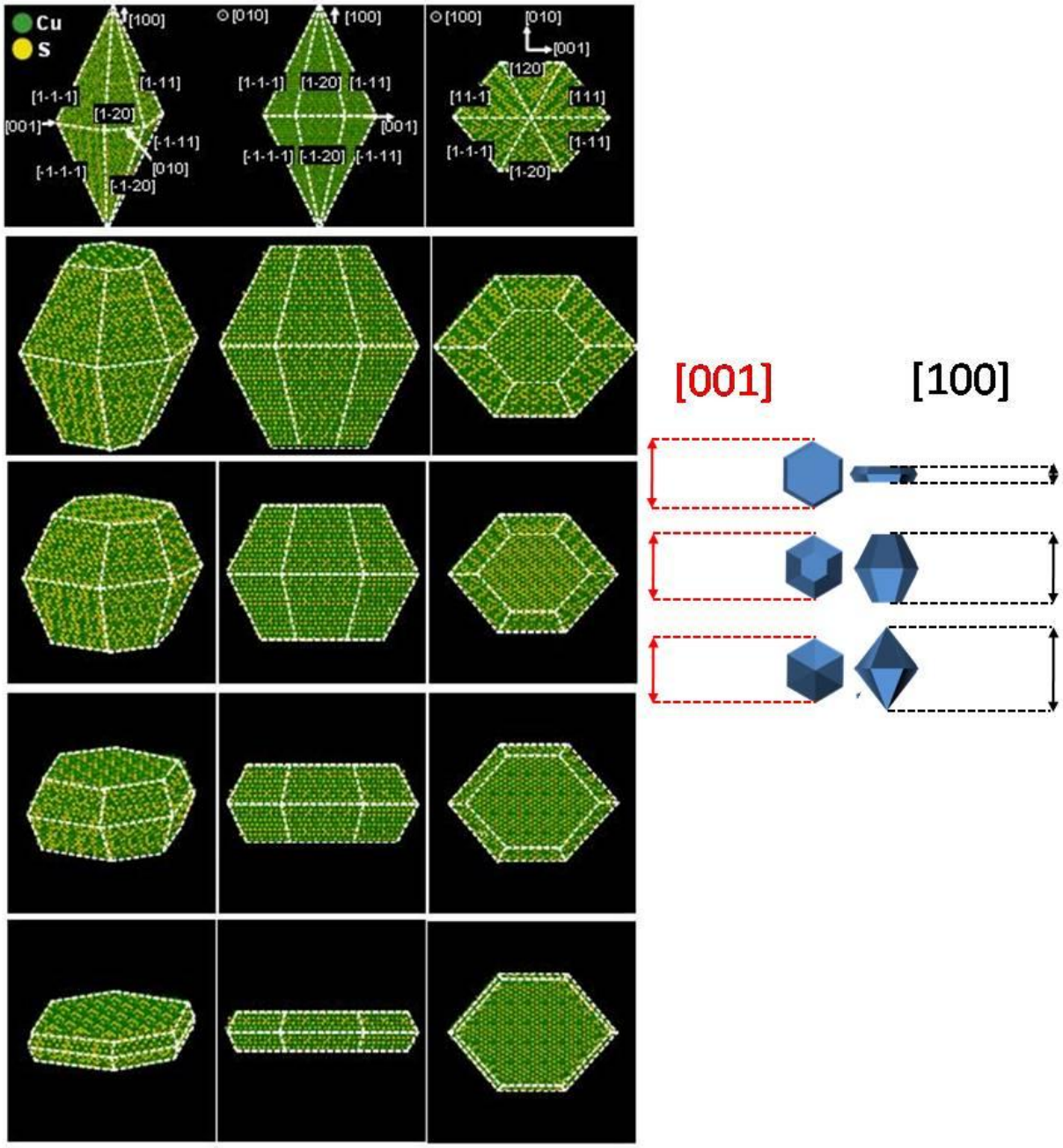

Figure 23. Scaled (1:5) 3D atomic models of $Cu_{1.96}S$ djurleite nanoparticles with different morphologies, from hexagonal nanodisks to dodecahedrons. The elongation of the tetradecahdeons in the <100> direction resulted in the suppression of the <100> facets which resulted in the formation of dodecahedrons.

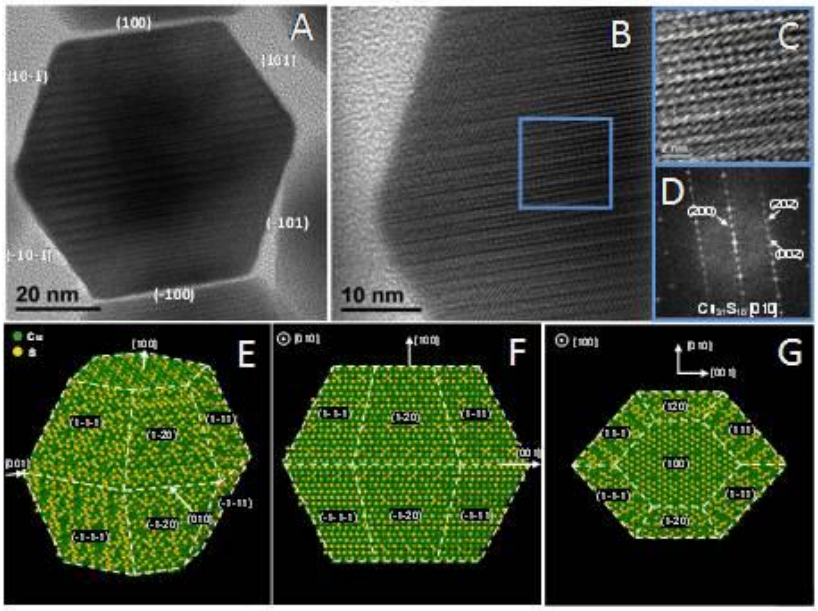

Figure 24. HRTEM image (A,B,C) of a $Cu_{1.96}S$ tetradecahedron, with power spectrum structure analysis (D), and corresponding scaled (1:5) 3D atomic model in perspective (E), frontal (F) and top (G) views.

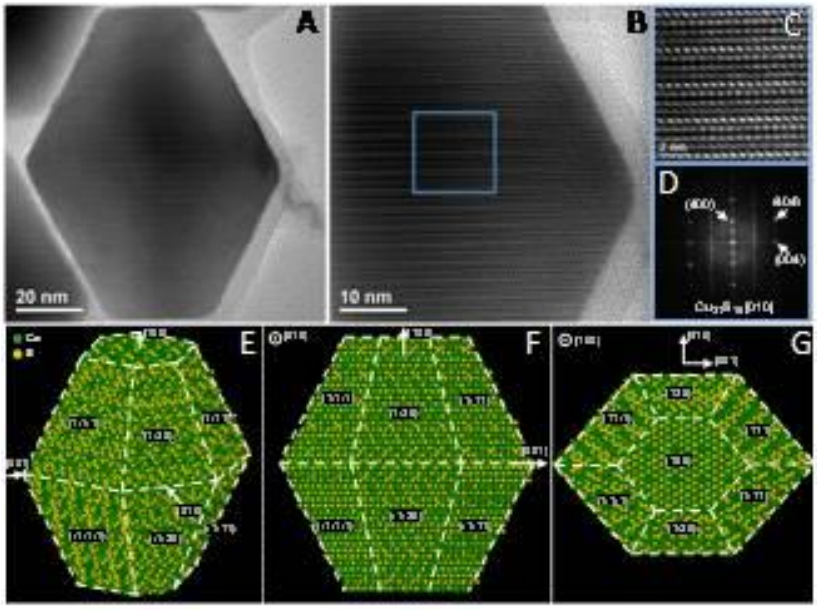

Figure 25. HRTEM image (A) and details (B,C) of a $Cu_{1.96}S$ tetradecahedron, with power spectrum structure analysis (D), and corresponding scaled (1:5) 3D atomic model in perspective (E), frontal (F) and top (G) views.

To summarize, the nanodisks encountered dimension increase in diameter due to the growth along [001] direction and on the other hand, the constant growth along [100] direction resulted in the formation of polyhedrons. As shown in Figure 26 of the histograms, the size in the [100] crystal direction corresponds with that in the axial direction. That is the disk thickness and the long dodecahedron dimension. In red, the size in the [001] crystal direction corresponds to the disk diameter and to the short dimension of the dodecahedral particles.

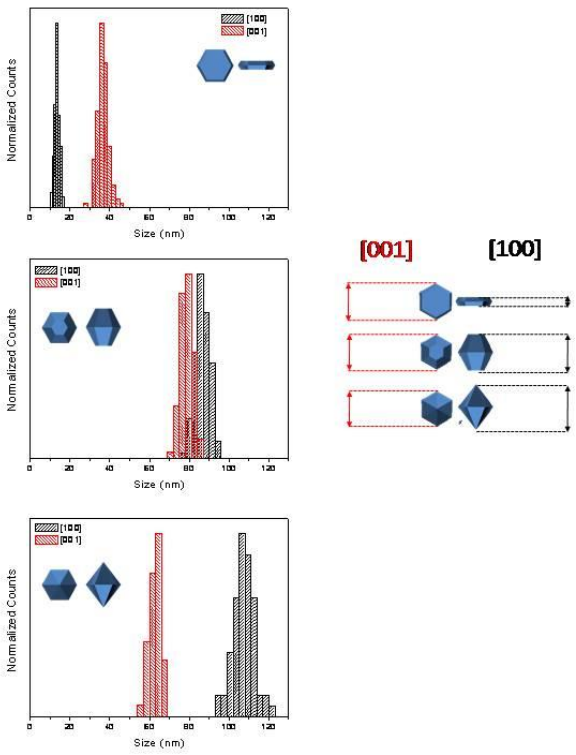

Figure 26. Histograms showing the typically-obtained nanocrystal size distributions. Top, middle and bottom histograms correspond to nanodisks, tetradecahedral nanocrystals and dodecahedrons, respectively.

3.3 Application as a cathode in all-vanadium redox flow batteries (VRB)

The performance of $Cu_{2-x}S$ nanocrystals with different shapes as a cathode in all-vanadium redox flow batteries (VRB) was also tested. The efficiency of this type of battery is usually limited by the rate and potential of the $[VO]^{2+}/[VO_2]^{+}$ cathodic reaction. $Cu_{2-x}S$ nanocrystals were thoroughly purified, deposited on a substrate and fixed by Nafion. Their electrochemical activity was characterized in an inert atmosphere by means of cyclic voltametry. Their characteristics were compared with those obtained for a polyacrylonitrile-derived graphite felt, which is a material widely used as VRB cathode. Notice how the voltage difference between the peaks corresponding to the reduction and oxidation events and its dependence with the scan rate are much lower for the electrodes containing $Cu_{2-x}S$ nanocrystals than for the naked graphite. Lower oxidation potentials were systematically obtained for $Cu_{2-x}S$ nanocrystals when compare to the PAN-based graphite felt (Figure 27). At a 2 mV s^{-1} scan rate, the oxidation potential was found at 0.72 V for the PAN-based graphite felt and at 0.44 V for the electrode containing $Cu_{2-x}S$ nanocrystals. This result denotes faster electrocatalytic kinetics of the oxidation process for the electrode containing $Cu_{2-x}S$ nanocrystals. The difference of potential between the oxidation and reduction peaks was 0.36 V for the PAN-based graphite felt and 0.10 V for the $Cu_{2-x}S$ electrode. Furthermore, the ratio between the currents at the oxidation and reduction peaks for $Cu_{2-x}S$ nanocrystals was close to unity and changed moderately with the scan rate. These experimental results pointed towards a significant performance improvement in terms of reversibility of the $[VO]^{2+}/[VO_2]^{+}$ redox process with the use of $Cu_{2-x}S$ nanocrystals. However, the currents measured with $Cu_{2-x}S$ cathodes were lower than those obtained with PAN-based graphite felts.

Thus, a further optimization of the density and dispersion of the nanocrystals and their surface conditioning is still required.

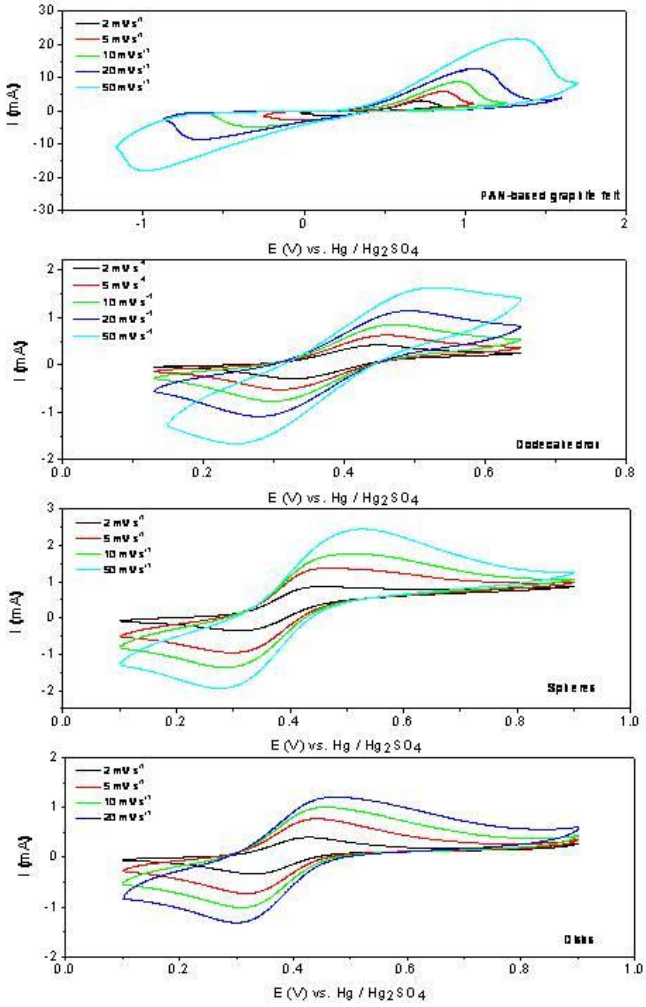

Figure 27. Cyclic voltammograms at different scan rates obtained using the PAN-based graphite felt (top) and the different $Cu_{2-x}S$ nanocrystal morphologies supported on a planar graphite substrate (as indicated on each graph).

In Figure 28, the voltage of the reduction and oxidation peaks obtained with the different nanocrystal geometries is plotted as a function of the scan rate. No clear differences in the

oxidation and reduction potentials were obtained between the different nanocrystal geometries, pointing towards the existence of similar reaction mechanisms.

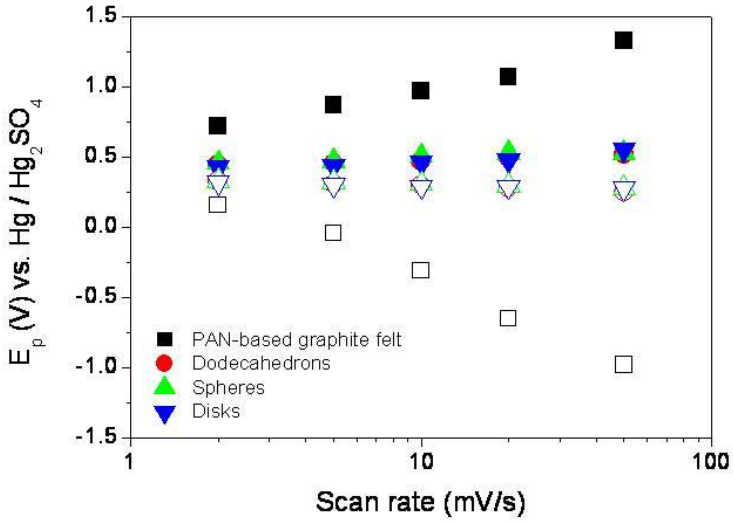

Figure 28. Voltage of the cathodic and anionic peaks as a funcion of the scan rate obtained from the different nanocrystal morphologies and the PAN-based graphite felt.

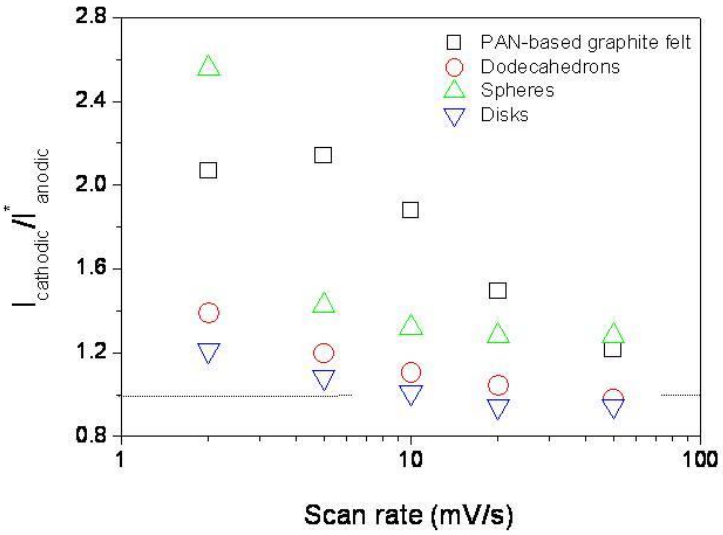

Figure 29. Anodic vs. cathodic peak current ratio obtained with the different nanocrystal morphologies and the PAN-based graphite felt.

Figure 29 shows the anodic vs. cathodic current ratio as a function of the scanning rate. In a reversible process, the ratio between the current intensities of the anodic and cathodic peaks should be close to 1.[57] Notice how electrodes containing $Cu_{2-x}S$ nanocrystals usually showed better reversibility than naked graphite electrodes.

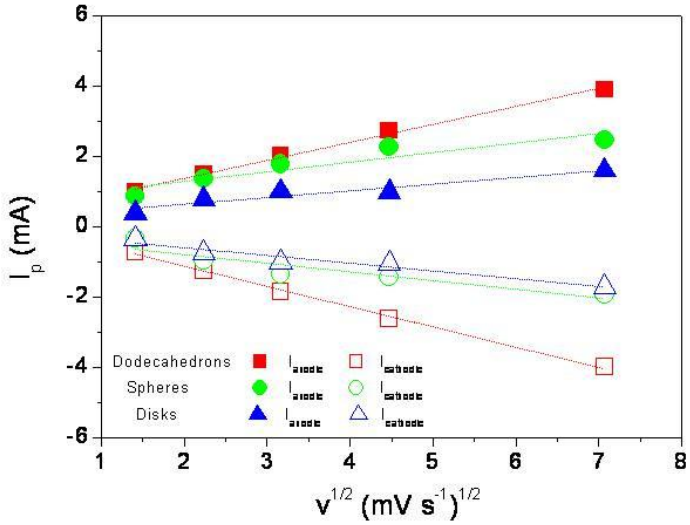

Figure 30. Current at the redox peaks as a function of the square root of the scan rate.

Furthermore, in a reversible process, the forward scan peak current should be proportional to the square root of the scan rate.[57] Figure 30 shows the dependence of the current with the square root of the scan rate. Lineal dependences were obtained for all electrodes containing $Cu_{2-x}S$ nanocrystals, which pointed towards a vanadium-diffusion limited mechanism. In this regime, the Randles-Sevcik equation can be used to determine the apparent diffusion coefficients of the vanadium species in the electrodes:

$$i_p = 2.686 \times 10^5 n^{3/2} A D^{1/2} C v^{1/2}$$

where i_p is the peak current, n the number of electrons transferred in the redox reaction, A is the electrode area, D the diffusion coefficient, C the concentration of vanadium in solution and v the

scan rate. Among the different morphologies, the highest diffusion coefficients were obtained with the electrodes containing $Cu_{2-x}S$ dodecahedral nanocrystals: 2 x 10^{-8} cm^2 s^{-1}. Nevertheless, no conclusive differences in the performance of the distinct morphologies can be obtained from these preliminary measurements.

The limited current intensities and the associated low diffusion coefficients obtained were related to the presence of the Nafion layer and the small surface area of the electrodes containing $Cu_{2-x}S$ nanocrystals. The Nafion layer was required to prevent the degradation of the $Cu_{2-x}S$ nanocrystals. However, its thickness needs to be optimized to maximize the current density. On the other hand, the use of 3D porous graphite supports will highly increase the nanocrystal dispersion and maximizing the number of reaction sites accessible for the vanadium species. In this sense, notice that the porous 1 cm^3 graphite felt used here for comparison had a surface area between 2 and 3 orders of magnitude larger than the planar graphite electrode, which could account for a 100-1000 fold increase in the current intensity. Another parameter which will need optimization when using 3D electrode supports is the density of $Cu_{2-x}S$ nanocrystals. Too high densities could led to saturation of the surface and thus to poorer electrochemical performance. Also the surface dispersion of the nanoparticles needs to be optimized and their aggregation prevented. This may be especially important and challenging for $Cu_{2-x}S$ nanodisks, which tend to stack face to face.

3.4 Conclusions

In conclusion, tuning the precursor concentration and reaction conditions, $Cu_{2-x}S$ nanoparticles with different morphologies were obtained. In particular, tetradecahedrons and dodecahedrons

were synthesized at relatively high precursor concentrations by means of an oriented attachment and growth mechanism involving the assembly of nanoplates into dimers, trimers, quadrumers and even larger assemblies, and their recrystallization into faceted single-crystal nanoparticles. In terms of reversibility, the presence of $Cu_{2-x}S$ nanocrystals significantly reduced the reduction potentials and increased the reversibility of the process. So these $Cu_{2-x}S$ nanocrystals showed promising electrocatalytic performace as cathodes in all-vanadium redox flow batteries and we believe the present work to provide the basics for developing more efficient VRB using $Cu_{2-x}S$ nanocrystals as catalyst in the cathodes.

3.5 References

(1) Zeng, H.; Sun, S. *Ad*v. *Funct. Mater.* **2008**, *18*, 391-400.

(2) Cozzoli, P. D.; Pellegrino, T.; Manna, L. *Chem. Soc. Re*v. **2006**, *35*, 1195-1208.

(3) Liu, N.; Prall, B. S.; Klimov, V. I. *J. Am. Chem. Soc.* **2006**, *128*, 15362-15363.

(4) Zhang, J.; Jin, S.; Fry, H. C.; Peng, S.; Shevchenko, E.; Wiederrecht, G. P.; Rajh, T. J. Am. Chem. Soc. **2011**, *133*, 15324–15327.

(5) Yin, Y.; Alivisatos, A. P. *Nature* **2005**, *437*, 664-670

(6) Manna, L.; Milliron, D. J.; Meisel, A.; Scher, E. C.; Alivisatos, A. P. *Nat. Mater.* **2003**, *2*, 382-385.

(7) Murray, C. B.; Sun, S. H.; Doyle, H.; Betley, T. *MRS. Bull.* **2001**, *26*, 985-991.

(8) Shevchenko, E. V.; Bodnarchuk, M. I.; Kovalenko, M. V.; Talapin, D. V.; Smith, R. K.; Aloni, S.; Heiss, W.; Alivisatos, A. P. *Ad*v. *Mater.* **2008**, *20*, 4323-4329.

(9) Milliron, D. J.; Hughes, S. M.; Cui, Y.; Manna, L.; Li, J.; Wang, L.-W.; Alivisatos, A. P. *Nature* **2004**, *430*, 190-195.

(10) Cho, K. S.; Talapin, D. V.; Gaschler, W.; Murray, C. B. *J. Am. Chem. Soc.* **2005**, *127*, 7140-7147.

(11) Dorfs, D.; Hartling, T.; Miszta, K.; Bigall, N. C.; Kim, M. R.; Genovese, A.; Falqui, A.; Povia, M.; Manna, L. *J. Am. Chem. Soc.* **2011**, *133*, 11175-11180.

(12) Zhao, Y.; Pan, H.; Lou, Y.; Qiu, X.; Zhu, J.; Burda, C. *J. Am. Chem. Soc.* 2009, *12*, 4253-4261.

(13) Luther, J. M.; Jain, P. K.; Ewers, T.; Alivisatos, P. A. *Nat. Mater.* **2011**, *10*, 361-366.

(14) Gurin, V. S.; Prokopenko, V. B.; Alexeenko, A. A.; Wang, S.; Yumashev, K. V.; Prokoshin, P. V. *Int. J. Inorg. Mater.* **2001**, *3*, 493–496.

(15) Evans, H. T. Jr. *Science* **1979**, 203, 356-358.

(16) Sigman, M. B.; Ghezelbash, J. A.; Hanrath, T.; Saunders, A. E.; Lee, F.; Korgel, B. A. *J. Am. Chem. Soc.* 2003, *125*, 16050-16057.

(17) Harbottle, J. E.; Fisher, S. B. *Nature* **1982**, *299*, 139-140.

(18) Skirma, A.; Vitalijus, J. *Mater. Sci-Medzg.* **2012**, *18*, 112–118.

(19) Mumme, W. G.; Sparrow, G. J.; Walker, G. S. *Mineral. Mag.* **1988**, *52*, 323-330.

(20) Li, S.; Wang, H.; Xu, W.; Si, H.; Tao, X.; Lou, S.; Du, Z.; Li, L. S. *J. Colloid Interface Sci.* **2009**, *330*, 483-487.

(21) Han, W.; Yi, L.; Zhao, N.; Tang, A.; Gao, M.; Tang, Z. *J. Am. Chem. Soc.* **2008**, *130*, 13152-13161.

(22) Chen, L.; Chen, Y. B.; Wu, L. M. *J. Am. Chem. Soc.* 2004, *126*, 16334-16335.

(23) Liu, Z.; Xu, D.; Liang, J.; Shen, J.; Zhang, S.; Qian, Y. *J. Phys. Chem. B* **2005**, *109*,10699-10704.

(24) Chen, Y. B.; Chen, L.; Wu, L. M. *Chem. Eur. J.* **2008**, *14*, 11069-11075.

(25) Du, X. S.; Yu, Z. Z.; Dasari, Z.; Ma, J.; Meng, Y. Z.; Mai, Y. W. *Chem. Mater.* **2006**, *18*, 5156-5158.

(26) Zhuang, Z.; Peng, Q.; Zhang B.; Li, Y. *J. Am. Chem. Soc.* **2008**, *130*, 10482-10483.

(27) Lim, W. P.; Wong, C. T.; Ang, S. L.; Low, H. Y.; Chin, W. S. *Chem. Mater.* 2006, *18*, 6170-6177.

(28) Zhang, H.; Zhang, Y.; Yu, J.; Yang, D. *J. Phys. Chem. C* **2008**, *112*, 13390-13394.

(29) Ghezelbash, A.; Korgel, B. A. Langmuir. 2005, 21, 9451-9456.

(30) Du, W.; Qian, X.; Ma, X.; Gong, Q.; Cao, H.; Yin, J. *Chem. Eur. J.* **2007**, *13*, 3241-3247.

(31) Li, X.; Shen, H.; Li, S.; Niu, J.; Wang, H.; Li, L. *J. Mater. Chem.* **2010**, *20*, 923–928.

(32) Wu, Y.; Wadia, C.; Ma, W.; Sadtler, B.; Alivisatos, A. P. *Nano. Letter*. **2008**, *8*, 2551–2555.

(33) Lou, Y.; Samia, A. C. S.; Cowen, J.; Banger, K.; Chen, X.; Lee, H.; Burda, C. *Phys. Chem. Chem. Phys.* **2003**, *5*, 1091–1095.

(34) Johansson, J.; Kostamo, J.; Karppinen, M.; Niinisto, L. *J. Mater. Chem*. **2002**, *12*, 1022–1024.

(35) Cordova, R.; Gomez, H.; Schrebler, R.; Cury, P.; Orellana, M.; Grez, P. *Langmuir.* **2002**, *18*, 8647–8654.

(36) Zhao, Y.; Pan, H.; Lou, Y.; Qiu, X.; Zhu, J.; Burda, C *J. Am. Chem. Soc.* **2009**, *131*, 4253–4261.

(37) Kuzuya, T., Tai, Y., Yamamuro, S., Sumiyama, K. Sci. Technol. *Adv. Mater.* **2005**, *6*, 84–90.

(38) Zhang, H. T., Wu, G., Chen, X. H. *Langmuir* 2005, *21*, 4281–4282.

(39) Zhang, J. Z. *J. Phys. Chem. B.* **2000**, *104*, 7239–7253.

(40) Du, X. S.; Yu, Z. Z.; Dasari, A.; Ma, J.; Meng, Y. Z.; Mai, Y. W. *Chem. Mater*. **2006**, *18*, 5156–5158.

(41) Larsen, T. H.; Sigman, M.; Ghezelbash, A.; Doty, R. C.; Korgel, B. A. *J. Am. Chem. Soc.* **2003**, *125*, 5638-5639.

(42) Roy, P.; Srivastava, S. K. *Mater. Lett.* **2007**, *61*, 1693–1697.

(43) Wu, C.; Yu, S. H.; Chen, S.; Liu, G.; Liu, B. *J. Mater. Chem.* **2006**, *16*, 3326–3331.

(44) Zhu, H.; Ji, X.; Yang, D.; Ji, Y.; Zhang, H. *Micropor. Mesopor. Mat.* **2005,** *80*, 153–156.

(45) Huang, K. L.; Li, X. G.; Liu, S. Q.; Tan, N.; Chen, L. Q. *Renew. Energ.* **2008,** *33*, 186–192.

(46) Fabjan, C.; Garche, J.; Harrer, B.; Jorissen, L.; Kolbeck, C.; Philippi, F.; Tomazic, G.; Wagner, F. *Electrochim. Acta.* **2001,** *47*, 825- 831

(47) Skyllaskazacos, M.; Rychcik, M.; Robins, R. G.; Fane, A. G.; Green, M. A. *J. Electrochem. Soc.* **1986,** *133*, 1057-1058.

(48) Ponce de Leon, C.; Frias-Ferrer, A.; Gonzalez-Garcia, J.; Szanto, D. A.; Walsh, F. C.. *J. Power Sources.* **2006**, *160*, 716-732.

(49) Zhong, S.; Padeste, C.; Kazacos, M.; Skyllas-Kazacos, M. *J. Power Sources.* **1993,** *45*, 29-41.

(50) Zhu, H. Q.; Zhang., Y. M.; Yue, L.; Li, W. S.; Li, G. L.; Shu, D.; Chen, H. Y. *J. Power Sources.* **2008,** *184*, 637-640.

(51) Sun, B.; Skyllas-Kazacos, M. *Electrochim. Acta.* **1991,** *36,* 513-517.

(52) Shao, Y.; Wang, X.; Engelhard, M.; Wang, C.; Dai, S.; Liu, J.; Yang, Z.; Lin, Y. *J. Power Sources.* **2010,** *195*, 4375-4379.

(53) Yamamuro, S.; Farrell, D. F.; Majetich, S. A. *Phys. Rev. B.* **2002**, *65*, 224431–224440.

(54) Puntes, V. F.; Zanchet, D.; Erdonmez, C. K.; Alivisatos, A. P. *J. Am. Chem. Soc.* **2002**, *124,* 12874–12880.

(55) Saunders, A. E.; Ghezelbash, A.; Smilgies, D. M.; Sigman, M. B. Jr.; Korgel, B. A. *Nano. Lett.* **2006**, *6*, 2959-2963.

(56) Bernal, S.; Botana, F. J.; Calvino, J. J.; Lopez-Cartes, C.; Perez-Omil, J. A.; Rodrõguez-Izquierdo, *J. M. Ultramicroscopy* **1998**, *72*, 135-164.

(57) Gosser, D. K. Jr. (Ed), Cyclic Voltammetry, VCH Publishers, **1993**.

Chapter 4

Metal Ions to Control the Morphology of CuSe nanoparticles

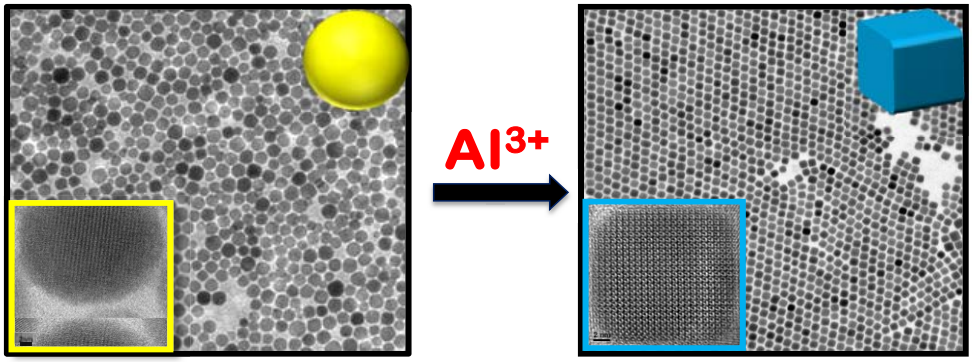

4.1 Introduction

It is in large part through the surface that nanocrystals (NCs) interact with neighboring NCs and the medium. Catalytic, electronic, optoelectronic and thermoelectric performance of NCs and nanocrystalline materials strongly rely on the chemical and energy exchange in the form of ions, charge carriers or phonons that take place between NCs themselves and between NCs and the medium. In this sense, numerous applications depend on the organization of the NC last atomic layers. That is, on the type and ratio of the NC facets, i.e. its morphology.

Morphology also controls NC assembly into macroscopic superstructures. In this regard, a particularly interesting geometry for technological applications is that of cubes.[1-4] Nanocubes can

maximize NC packing and produce highly compact films or bulk nanostructured materials. At the same time, nanocubes can form lattice-matched superstructures where all crystallographic domains are oriented in the same direction.[5-6] This may be an important asset in magnetic, electronic, optoelectronic, and thermoelectric applications, where charge carrier or phonon exchange is fundamental.

To control NC morphology, organic molecules that selectively bind to different NC facets are generally used. There are countless examples on the use of aliphatic chains with carboxylic acid, phosphonic acid and amine functional groups to control the morphology of elemental, binary, ternary, and quaternary nanoparticles.[7-12] Some metal ions have also been proved as efficient directors of NC morphology, especially for metal nanoparticles. A particularly illustrative example is that of Pt-based nanocubes. Tungsten,[13-14] iron,[15] cobalt,[16-17] and chromium[18] carbonyls and also iron chloride,[19-21] silver nitrate[22] and silver acetylacetonate[23] have been used to produce Pt nanocubes by manipulating NC nucleation and growth rate in the different crystallographic directions. In many cases, these metal ions did not incorporate in the NC structure and were not detected on the surface or within the final NCs. They just catalysed the nanocube formation, returning afterward to the solution or precipitating as a salt.

Previous studies on the use of foreign metal ions to control NC morphology were focused on metal NCs. However, because the underlying mechanism is a general one, we believe metal ions should be also included in our tool bench as potential morphology drivers of semiconductor NCs. Here in this present work, we investigate an example of the influence of foreign metal ions to control the morphology of a chalcogenide semiconductor: Cu_xSe. In particular, we detail a synthetic route to produce Cu_xSe nanocubes by the incorporation of Al ions in the initial

precursor solution. We also characterize the plasmonic properties of the new copper selenide geometry obtained and demonstrate the potential of the produced Cu_xSe NCs to prepare nananocubes of other semiconductor chalcogenides by cation exchange. This is exemplified by preparing Ag_2Se nanocubes.

Colloidal syntheses of various nanocrystals have been studied extensively and gained much attention during the past two decades.[24-28] Among them, a considerable effort has been put into the synthesis of Cu_XSe nanocrystals. It has both a direct band gap of 2.2 eV and an indirect band gap of 1.4 eV[29] which makes it not only be used as p-type semiconductor due to the copper vacancies in the lattice, but also show tuneable optical absorption behaviour due to the modified density of holes via controlling the x value in Cu_XSe. As one of the superionic conductors, it is considered as a promising material in applications like photovoltaic, photonic devices[29-32] and thermoelectric[33] due to the presence of copper vacancies which is highly dependent on the composition[34] and shape control.[35] Here in this chapter, we demonstrated a well-defined cubic shape of semiconductor copper selenide with strong NIR absorption by the hot-injection colloidal synthesis method. To our best knowledge, since great progress has been achieved regarding to the synthesis of size-, shape-, and assembly-controllable Cu_XSe nanoparticles like nanowire, [32] nanodisk, [30] hexagonal bipyramids and pyramidal-shaped nanocrystals[35] etc., but there is only one paper reported about $Cu_{2-x}Se$ nanocubes.[36] However, actually this paper did not yield uniform particles and on the other hand, the optical property of nanocubes was not investigated either. In fact, a considerable effort has been put in the last years into metal nanocubes synthesis due to their shape dependent properties, [1, 3, 4] especially surface plasmonics. As one of the significant semiconductor nanocrystals, $Cu_{2-x}Se$ has gained intensive research as

well as $Cu_{2-x}S$ used for nanoplasmonics. But all the reports focused on the study of plasmonic resonance with spherical. [3, 29, 34] Here in the present work, the monodisperse Cu_xSe nanocubes with mean edge length of 17.4 ± 0.9 nm were synthesized and their plasmonic properties was characterized as well.

4.2 Results and Discussion

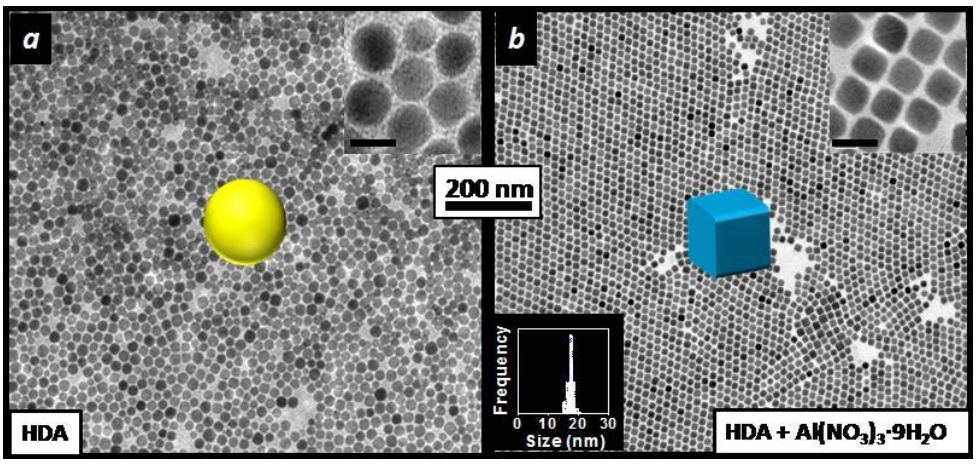

Figure 1. (a) TEM micrograph and particle size distribution of Cu_xSe nanocubes obtained by reacting CuCl with ODE-Se in the presence of HDA and $Al(NO_3)_3 \cdot 9H_2O$ at 180 °C. (b) TEM micrograph of quasi-spherical Cu_xSe NCs obtained by reacting CuCl with ODE-Se in the presence of HDA at 180 °C. Scale bars of inset TEM micrographs corresponding to 20 nm.

Cu_xSe nanocrystals were obtained by the reaction of CuCl with an excess of selenium precursor in the presence of hexadecylamine (HDA). In a typical synthesis, 0.5 mmol of CuCl, 5 mmol HAD and 10 mL of ODE were introduced inside a four-neck flask and heated to 200 °C under argon flow until all precursors were dissolved. The flavescent, transparent solution produced was maintained at 200 °C for 1 h for purification, i.e. to remove oxygen, water and

other low-boiling point impurities. Afterwards, the temperature was set to 180 °C and at this temperature 4 mL of the 0.8M ODE-Se solution in stock was injected through a septum. The mixture was maintained at the reaction temperature to allow the nanocrystals further grow for 5 min before rapidly cooling down the flask to room temperature. The reaction yield was around 80 % for all the synthesis present here. Figure 1a shows a representative transmission electron microscopy (TEM) micrograph of the quasi-spherical Cu_xSe NCs obtained following the above described procedure.

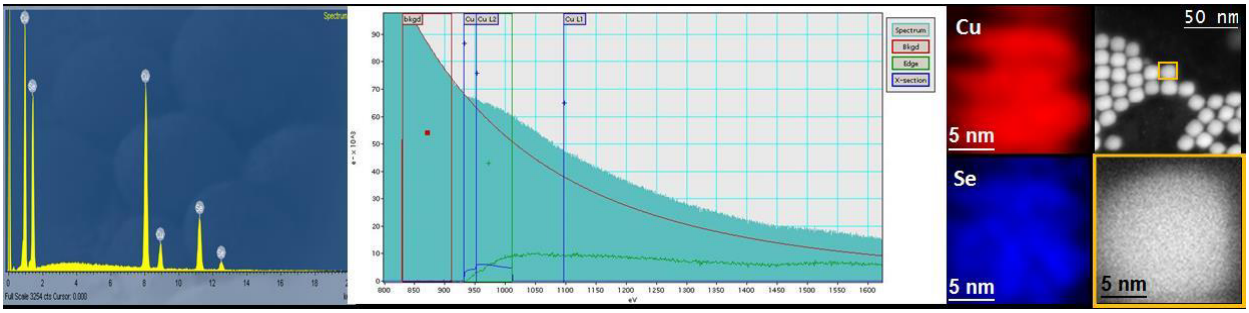

Figure 2. EDX spectrum (left), Raw EELS spectrum (middle) and Se and Cu EELS elemental mapping images of single copper selenide nanocube (right).

In an attempt to prepare $CuAlSe_2$ NCs, we added $Al(NO_3)_3 \cdot 9H_2O$ in the precursor solution. All other parameters were maintained the same. Figure 1b shows a representative TEM micrograph the NCs obtained in the presence of 0.1 mmol of $Al(NO_3)_3$. It displays that the cubic-shaped NCs with a narrow size distribution ~ 5 %, were systematically obtained and indicates that good homogeneity and uniformity were achieved using this approach. To our surprise and initial disappointment, energy dispersive X-ray (EDX) analysis (Figure 2, left) inside a scanning electron microscope (SEM) showed the presence of no Al in the nanocube sample. From the EDX analysis, the sample composition matched approximately to Cu_3Se_2. Electron energy loss

spectroscopy (EELS, Figure 2, middle) further confirmed the absence of Al and the NC composition to be Cu_3Se_2. Single particle EELS (Figure 2, right) analyses showed NCs to have a Cu:Se ratio 3:2 with a composition distribution from particle to particle within the technique uncertainty. Single particle EELS elemental maps further showed that the NC composition was highly homogeneous within each particle.

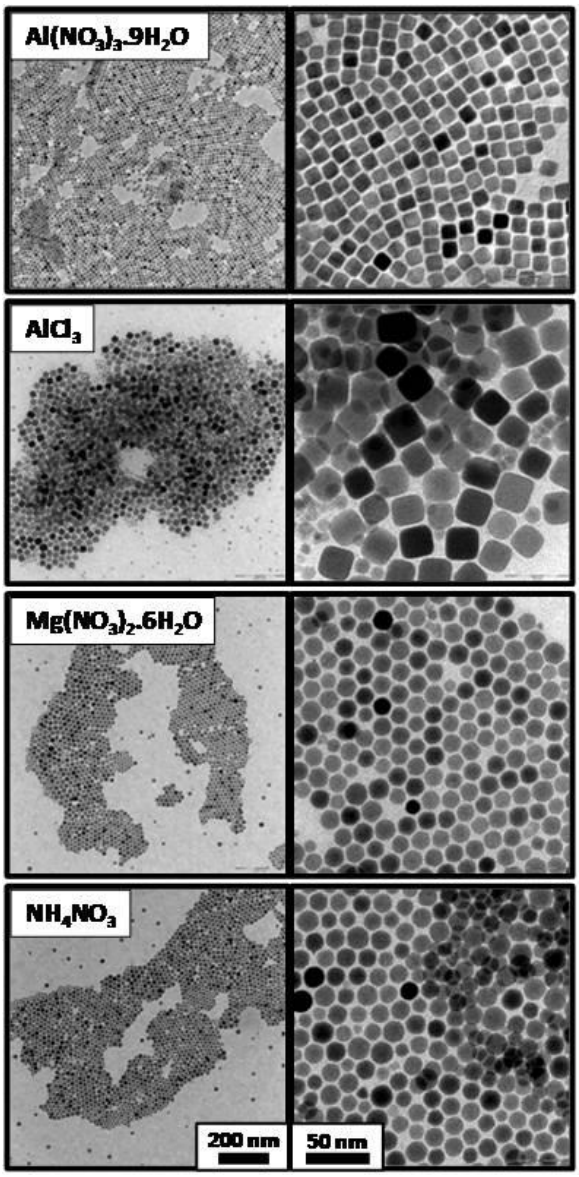

Figure 3. TEM micrograph of Cu_3Se_2 NCs obtained in the presence of HDA and different salts, as noted.

To determine the influence of NO_3^- and Al^{3+} ions on the Cu_3Se_2 NC growth, various control experiments were carried out. Figure 3 displays the TEM micrographs of the NCs obtained from the reaction of CuCl with the ODE-Se solution in the presence of HDA and different salts: $Al(NO_3)_3 \cdot 9H_2O$, $Mg(NO_3)_2 \cdot 6H_2O$, $AlCl_3$, NH_4NO_3. Cu_3Se_2 nanocubes were only obtained in the presence of $Al(NO_3)_3 \cdot 9H_2O$ and $AlCl_3$. The NCs obtained in the presence of $AlCl_3$ were sensibly worse in terms of size distribution than those obtained with $Al(NO_3)_3 \cdot 9H_2O$. The presence of HDA and the purity of the Se precursor solution were also demonstrated as essential to obtain nanoparticles with narrow size distributions. In particular, the Se source was very sensitive to preparation.[37] we are currently studying in detail the influence of the Se precursor preparation method on the morphology of the produced Cu_3Se_2 NCs.

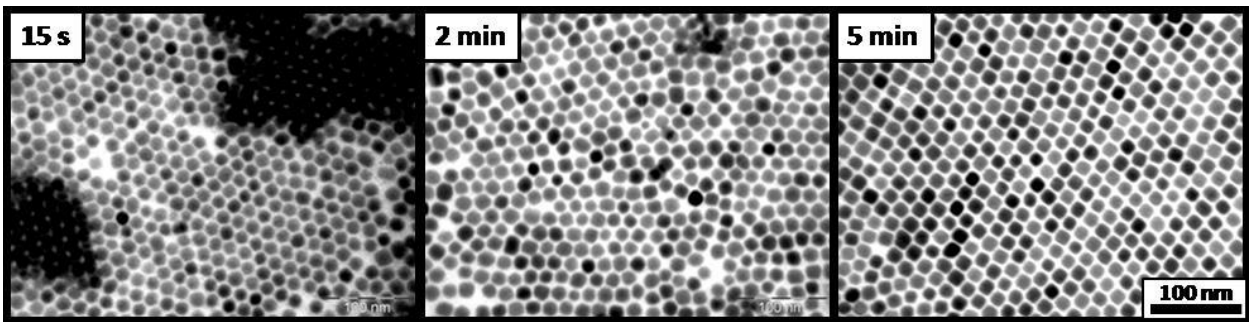

Figure 4. TEM micrographs of Cu_3Se_2 NCs obtained at successively higher reaction times.

Figure 4 shows the shape and size evolution of the obtained nanocrystals. For this study, several aliquots were extracted at different reaction times from a single batch. At the very early stage of the nanocrystals growth, the obtained initial Cu_3Se_2 NCs displayed similar sizes and narrow size distributions as in the final product but were characterized by quasi-spherical geometries.

However, NCs morphology evolved from quasi-spherical to cubic within a few minutes of reaction.

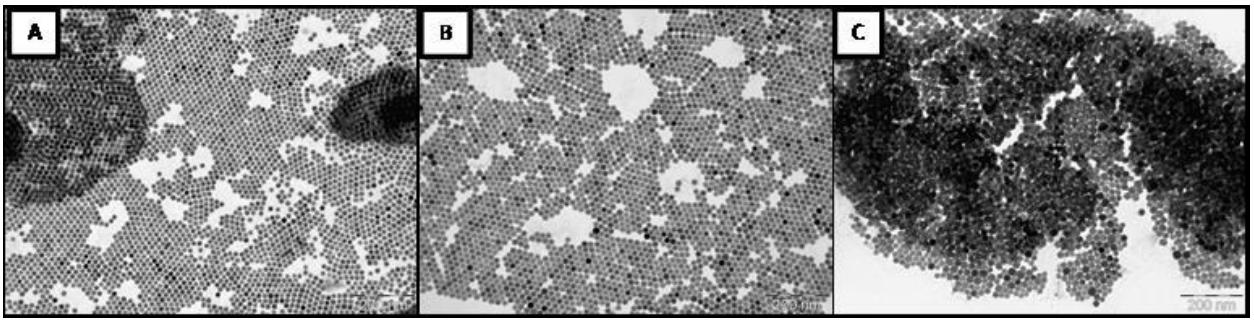

Figure 5. TEM images of copper selenide nanocubes obtained with different amount of $Al(NO_3)_3 \cdot 9H_2O$: (A) 0.1 mmol, (B) 0.3 mmol, and (C) 0.5 mmol).

As we stated in the previous part, the purity of Se precursor solution was essential to obtain nanoparticles with narrow size distributions, however, the Cu:Se nominal ratio, the reaction time and temperature were key parameters to control the shape of the copper selenide NPs as well. In addition, we investigated the influence of $Al(NO_3)_3 \cdot 9H_2O$ concentration on the final nanoparticle morphology. We followed the exact same procedure described in the Experimental section but just modifying the amount of $Al(NO_3)_3 \cdot 9H_2O$ introduced in the precursor solution. Particularly, we introduced the following amounts of $Al(NO_3)_3 \cdot 9H_2O$: 0.1, 0.3 and 0.5 mmol. Figure 5 displays TEM images of the nanoparticles obtained at each concentration. At it can be observed, all the nanoparticles displayed a cubic morphology and their size was quite similar. However, we could appreciate broader size distribution as the amount of $Al(NO_3)_3 \cdot 9H_2O$ was increased. Additionally, the nanoparticle purification became harder the higher the $Al(NO_3)_3 \cdot 9H_2O$ content. Based on these results, best nanocubes were obtained with 0.1 mmol of $Al(NO_3)_3 \cdot 9H_2O$.

The identification of copper selenide crystallographic phases is particularly difficult. Copper selenides exist in a wide variety of compositions and crystallographic systems, including orthorhombic, monoclinic, and cubic.[38-40] Figure 6 shows the X-ray diffraction (XRD) pattern of the nanoparticles prepared in the presence of HDA and different salts. X-ray diffraction analysis evidenced that the crystallographic structure of the Cu_3Se_2 NCs was not substantially modified by the presence of Al^{3+} ions in the precursor solution. From the NC composition obtained by EDX and EELS analysis, we anticipated the NCs to display the tetragonal umangite crystal structure. However, XRD patterns did not exactly match the umangite reference pattern (JCPDF: 01-071-0045). XRD patterns obtained did not exactly match any of the previously reported structures as shown in Figure 6.

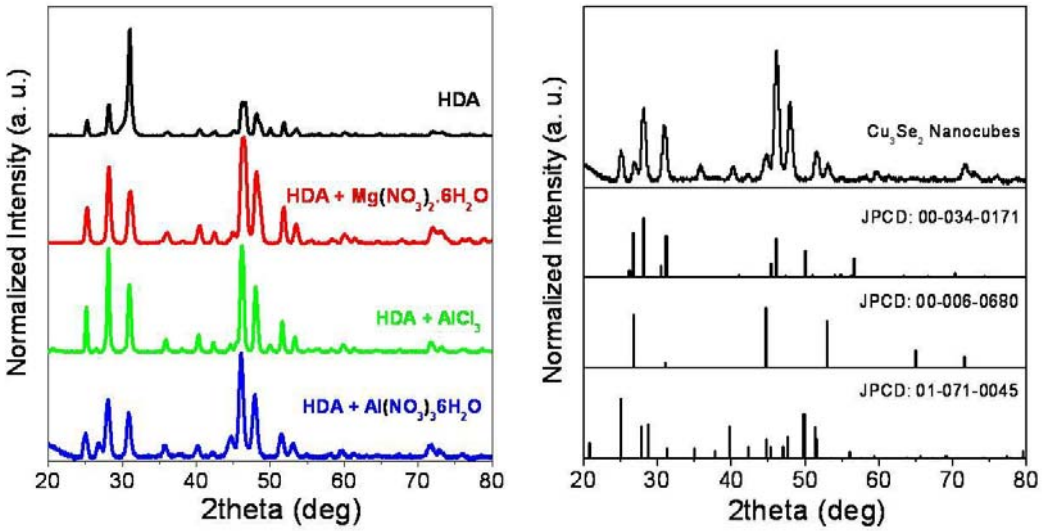

Figure 6. XRD patterns of the Cu_3Se_2 NCs obtained in the presence of HDA and different salts. As a reference the peak position of various copper selenide phases is also represented: klockmannite hexagonal CuSe JPCD: 00-034-0171; berzelianite cubic $Cu_{2-x}Se$ JPCD: 00-006-0680; umangite tetragonal Cu_3Se_2 JPCD: 01-071-0045.

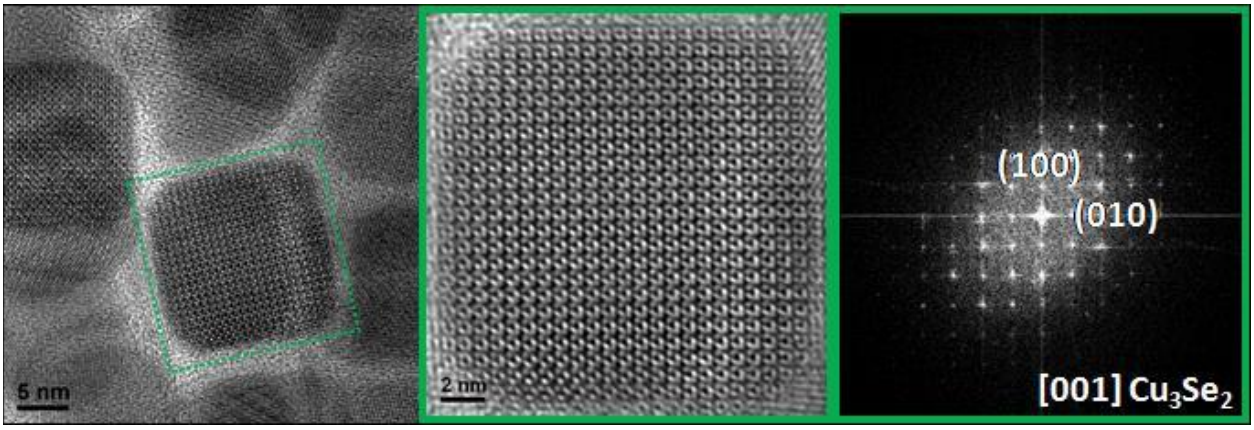

Figure 7. HRTEM micrographs and power spectrum analyses of a Cu_3Se_2 nanocube.

Figure 7 shows HRTEM micrographs and the corresponding power spectrum obtained by aligning the incident electron beam perpendicular to one of the square facets of a Cu_3Se_2 cube. The crystal structure obtained from HRTEM could be associated to the umangite tetragonal phase (S.G.: P-421m) with lattice parameters (a=b=7.2 Å; c=2a). However the cell parameters obtained from the power spectra (FFT) analyses were significantly different from those of the reported umangite phase. Otherwise, the crystal structure could be identified as orthorhombic with cell parameters a= 7.2 Å, b=7.3 Å and c= 14.4-14.5 Å. However, such crystal phase has not been previously reported and attending to the very small difference between a and b cell parameters it is more reasonably to associate the crystal structure to a quasi-tetragonal phase with c parameter being 2a (a=b; c=2a). Still, the formation of a tetragonal structure with double cell parameter along c suggests some ordering along the z-axis.

From the experimental results obtained, it is evident that Al^{3+} ions had a strong influence on the Cu_3Se_2 NC morphology. Because the cubic morphology was obtained after a few minutes of reaction time, after NCs reached an equilibrium with the monomer concentration in solution

(Figure 4), it is clear that nanocubes were formed during ripening due to a stability differential between the {111} and the {100} and {001} facets of the Cu_3Se_2 tetragonal-like structure. On the other hand, the chemical analysis of the final nanoparticles demonstrated that Al^{3+} ions did not incorporate to the Cu_3Se_2 crystal structure or surface facets in the used synthesis conditions. Adding both experimental observations together, we speculate that the role of Al^{3+} ions is more probably to promote the crystal growth in a specific direction instead of stabilizing a particular facet. We hypothesize that Al^{3+} ions block the binding of HDA to the {111} facets. Then, during the ripening regime, while {100} and {001} facets capped by HDA are stable towards the incorporation or dissolution of Cu and Se ions, {111} facets, possibly terminated by Al^{3+} ions with a fast dynamic salvation, are subject to a relatively fast exchange of Cu and Se ions with the solution. Thus {111} facets tend to disappear with the reaction time and {100} and {001} faceted nanocubes are formed. Again, the nanoparticle quality and morphology was very sensitive to the purity of the Se precursor solution. Thus ODE-Se must play an important role which remains to be elucidated in the global mechanism of Cu_3Se_2 NC size and shape control.

Copper selenides are usually p-type semiconductors with band gaps in the range 1.0-2.0 eV as we stated previously.[41-44] Their p-type character is associated to the presence of copper vacancies in the lattice, what makes their carrier concentration and transport properties strongly dependent on its composition. Copper selenides also display composition-dependent plasmonic light scattering in the NIR.[45-53] Their band-gap in the visible part of the spectrum and their plasmonic properties make copper selenides valuable materials in optoelectronic and plasmonic applications.

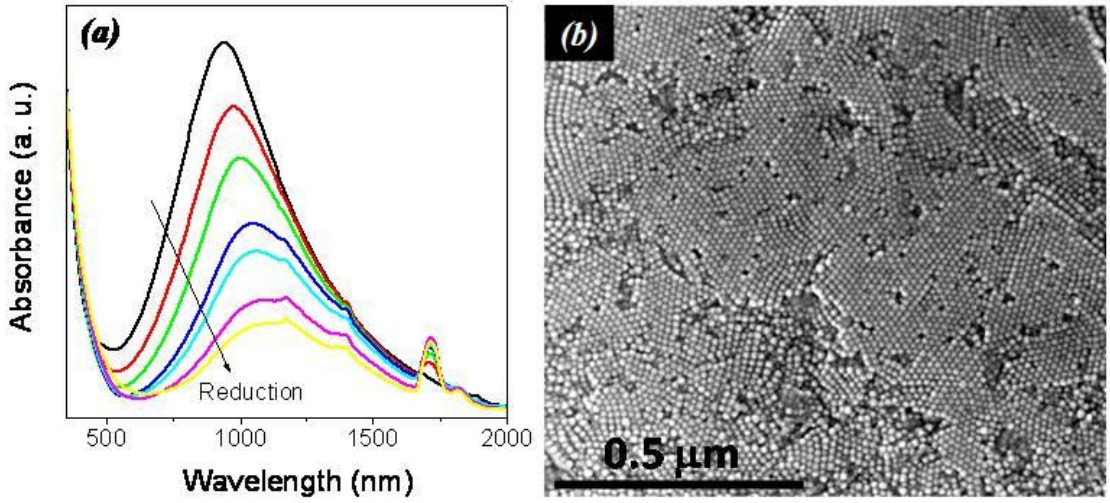

Figure 8. (a) Evolution of the absorption spectra of Cu_3Se_2 nanocubes in tetrachloroethylene when chemically reduced. Each step from the black toward the yellow spectrum corresponds to an addition of 50 µL of a 0.02 M $Li(C_2H_5)_3BH$ solution in tetrahydrofuran. (b) SEM micrograph of an assembly of Cu_3Se_2 nanocubes

Figure 8a shows the UV-vis spectra of colloidal Cu_3Se_2 nanocubes in tetrachloroethylene. A plasmon peak was clearly observed. The maximum of the peak blue shifted from 940 to 1110 nm when reducing the NCs with a $Li(C_2H_5)_3BH$ solution in tetrahydrofuran, probing its strong composition dependence.

As pointed out above, nanocubes have a convenient geometry for technological applications as they can maximize NC packing and produce highly compact films or bulk nanostructured materials (Figure 8b). Due to their advantageous morphology, we further used the Cu_3Se_2 nanocubes as a platform to produce other semiconductor nanocubes by cation exchange.

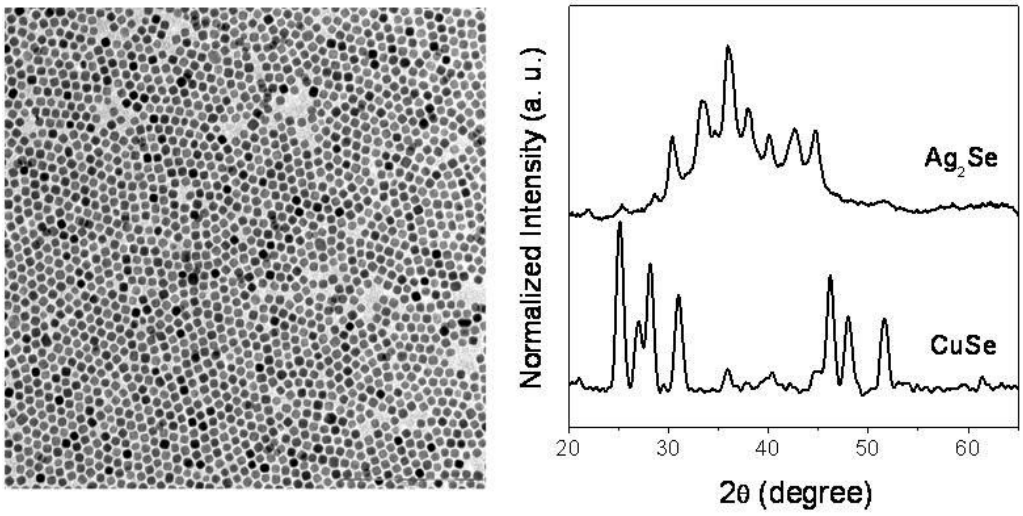

Figure 9. TEM micrograph and XRD pattern of the Ag_2Se nanocubes obtained by cation exchange from Cu_3Se_2 nanocubes. Scale bar corresponds to 200 nm.

Figure 9 shows a representative TEM micrograph and the corresponding XRD pattern of the Ag_2Se nanocubes obtained by cation exchange from Cu_3Se_2 NCs. Ag_2Se nanocubes were obtained from the dropwise addition at room temperature of 0.08 mL of a 0.2 mM $AgNO_3$ methanol solution to a toluene solution containing approximately 10 mg of Cu_3Se_2 NCs.[54-55]

4.3 Conclusions

In summary, we described how Al^{3+} ions catalyzed the formation of Cu_xSe nanocubes. The composition of the obtained copper selenide nanocubes was identified as Cu_3Se_2 and no aluminium was detected within the NC structure. Cu_3Se_2 nanocubes showed a strong composition-dependent plasmonic peak in the wavelength range between 900 and 1100 nm.

Cu_3Se_2 nanocubes were also proven as an excellent platform for the production of other selenide nanocubes.

4.4 References

(1) Catherine, J. M. *Science* **2002**, *298*, 2139-2141.

(2) Song, H.; Kim, F.; Connor, S.; Somorjai, G. A.; Yang, P. D. *J. Phys. Chem. B* **2005**, *109*, 188-193.

(3) Sherry, L. J.; Chang, S. H.; Schatz, G. C.; Duyue, R. P. V.; Wiley, B. J.; Xia, Y. N. *Nano. Lett.* **2005**, *5*, 2034-2038.

(4) Xiong, Y. J.; Wiley, B. J.; Chen, J. Y.; Li, Z. Y.; Yin, Y. D.; Xia, Y. N. *Angew. Chem. Int. Ed.* **2005**, *117*, 8127-8131.

(5) Zhang, J.; Kumbhar, A.; He, J. B.; Das, N. C.; Yang, K. K.; Wang, J. Q.; Wang, H.; Stokes, K. L.; Fang, J. Y. *J. Am. Chem. Soc.* **2008**, *130*, 15203-15209.

(6) Zhang, J.; Yang, H. Z.; Yang, K. K.; Fang, J. Y.; Zou, S. Z.; Luo, Z. P.; Wang, H.; Bae, I.; Jung, D. Y. *Adv. Funct. Mater.* **2010**, *20*, 3727-3733.

(7) Yin, Y.; Alivisatos, A. P. *Nature* **2005**, *437*, 664-670.

(8) Ibáñez, M.; Guardia, P.; Shavel, A.; Cadavid, D.; Arbiol, J.; Morante, J. R.; Cabot, A. *J. Phys. Chem. C.* **2011**, *115*, 7947-7955.

(9) Li, W. H.; Zamani, R.; Gil, P. R.; Pelaz, B.; Ibáñez, M.; Cadavid, D.; *J. Am. Chem. Soc.* **2013**, *135*, 7098-7101.

(10) Li, W. H.; Shavel, A.; Guzman, R.; Garcia, J. R.; Flox, C.; Fan, J. D.; Cadavid, D.; Ibáñez, M.; Arbiol, J.; Morante, J. R.; Cabot, A. *Chem. Commun.* **2011**, 47, 10332-10334.

(11) Ibáñez, M.; Zamani, R.; Li, W. H.; Shavel, A.; Arbiol, J.; Morante, J. R.; Cabot, A. *Cryst. Growth. Des.* **2012**, *12*, 1085-1090.

(12) Singh, A.; Geaney, H.; Laffir, F. R.; Ryan, K. M. *J. Am. Chem. Soc.* **2012, *134*,** 2910-2913**.**

(13) Shavel, A.; Arbiol, J.; Cabot, A. *J. Am. Chem. Soc.* **2010**, *132*, 4514-4515.

(14) Zhang, J.; Fang, J. Y. *J. Am. Chem. Soc.* **2009**, *131*, 18543-18547.

(15) Zhang, J.; Yang, H. Z.; Fang, J. Y.; Zou, S. H. *Nano. Lett.* **2010**, *10*, 638-644.

(16) Lim, S. I.; Ojea-Jiménez, I.; Varon, M.; Casals, E.; Arbiol, J.; Puntes, V. *Nano. Lett.* **2010**, *10*, 964-973.

(17) Chen, J. Y.; Lim, B.; Lee, E. P.; Xia, Y. N. *Nano. Today.* **2009**, *4*, 81-95.

(18) Loukrakpam, R.; Chang, P.; Luo, J.; Fang, B.; Mott, D.; Bae, I. T.; Naslund, R.; Engelhard, M. H.; Zhong, C. J. *Chem. Commun.* **2010**, *46*, 7184-7186.

(19) Chen, J.; Herricks, T.; Xia, Y. N. *Angew. Chem. Int. Ed.* **2005**, *44*, 2589-2592.

(20) Chen, J.; Herricks, T.; Geissler, M.; Xia, Y. N. *J. Am. Chem. Soc.* **2004**, *126*, 10854-10855.

(21) Lim, B.; Lu, X.; Jiang, M.; Camargo, P. H. C.; Cho, E. C.; Lee, E. P.; Xia, Y. N. *Nano. Lett.* **2008**, *8*, 4043-4047.

(22) Grass, M. E.; Yue, Y.; Habas, S. E.; Rioux, R. M.; Teall, C. I.; Yang, P.; Somorjai, G. A. *J. Phys. Chem. C* **2008**, *112*, 4797-4804.

(23) Teng, X.; Yang, H. *Nano. Lett.* **2005**, *5*, 885-891.

(24) Huynh, W. U.; Dittmer, J. J.; Alivisatos, A. P. *Science,* **2002**, *295*, 2425-2427.

(25) Talapin, D. V.; Murray, C. B. *Science,* **2005**, *310*, 86-89.

(26) Dong, A.; Tang, R.; Buhro, W. E. *J. Am. Chem. Soc.* **2007***,129*, 12254-12262.

(27) Sun, J.; Wang, L. W.; Buhro, W. E. *J. Am. Chem. Soc.* **2008**, *130*, 7997-8005.

(28) Talapin, D. V.; Lee, J. S.; Kovalenko, M. V.; Shevchenko, E. V. *Chem. Rev.* **2010**, *110*, 389-458.

(29) Chen, H.; Zou, R.; Wang, N.; Chen, H.; Zhang, Z.; Sun, Y.; Yu, L.; Tian, Q.; Chen, Z.; Hu, J. *J. Mater. Chem.* **2011**, *21*, 3053-3059.

(30) Choi, J.; Kang, N.; Yang, H. Y.; Kim, H. J.; Son, S. U. *Chem. Mater*. **2010**, *22*, 3586-3588.

(31) Zhang, S. Y.; Fang, C. X.; Tian, Y. P.; Zhu, K. R.; Jin, B. K.; Shen, Y. H.; Yang, J. X. *Cryst. Growth. Des.* **2006**, *6*, 2809-2813.

(32) Xu, J.; Zhang, W.; Yang, Z.; Ding, S.; Zeng, C.; Chen, L.; Wang, Q.; Yang, S. *Adv. Funct. Mater.***2009**, *19*, 1759-1766.

(33) Liu, H.; Shi, X.; Xu, F.; Zhang, L.; Zhang, W.; Chen, L.; Li, Q.; Uher, C.; Day, T.; Snyder, G. J. Nat. Mater. **2012**, *11*, 422-425.

(34) GarcmHa, V. M.; Nair, P. K.; Nair, M. T. S. *J. Cryst. Growth.* **1999**, *203*, 113-124.

(35) Shen, H.; Wang, H.; Yuan, H.; Ma L.; Li, L. *Cryst. Eng. Comm*. **2012**, *14*, 555-560.

(36) Yu, R.; Ren, T.; Sun, K.; Feng, Z.; Li, G.; Li, C. *J. Phys. Chem. C*, **2009**, *113*,10833-10837.

(37) Bullen, C.; van Embden, J.; Jasieniak, J.; Cosgriff, J. E.; Mulder, R. J.; Rizzardo, E.; Gu, M.; Raston, C. L. *Chem. Mater.* **2010**, *22*, 4135-4143.

(38) Haram, S. K.; Santhanam, K. S. V.; Numann-Spallar, M.; Levy-Clement, C. *Mater. Res. Soc. Bull.* **1992**, *27*, 1185-1191.

(39) Haram, S. K.; Santhanam, K. S. V. *Thin. Solid. Films.* **1994**, *238*, 21-26.

(40) Heyding, R. D.; Murray, R. M. *Can. J. Chem.* **1976**, *54*, 841-848.

(41) Chen, W. S.; Stewart, J. M.; Mickelson, R. A. *Appl. Phys. Lett.* **1985**, *46*, 1095-1097.

(42) Hermann, A. M.; Fabick, L. *J. Cryst. Growth* **1983**, *61*, 658-664.

(43) Okimura, H.; Matsumae, T.; Makabe, R. *Thin. Solid. Films.* **1980**, *71*, 53-59.

(44) Riha, S. C.; Johnson, D. C.; Prieto, A. L. *J. Am. Chem. Soc.* **2011**, *133*, 1383-1390.

(45) Deka, S.; Genovese, A.; Zhang, Y.; Miszta, K.; Bertoni, G.; Krahne, R.; Giannini, C.; Manna, L.*; J. Am. Chem. Soc.* **2010**, *132*, 8912-8914.

(46) Dorfs, D.; Hartling, T.; Miszta, K.; Bigall, N. C.; Kim, M. R.; Genovese, A.; Falqui, A.; Povia, M.; Manna, L. *J. Am. Chem. Soc.* **2011**, *133*, 11175-11180.

(47) Gurin, V. S.; Prokopenko, V. B.; Alexeenko, A. A.; Wang, S.; Prokoshin, P. V. *Mater. Sci. Eng. C* **2001**, *15*, 93-95.

(48) Machado, K. D.; Lima, J. C.; Grandi, T. A.; Campos, C. E. M.; Maurmann, C. E.; Gasperini, A. A. M.; Souza, S. M.; Pimenta, A. F. *Acta. Crystallogr. Sect. B* **2004**, *60*, 282-286;

(49) Jagminas, A.; Juskenas, R.; Gailiute, I.; Statkute, G.; Tomasiunas, R. *J. Cryst. Growth* **2006**, *294*, 343-348.

(50) Seoudi, R.; Shabaka, A. A.; Elokr, M. M.; Sobhi, A. *Mater. Lett.* **2007**, *61*, 3451-3455.

(51) Hessel, C. M.; Pattani, V. P.; Rasch, M.; Panthani, M. G.; Koo, B.; Tunnell, J. W.; Korgel, B. A. *Nano. Lett.* **2011**, *11*, 2560-2566.

(52) Luther, J. M.; Jain, P. K.; Ewers, T.; Alivisatos, P. A. *Nat. Mater.* **2011**, *10*, 361-366.

(53) Ibáñez, M.; Cadavid, D.; Zamani, R.; García-Castelló, N.; Izquierdo-Roca, V.; Li, W.; Fairbrother, A.; Prades, J. D.; Shavel, A.; Arbiol, J.; Pérez-Rodríguez, A.; Morante, J. R.; Cabot, A. *Chem. Mater.* **2012**, 24, 562-570.

(54) Son, D. H.; Hughes, S. M.; Yin, Y. D.; Alivisatos, A. P. *Science* **2004**, *306*, 1009-1012.

(55) Pietryga, J. M.; Werder, D. J.; Williams, D. J.; Casson, J. L.; Schaller, R. D.; Klimov, V. I.; Hollingsworth, J. A. *J. Am. Chem. Soc.* **2008**, *130*, 4879-4885.

Chapter 5

Shape-Controlled Synthesis of CuTe Nanocrystals and Their Plasmonic Properties

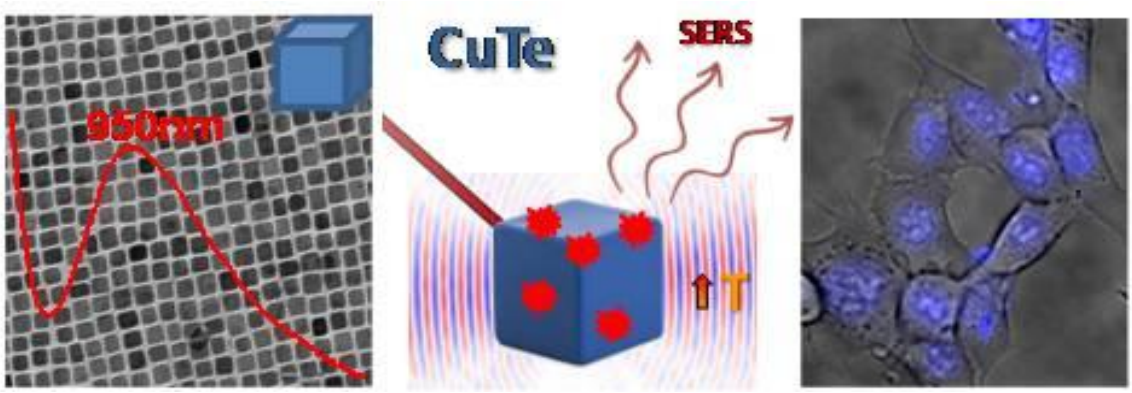

5.1 Introduction

Copper-based chalcogenides are used in a wide range of applications, from thermoelectrics to batteries, including photonics, photovoltaics, and photothermal therapy.[1-6] They are usually p-type semiconductors, due to the presence of copper vacancies. Copper vacancies not only determine charge transport properties but also provide copper chalcogenides with a particularly attractive property: a composition-dependent localized surface plasmon resonance (LSPR) in the near-infrared (NIR).[7-8] In particular, copper telluride is characterized by a large thermal power, a direct band gap between 1.1 eV and 1.5 eV and superionic conductivity. Copper telluride can exist in a wide range of compositions and phases, which allows tuning its properties by just adjusting the Cu/Te ratio. These properties provide it with both high fundamental interest and

technological potential. However, in spite of its relevance, little is known about its properties at the nanoscale, e.g. plasmonic, and a synthetic route to produce uniform copper telluride nanoparticles (NPs) is yet to be reported. While a variety of procedures to prepare sulfide and selenide NPs with excellent uniformity are available,[7-10] one main constraint to produce telluride NPs and particularly copper telluride is the reduced number of tellurium sources available, which narrows the range of accessible reaction conditions to direct telluride NPs nucleation and growth. In the present work, the potential of lithium bis(trimethylsilyl)amide to control the growth of copper telluride NPs is demonstrated and a simple synthetic route to produce highly uniform copper telluride nanocubes, nanoplates, and nanorods is detailed as well. We further demonstrate how copper telluride NPs provide a new and unique optical platform for the design of plasmonic sensors of a wide family of molecules that cannot be conventionally analyzed with surface-enhanced Raman scattering (SERS).[11-12] Furthermore, we show preliminary results on the use of copper telluride NPs for photothermal destruction of cells.

5.2 Results and discussion

5.2.1 CuTe shape and size control

Copper telluride NPs were prepared by reacting copper (I) chloride with trioctylphosphine telluride (TOPTe) in the presence of trioctylphosphine (TOP), trioctylphosphine oxide (TOPO), lithium bis(trimethylsilyl)amide $LiN(SiMe_3)_2$, and distilled oleylamine (OLA). The reported synthetic procedures by using OLA, TOPO, and TOP system to synthesize nanocrystals have been well investigated to produce a wide range of chalcogenide nanocrystals with well-controlled shape and size.[13-15] However, all of them did not allow the production of copper

telluride nanocrystals by just changing the S or Se precursor by Te. In this part, the highly uniform CuTe nanocubes, nanoplates and nanorods in the presence of $LiN(SiMe_3)_2$. In a typical synthesis, 0.25 mmol of CuCl was mixed with 1 mmol of TOPO and 6 mL of OLA in a 25 mL three-neck flask. The mixture was heated under vacuum to 100 °C to obtain a clear blue solution, and kept at this temperature for 30 min to remove low boiling point impurities. Then temperature was raised to 160 °C, and 0.125 mL of TOP was added. In parallel, a tellurium precursor solution was prepared inside the glovebox by mixing 0.125 mL of a 2 M TOPTe solution with 0.5 mL of a 0.5 M $LiN(SiMe_3)_2$ solution in dried octadecene (ODE). The tellurium solution was rapidly injected to the copper solution maintained at 160 °C. Upon injection, the solution color immediately changed to deep green, and temperature dropped to 152 °C. Just after injection, temperature was set to 220 °C and NPs were allowed to grow for 30 min. During cooling, when temperature reached 70 °C, 2 mL of oleic acid were added to replace the weakly bound OLA molecules.

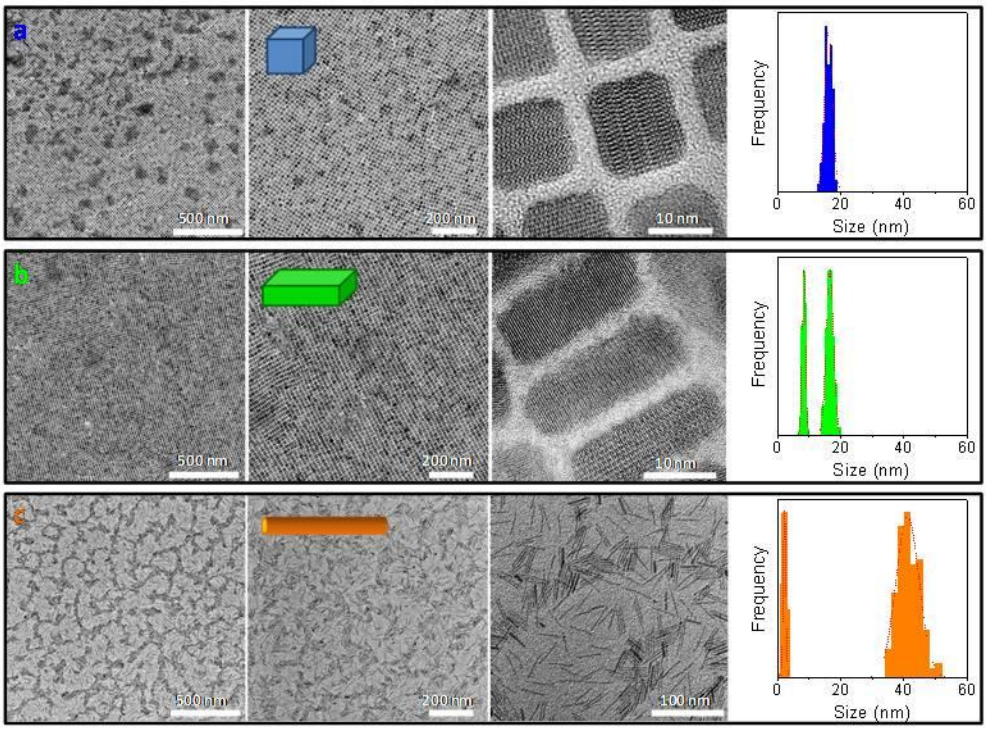

Figure 1. TEM micrograph and size distribution histograms of CuTe NPs: (a) nanocubes; (b) nanoplates; (c) nanorods.

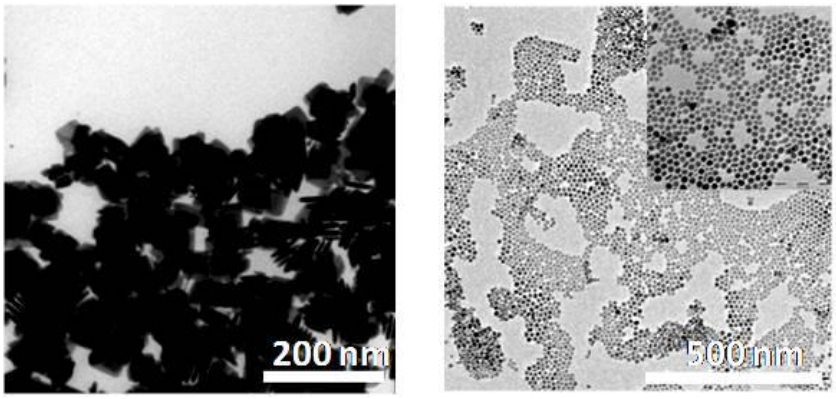

Figure 2. TEM micrographs showing the nanoparticles obtained without $LiN(SiMe_3)_2$ (left) and using $CuN(SiMe_3)_2$ as Cu precursor in the absence of Lithium (right).

Figure 1a shows representative transmission electron microscopy (TEM) and high resolution TEM (HRTEM) micrographs of the copper telluride NPs obtained by the procedure described

above. NPs displayed a cubic geometry and very narrow size distributions (< 5 %), which facilitated their self-assembly in cubic superlattices extending several microns.

The presence of $LiN(SiMe_3)_2$ molecules was found critical to produce cubic NPs with narrow size distributions. When attempting to produce copper telluride NPs without this compound, large rectangular plates with very broad size distributions were obtained (Figure 2, left). This experimental result clearly demonstrates that $LiN(SiMe_3)_2$ plays a very important role on the size and shape control of CuTe NPs and it should be noted that without $LiN(SiMe_3)_2$, the nucleation event was not as abrupt as in the presence of $LiN(SiMe_3)_2$, thus this compound facilitates the CuTe nucleation. One possible mechanism would be the formation of $CuN(SiMe_3)_2$ from the reaction of copper with $LiN(SiMe_3)_2$. This copper complex would then act as the precursor compound reacting with TOPTe. To determine if this was the CuTe formation mechanism and to further assess the Lithium role in the size and shape control, $CuN(SiMe_3)_2$ was prepared inside our glovebox and used as precursor for the Li-free synthesis of CuTe nanoparticles. The reaction of $CuN(SiMe_3)_2$ with TOPTe resulted in quasi-spherical NPs (Figure 2, right). This control experiment proved that $LiN(SiMe_3)_2$ actually have an important role in the control of the CuTe NP shape. Following recent findings on the mechanism of formation of metal NPs in the presence of $LiN(SiMe_3)_2$ and OLA,[16] we speculate $LiN(SiMe_3)_2$ activates the formation of a Cu-oleylamido complex, which is the actual species reacting with TOPTe to form the copper telluride NPs. Besides, the Cu-oleyamido complexes and/or lithium oleylamine may stabilize the NP surface during growth.

The Cu:Te nominal ratio, the reaction time and temperature and the concentration of TOP were key parameters to control the size and shape of the copper telluride NPs obtained. By tuning the Cu:Te ratio, we could control the size of the nanocubes in the range between 10 and

20 nm (Figure 3). Nanocubes size increased with the Cu:Te ratio. We hypothesize that TOPTe concentration controls NP nucleation. When increasing the concentration of TOPTe a higher nucleation rate is initially obtained, reducing the total amount of precursor for posterior NP growth. Thus smaller NPs are finally obtained.

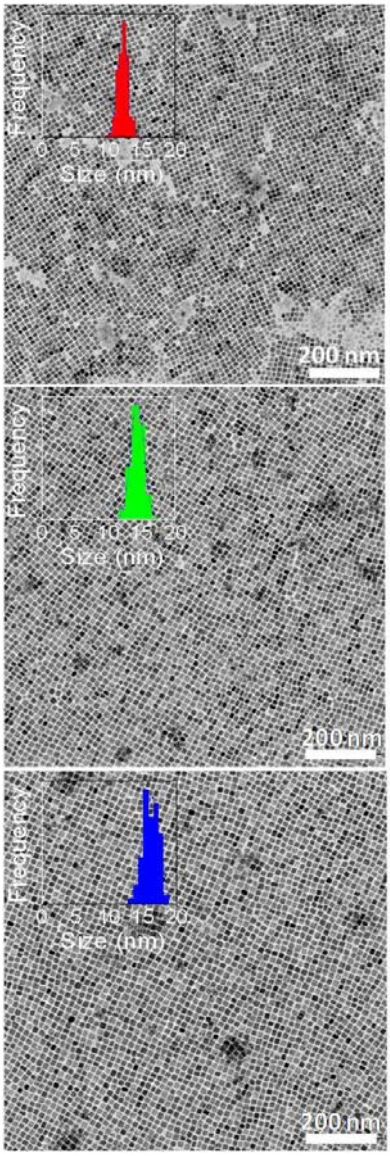

Figure 3. TEM micrographs of copper telluride nanocubes with different average size obtained from different Cu:Te ratios (from up to bottom, the precursors of Cu:Te ratio is 1:2, 3:4 and 1:1, respectively).

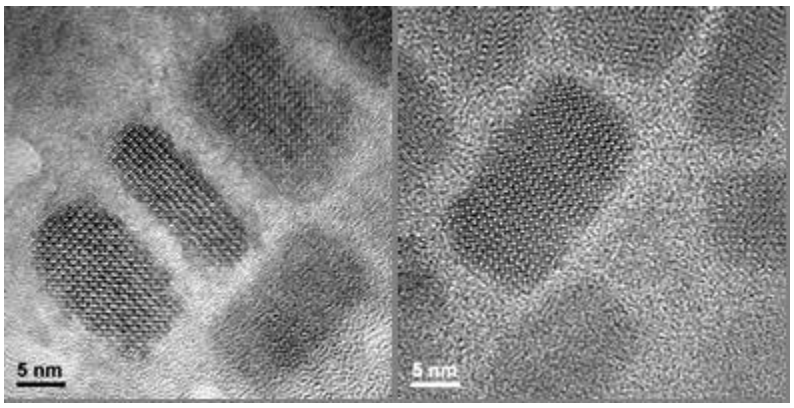

Figure 4. HRTEM micrographs of copper telluride nanoplates.

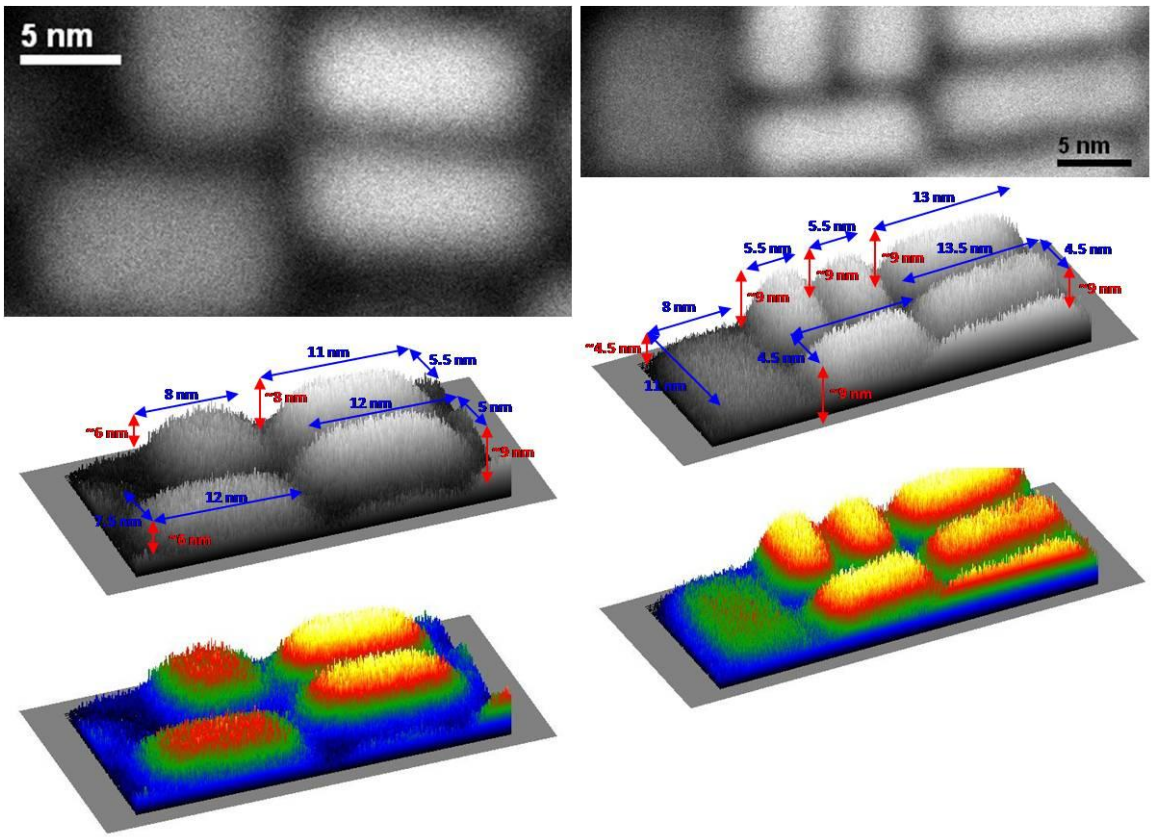

Figure 5. HAADF images and 3D profiles of CuTe nanoplates.

When decreasing the reaction temperature to 190 °C and the growth time to 15 min, highly homogeneous copper telluride nanoplates were produced (Figures 1b). To verify that those are

nanoplates instead of thick nanorods or nanodisks, more TEM measurements were carried out as shown in the Figure 4, Figure 5 and Figure 6. The left HRTEM image in Figure 4 shows three nanoplates aligned by their length. The one in the middle is lying on its side, meaning that the dimensions we see are the thickness (6 nm) and the length (18 nm), while the other two are lying on the largest surface, meaning we can see their widths (10 nm) and lengths (16 and 17 nm). The right HRTEM image in Figure 4 also shows few CuTe nanoplates. The nanoplate in the middle is lying on its widest side (12 x 21 nm), and the top-right nanoplate in the same image is lying on its side and has a thickness of around 7 nm. Notice that the surface gets slightly rough under the TEM e beam.

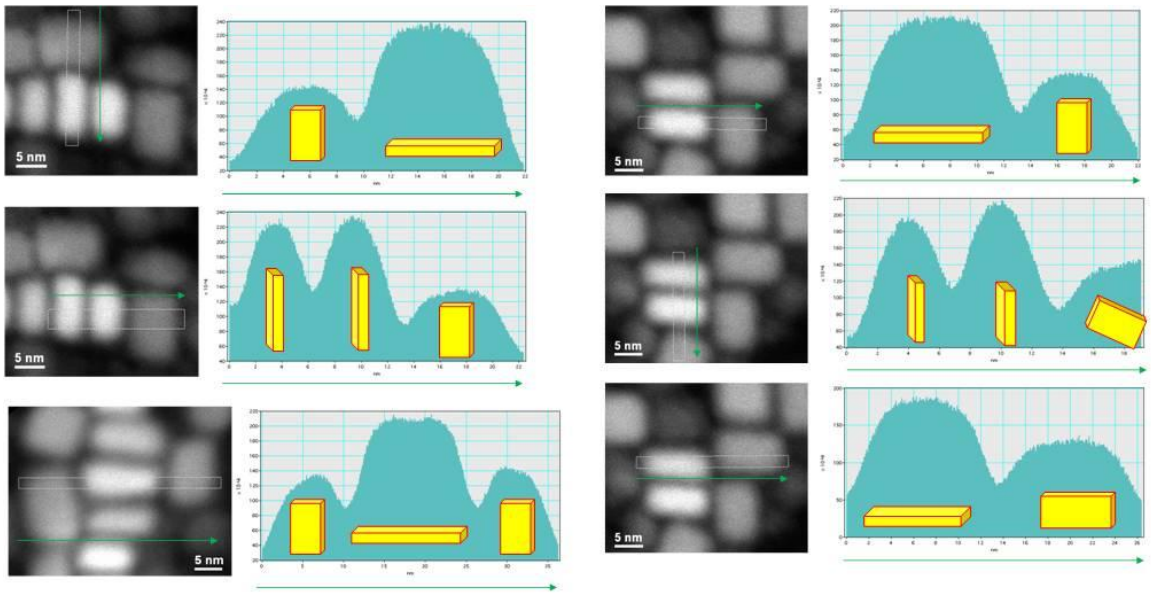

Figure 6. HAADF images and intensity profiles of CuTe nanoplates.

In the High Angle Annular Dark Field (HAADF) images the brightness is proportional to the material composition and also to the sample thickness (linear density). As all nanoplates have the same chemical composition, the intensity profiles of the HAADF images are related to their

thickness of the plates we see. In the images below we show the HAADF 3D (Figure 5) and 1D (Figure 6) intensity profiles of the CuTe NPs oriented in different directions, some of them are lying on the thin side, and others are lying on the widest side. The bimodal distribution of thicknesses obtained probes that the geometry of the CuTe nanostructures obtained is the plate.

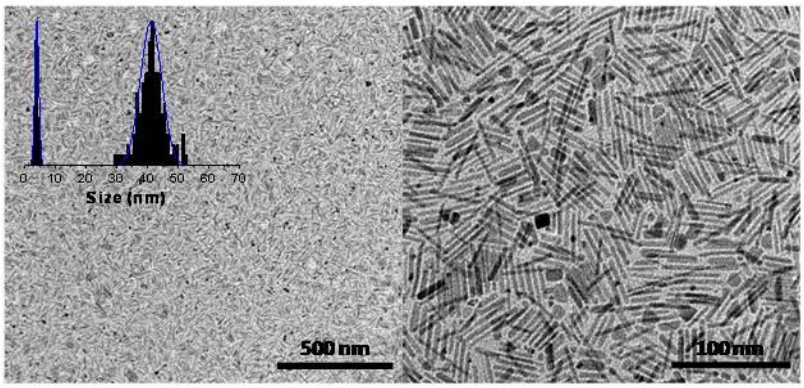

Figure 7. TEM micrographs of copper telluride nanorods obtained as detailed in Figure 1c but after 5 min reaction time.

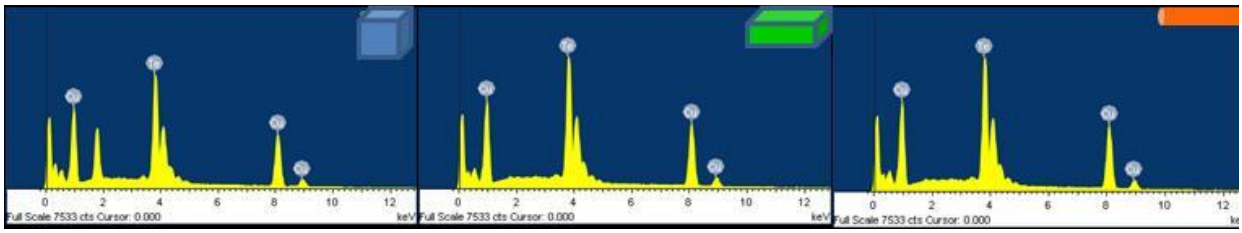

Figure 8. EDX spectra of copper telluride nanoparticles. The ratio Cu:Te is determined to be close to 1:1 for nanocubes (left), nanoplated (middle) and nanorods (right).

On the other hand, an increase of the TOP concentration resulted in the formation of nanorods. When adding 0.75 mL of TOP instead of 0.125 mL and setting the growth temperature to 190 °C and the growth time to 2 min, thin nanorods were obtained (Figure 1c). By increasing the reaction time thicker nanorods were produced but its size distribution worsened (Figure 7).

Energy-dispersive x-ray spectroscopy (EDX, Figure 8) and electron energy loss spectroscopy (EELS, Figure 9) analysis showed the NPs to have a Cu:Te atomic ratio close to 1:1. Further single particle analysis demonstrated the homogeneous distribution of the two elements within each particle and a very uniform composition from particle to particle (Figure 10).

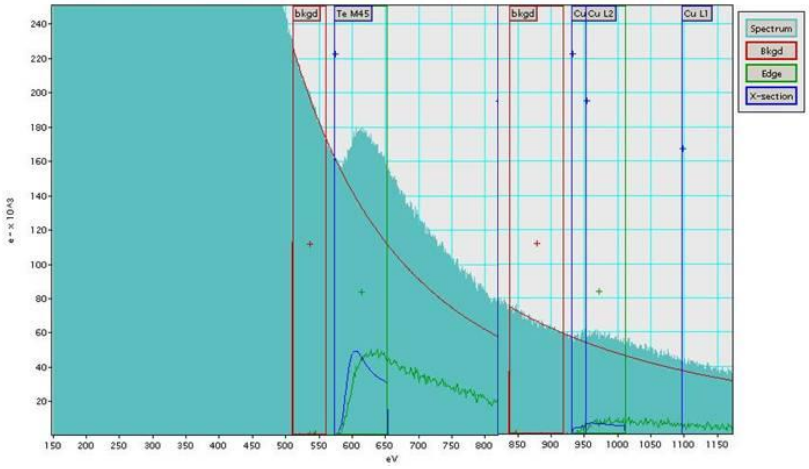

Figure 9. Raw EELS spectrum of copper telluride nanoparticles and the quantification on parent-spectrum image shows the nanoparticle composition to be 52 % of Cu and 48 % of Te, with a 4 % error, taking into account the technique resolution and statistical variations from sample to sample. Thus the ratio Cu:Te is very close to 1:1, which is consistent with the results obtained from an extensive EDX analysis of numerous samples. In the EELS analysis, the width of the signal windows was 80 eV in the case of both elements (in the case of Te starting from 572 eV, and in the case of Cu starting from 931 eV).

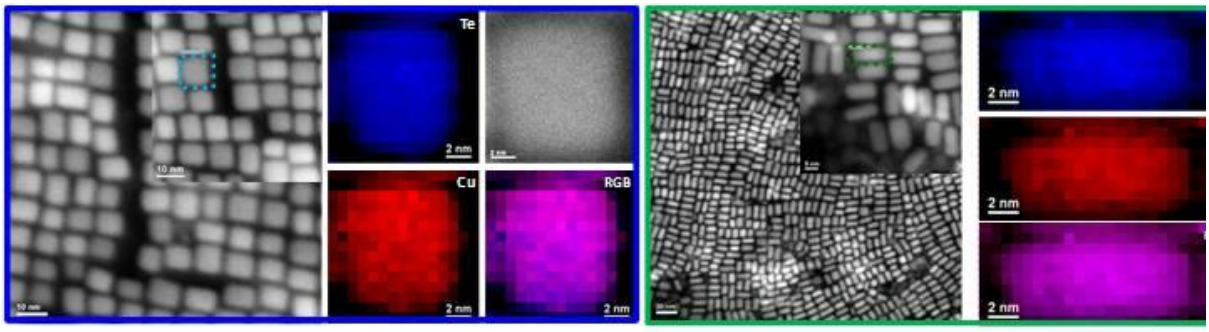

Figure 10. Z-contrast scanning TEM images and Te and Cu EELS elemental mapping images of copper telluride nanocubes and nanoplates.

The crystal phase identification in copper chalcogenides and more generally in transition metal chalcogenides is a challenging task. The partially filled d-shell in transition metals allows them to adopt multiple oxidation states, what results in compounds with a large composition and structural diversity. Copper tellurides exist as orthorhombic CuTe, hexagonal Cu_2Te, Cu_3Te_4, Cu_7Te_5, etc. and also as non-stoichiometric $Cu_{2-x}Te$ phases.[17-19] X-ray diffraction (XRD) analyses demonstrated CuTe nanorods, nanocubes and nanoplates to have the same crystal structure, but it did not allow to unequivocally determine it as the patterns measured did not exactly match with any of the copper telluride phases in the literature (Figure 11).

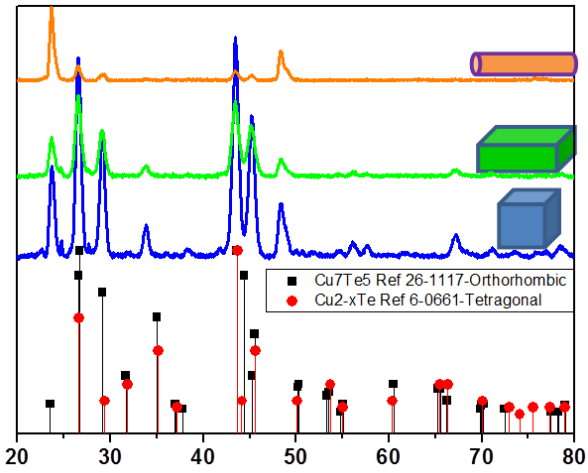

Figure 11. XRD patterns of copper telluride nanocubes, nanoplates and nanorods.

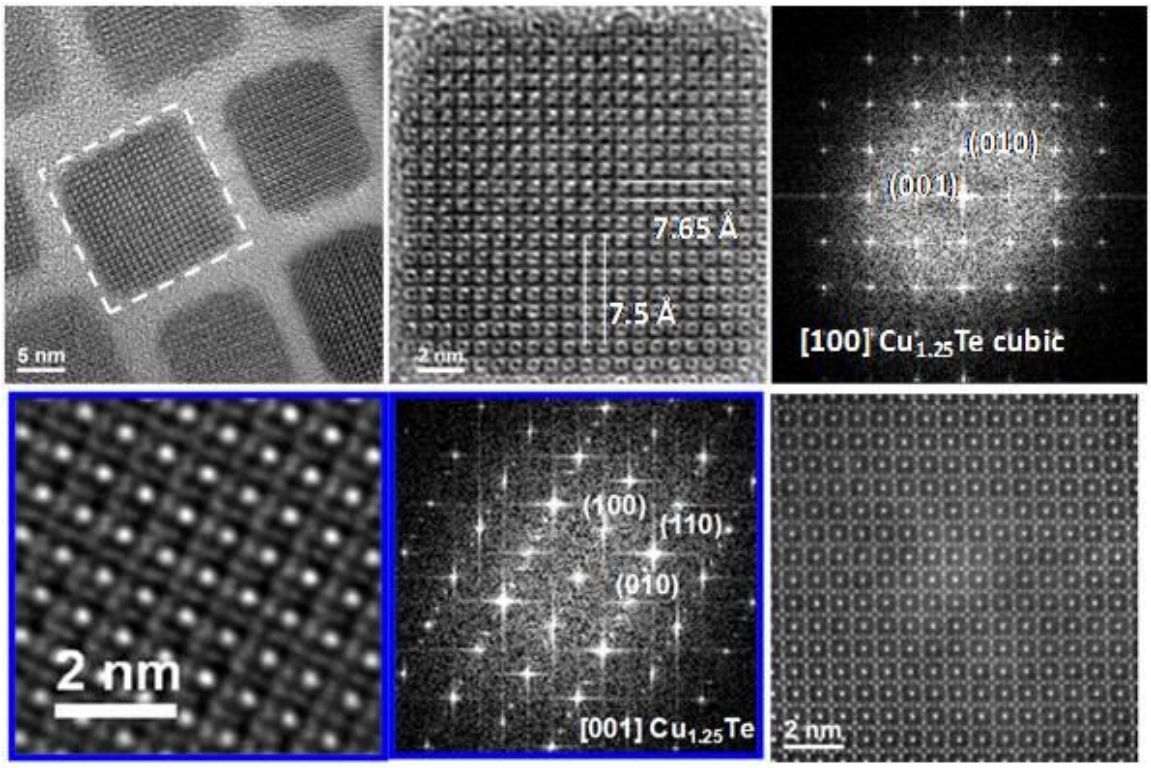

Figure 12. HRTEMs and power spectra of copper telluride nanocubes (top 2 lines), annular dark-field scanning TEM image (second line) and additional HRTEM micrographs of CuTe nanoparticles. The crystal structure resembles that of a tetragonal $Cu_{1.25}Te$ phase with cell parameter a=b=7.50 ± 0.05 Å and c=7.65 ± 0.05 Å. Periodic spots appearing between the main spots indicate the presence of an ordered superstructure.

Figures 1 and 12 show HRTEM micrographs of the CuTe nanocubes and nanoplates obtained. No reliable HRTEM micrograph could be obtained from nanorods due to electron beam-induced structural modifications. From the HRTEM analysis, we associate the NPs crystal phase with a tetragonal $Cu_{1.25}Te$ structure having cell parameters a=b=7.50 ± 0.05 Å and c=7.65 ± 0.05 Å. CuTe NPS further display a superstructure with periodicity of three unit cells, which could be originated from an internal ordering of copper vacancies (Figure 12).[20]

5.2.2 Optical properties of CuTe nanocrystals

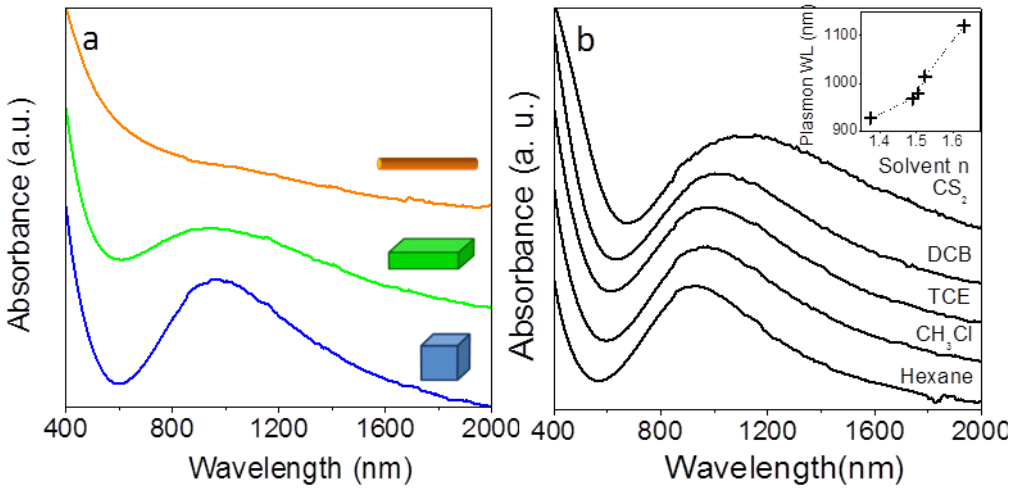

Figure 13. (a) UV-vis spectra of copper telluride nanocubes, nanoplates and nanorods; (b) Extinction spectra of copper telluride nanocubes in hexane, chloroform (CH_3Cl), tetrachloroethylene(TCE), dichlorobenzene (DCB), and carbondisulfide (CS_2) with the solvent refractive indices 1.38, 1.45, 1.50, 1.54 and 1.63, respectively. Inset displays the peak position as a function of the solvent which shows Red-shift of NIR LSPR with increasing refractive index of the solvent.

Figure 13a shows the UV-vis spectra of colloidal CuTe NPs with different geometries. A strong absorption band cantered at 950 nm and associated to a localized surface plasmon resonance (LSPR)[7] is clearly observed in the spectra obtained from CuTe nanocubes. This band had a weaker intensity in CuTe nanoplates and nearly disappeared from the UV-vis spectra of thin CuTe nanorods, probably because the small transversal dimension of thin nanorods does not support a detectable plasmon.

The position of the LSPR band in the copper chalcogenide was actively tuned by changing the dielectric environment of the NCs. In refractive index sensing experiments with copper telluride nanocubes with well-defined NIR LSPR, the particles were re-dispersed in organic solvents of

different refractive indexes, namely hexane (n=1.38), chloroform (CH_3Cl, n=1.45), tetrachloroethylene (TCE, n=1.50), dichlorobenzene (DCB, n=1.54), and carbon disulfide (CS_2, n=1.63). Note that due to the certain degree of sensitivity of our NCs to oxygen, the fresh sample was prepared and re-dispersed in the different solvents before the moment to measure. The results summarized in Figure 13b demonstrate that both LSPR red-shift with increasing solvent refractive index in agreement with the behavior of LSPR in metal nanoparticles[21] and with recent work from Alivisatos and co-workers.[22] The insert in Figure 13b summarizes the LSPR peak position of the same copper telluride nanocubes plotted versus the refractive index of the solvent clearly showing a red-shift in the maximum of the NIR plasmon band with increasing refractive index of the solvent.

5.2.3 Application of CuTe nanocubes and nanoplates in SERS measurement

Plasmonic NPs find applications in a broad range of fields, from optoelectronics to biomedical. A particularly interesting application is the use of their extremely high near electric fields to increase the signals of molecules close to their surfaces. SERS spectroscopy is one of the most powerful techniques for ultra-detection. Unfortunately the direct applicability of this technique has been so far restricted to molecular families carrying functional groups ($-NH_2$ or -SH) with affinity for gold or silver, the most common plasmonic nanostructures. The analysis of other compounds requires of surface functionalization with trapping species which many times result difficult and expensive to obtain.[5] thus the preparation of plasmonic materials with different surface chemistry permits the direct identification of chemical families which present oxygen

based functional groups and that are ubiquitous in the environment and biological media as pollutants, metabolites or disease markers.

On the other hand small gold and silver NPs present LSPRs at the visible, although it is possible to tune the size and shape in gold to shift these bands to the IR such as in the case of the nanostars or nanoshells. This usually results in an increase of the particle size, limiting the applicability of these particles in living organism. Notably, the natural excitation of CuTe LSPRs at the NIR paves the way for the improvement of bio-applications either in therapy or sensing. CuTe NPs were analyzed without any analyte to check for surfactant spurious bands. Notably, at the normal experimental SERS conditions TOPO and OLA did not yield any appreciable signal, consistent with the low SERS cross-sections of aliphatic species (Figure 14).

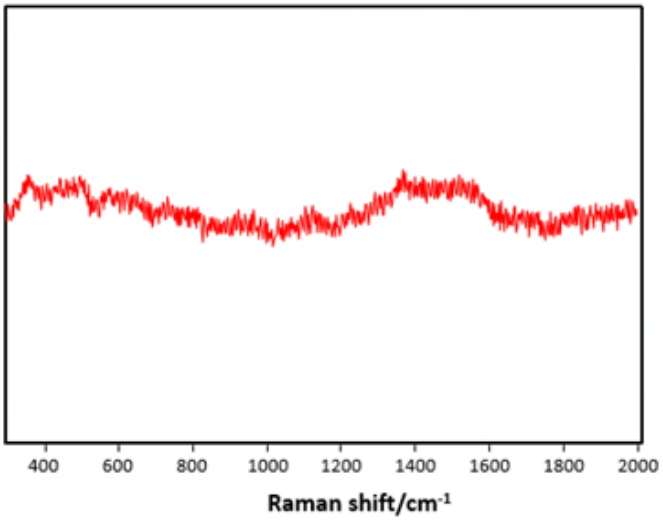

Figure 14. SERS spectra of the colloidal suspensions of CuTe without any analyte.

To probe the efficiency of the prepared CuTe particles as SERS sensors, two analytes were selected, nile blue, which carries an ionized amino group, and nile red, a highly hydrophobic

molecule that has a keto-oxygen available for surface reaction. To compare the results of CuTe with gold nanostructures, gold nanostars, (Figure 15) the most efficient nanostructure to date[7]- were also tested in the same conditions.

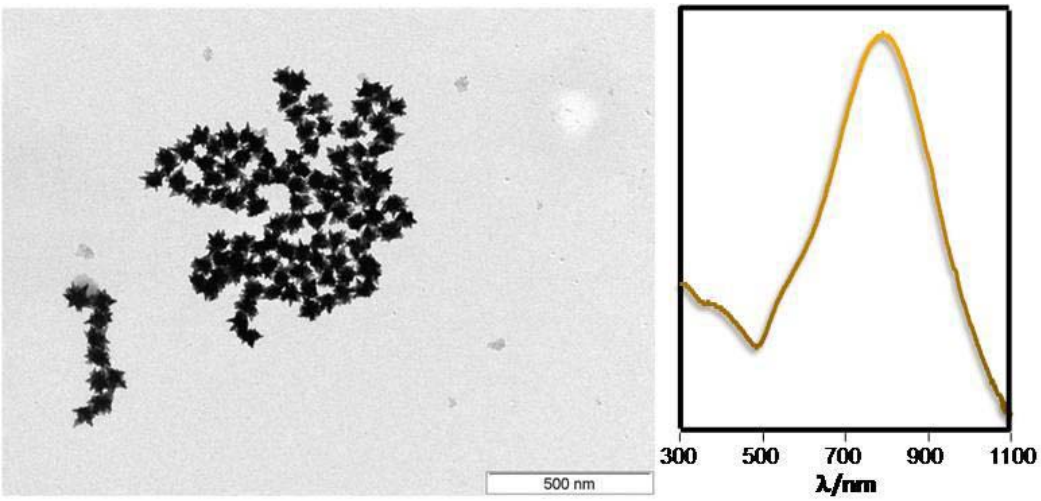

Figure 15. TEM image of gold nanostars and their UV-vis spectrum showing the plasmonic absoprtion.

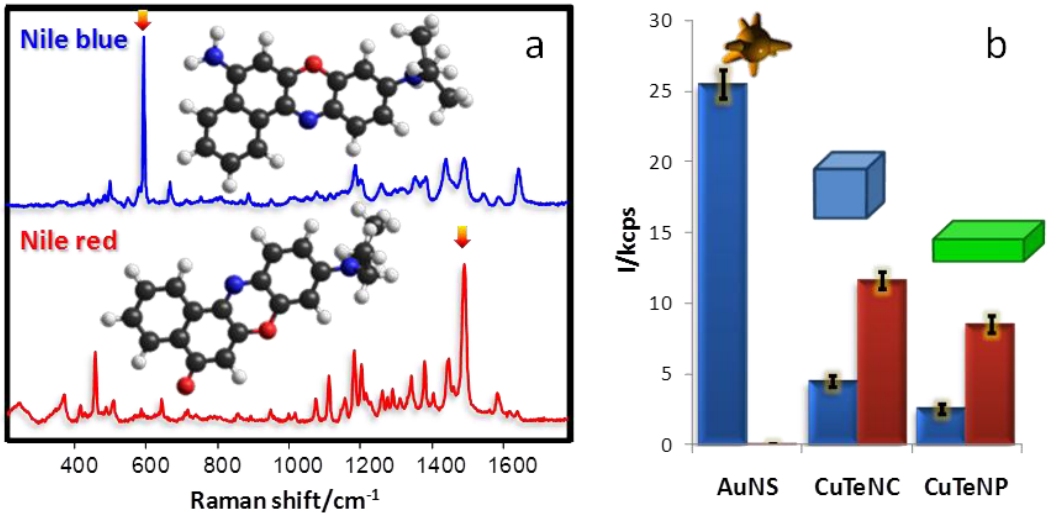

Figure 16. (a) SERS spectra of nile blue and nile red. (b) Comparison of the signal enhancement when using gold nanostars (AuNS), CuTe nanocubes (CuTeNC) and CuTe nanoplates (CuTeNP).

Figure 16 shows the SERS spectra of nile blue and nile red and the enhancement factors for both analytes obtained with gold nanostars and CuTe nanocubes and nanoplates. The CuTe nanorods did not yield any SERS signal, which is consistent with their very weak plasmon peak. The other two, nanocubes and nanoplates, yielded good signal to noise spectra with enhancement factors of 1.5 10^6 and 10^6, respectively for the hydrophobic nile red (Figure 17).

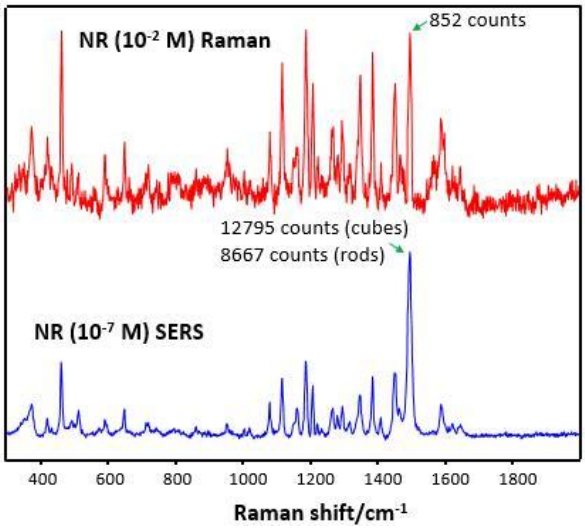

Figure 17. Raman and SERS spectra of a nile red.

This is explained in light of both the copper chemistry and the hydrophobicity of the NPs. The nile blue is a charged molecule thus, although the high affinity of the primary amines for copper, the electrostatic repulsion derived of the analyte charge inhibits the close contact of the target molecule with the surface. In the case of nile red, its hydrophobicity and the tendency of the oxygen containing groups to react with copper makes a much more efficient retention with the subsequent increase in the SERS signal. Notably, cubes offer and slightly higher signal as compared with plates. This phenomenon can be explained in terms of shape and plasmon concentration in the corners which localize the LSPR providing extremely high signals. However,

the fact that the corners of the cubes are not perfectly shaped, reduces this extra enhancement yielding as compared with the plates. Further, comparison of the CuTe nanostructures with the gold nanostars showed that, although the amino-containing molecule gave a considerable higher signal with gold, due to both the photonic efficiency of gold nanostars and the perfect matching between the negatively charged gold surface and the positively charged amino group, the nile red could be only detected with CuTe due to the low affinity of ketones for gold.

5.2.4 Application of CuTe nanocubes in photothermal therapy

Other major application of plasmonic NPs is photothermal therapy. Photothermal therapy uses the local heat produced by plasmonic NPs when absorbing light to kill cancerous cells, which are sensitive to small temperature changes.[23-24] Hyperthermia therapies[23,25] are mostly used together with more conventional therapies such as radiotherapy or chemotherapy.

Gold NPs are typically used for photothermal therapy.[23] In spite of their toxicity, silver NPs have been also proposed for this application. The advantage of using silver instead of gold is that to destroy cancerous cells one can combine the intrinsic toxicity of silver NPs with their ability to increase the local temperature of the tissue.[24] This is of course a relative advantage, as the administration of toxic NPs would require a very careful localization to do not affect healthy cells. NPs with a strong absorption band in the NIR are particularly interesting because at these frequencies light can penetrate through cells and tissues, interacting only with cells containing the NPs, while at other wavelengths strong absorption by tissue occurs.

Also copper sulfide and copper selenide have been recently proposed as photothermal agents.[4-6] Copper telluride is a new candidate material which potential is worth testing. For a preliminary

study of the potential of CuTe NPs as photothermal agents, CuTe nanocubes were stabilized in water by coating them with an amphiphillic polymer (see Chapter 2 and Figure 18, Figure 19, Figure 20).[26-27] The polymer-coated CuTe NPs were extremely stable in water and no agglomeration was detected during periods of over a month.

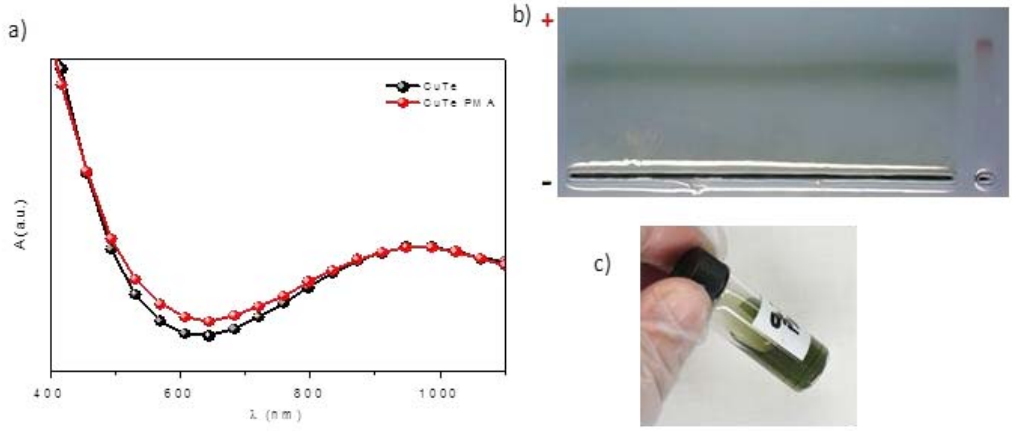

Figure 18. (a) Absorption spectra of CuTe NPs before (black line) and after (red line) the polymer coating procedure. (b) Gel electrophoresis image of the cleaning procedure of the CuTe NPs after their coating. Its electrophoretical mobility is compared with 10 nm Au NPs. (c) Image of the final CuTe NPs solution after the polymer coating process and the cleaning steps.

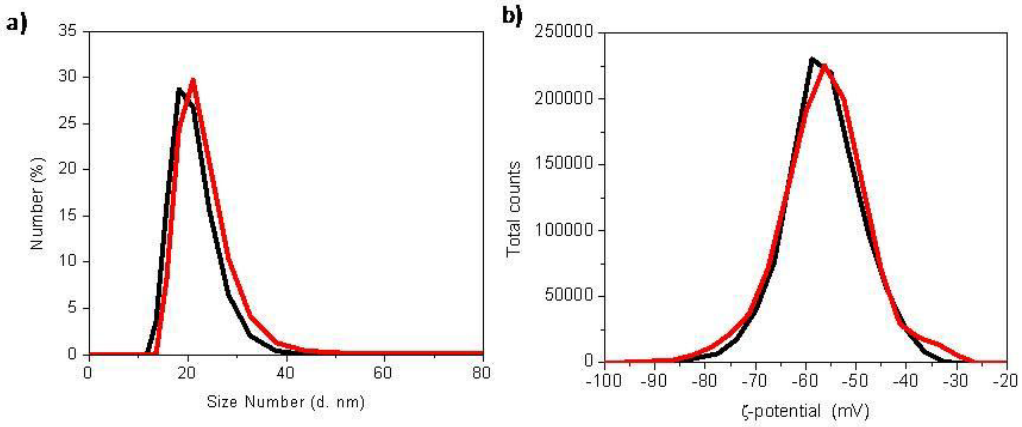

Figure 19. (a) Radius hydrodynamic measurements in number; (b) ζ –potential measurements, both from the final CuTe polymer coated NPs.

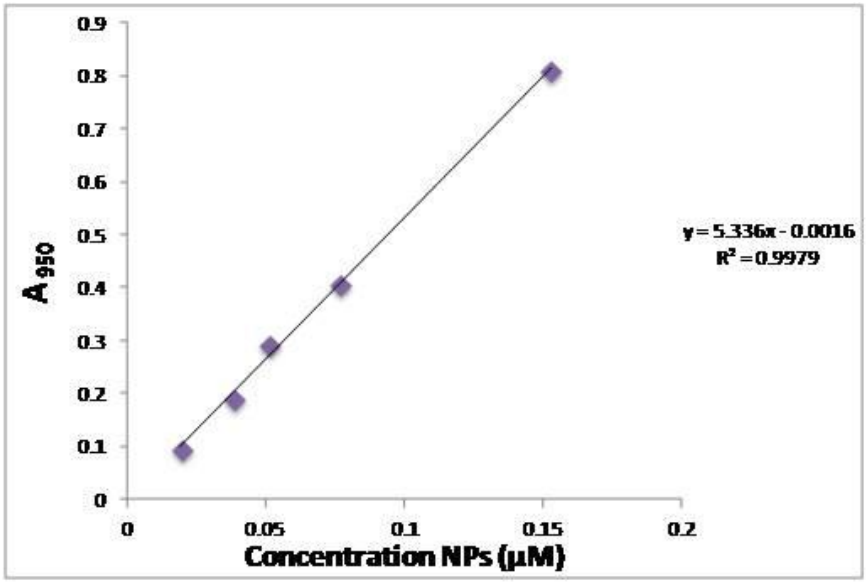

Figure 20. Standard curve for the absorbance at 950 nm of different NPs concentrations in chloroform.

A solution of polymer-coated CuTe nanocubes was used to incubate 3T3 embryonic fibroblast. After incubation, cells were placed in a solution of DAPI (4',6-diamidino-2-phenylindole). DAPI is a dye which only slowly permeates living cells, but its penetration is highly increased in case the plasma and nuclear membranes are damaged. Figure 21 shows transmission and fluorescent images of untreated cells and those containing CuTe nanocubes imaged before and after 830 nm NIR laser irradiation. An increase in the fluorescence intensity of the nucleus is a result of plasma and nuclear membrane damage, which in turn indicates disruption of cell viability. As can be seen in Figure 21, only cells containing the nanocubes were dying. A certain degree of toxicity can be seen as some cells were dying before laser irradiation. This could be due to oxidation of the CuTe NP surface, which would lead to the release of toxic ions. Nevertheless, a significantly higher degree of toxicity was assessed after laser irradiation. These preliminarily results point out that copper telluride could be used as cytotoxic and

photothermal agent. Compared to silver, CuTe NPs have the advantage of displaying their plasmon peak in the NIR, which would allow for selectively targeting NP-labeled cancer cells without affecting unlabeled cells. Although again, their intrinsic toxicity would require a very localized administration or a more efficient encapsulation.[24]

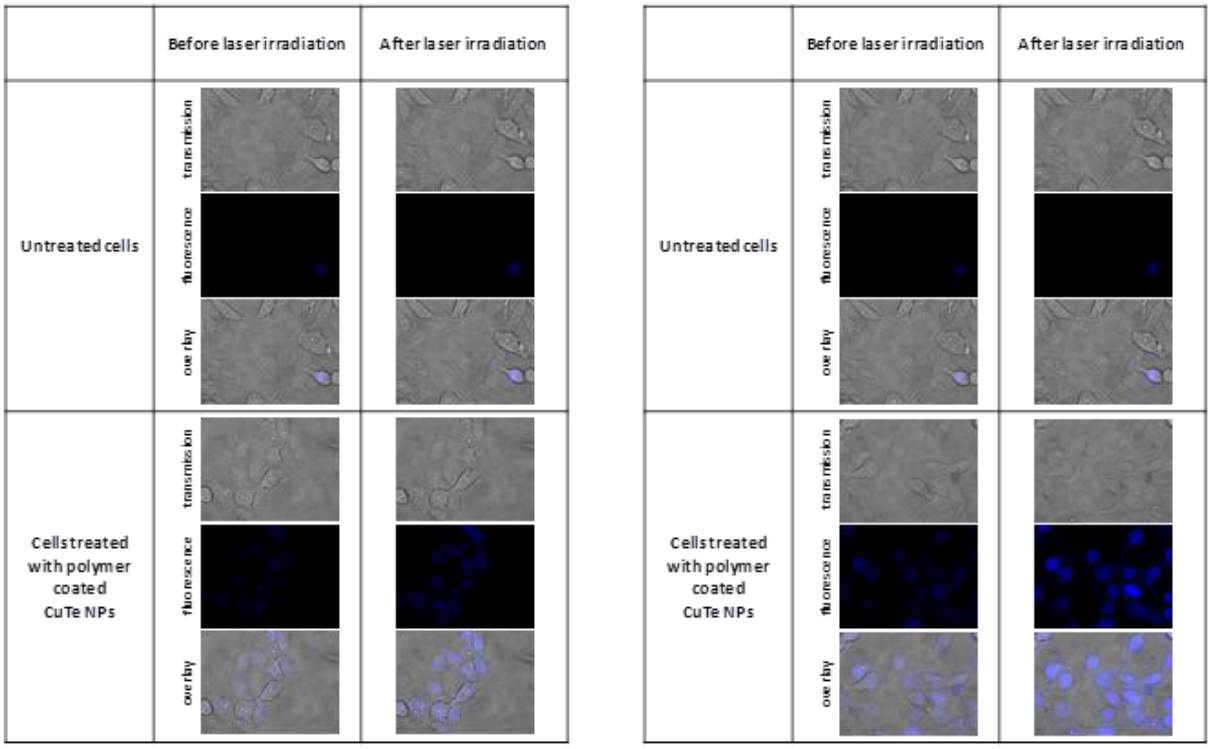

Figure 21. Copper telluride nanocubes-induced disruption of cell viability in two different regions.

5.3 Conclusions

In summary, we have provided a new synthetic method to produce binary semiconductor nanocrystals based on the use of $Li[N(SiMe_3)_2]$, which we demonstrate plays a crucial role for the control the copper telluride nucleation and growth; we finally obtained highly uniform CuTe nanocubes, nanoplates and nanorods in the presence of $LiN(SiMe_3)_2$. These CuTe NPs show a strong plasmonic peak at 950 nm which allowed their use as SERS probes and photothermal

therapy. Here we show for the first time the use of copper chalcogenides as probes for SERS application and demonstrates its interest by showing the ultradetection of a group of molecules here exemplified with nile red that have no affinity for classical SERS probes (gold and silver); While CuTe NPs are not competitive with those of gold for the detection of conventional analytes, they find good applicability for the direct ultradetection of oxygen substituted targets. On the other hand, CuTe nanocubes induced a high degree of toxicity by locally increasing the temperature and possibly by releasing toxic ions to the cellular environment. Furthermore, the results give insights on the potential and the limitations of the still unexplored use of copper telluride nanoparticles in biological application.

5.4 References

(1) Zhao, Y.; Burda, C. *Energy. Environ. Sci.* **2012**, *5*, 5564-5576.

(2) Ibáñez, M.; Cadavid, D.; Zamani, R.; García-Castelló, N.; Izquierdo-Roca, V.; Li, W.; Fairbrother, A.; Prades, J. D.; Shavel, A.; Arbiol, J.; Pérez-Rodríguez, A.; Morante, J. R.; Cabot, A. *Chem. Mater.* **2012**, *24*, 562-570.

(3) Ibáñez, M.; Zamani, R.; Li, W.; Cadavid, D.; Gorsse, S.; Katcho, N. A.; Shavel, A.; López, A. M.; Morante, J. R.; Arbiol, J.; Cabot, A. *Chem. Mater.* **2012**, *24*, 4615–4622.

(4) Hessel, C. M.; Pattani, V. P.; Rasch, M.; Panthani, M. G.; Koo, B.; Tunnell, J. W.; Korgel, B. A. *Nano. Lett.* **2011**, *11*, 2560-2566.

(5) Tian, Q.; Jiang, F.; Zou, R.; Liu, Q.; Chen, Z.; Zhu, M.; Yang, S.; Wang, J.; Wang, J.; Hu, J. *ACS. Nano*. **2011**, *5*, 9761-9771.

(6) Li, Y.; Lu, W.; Huang, Q.; Li, C.; Chen, W. *Nanomedicine* **2010**, *5*, 1161-1171

(7) Kriegel, I.; Jiang, C.; Rodríguez-Fernández, J.; Schaller, R. D.; Talapin, D. V.; da Como, E.; Feldmann, J. *J. Am. Chem. Soc.* **2012**, *134*, 1583-1590.

(8) Dorfs, D.; Härtling, T.; Miszta, K.; Bigall, N. C.; Kim, M. R.; Genovese, A.; Falqui, A.; Povia, M.; Manna, L. *J. Am. Chem. Soc.* **2011**, *133*, 11175-11180.

(9) Li, W.; Shavel, A.; Guzman, R.; Rubio-Garcia, J.; Flox, C.; Fan, J.; Cadavid, D.; Ibáñez, M.; Arbiol, J.; Morante, J. R.; Cabot, A. *Chem. Comm.* **2011**, *47*, 10332-10334.

(10) Li, W.; Zamani, R.; Ibáñez, M.; Cadavid, D.; Shavel, A.; Morante, J. R.; Arbiol, J.; Cabot, A. *J. Am. Chem. Soc.* **2013**, *135*, 4664-4667.

(11) Alvarez-Puebla, R. A.; Liz-Marzan, L. M. *Chem. Soc. Rev.* **2012**, *41*, 43-51.

(12) Alvarez-Puebla, R. A.; Liz-Marzan, L. M. *Angew. Chem. Int. Ed.* **2012**, *51*, 11214-11223.

(13) Liu, S.; Guo, X. Y.; Li, M. G.; Zhang, W. H.; Liu, X. Y.; Li, C. *Angew. Chem. Int. Ed.* **2011**, *50*, 1-5.

(14) Hickey, S. G.; Waurisch, C.; Rellinghaus, B.; Eychmuller, A. *J. Am. Chem. Soc.* **2008**, *130*, 14978–14980.

(15) Kovalenko, M. V.; Heiss, W.; Shevchenko, E. V.; Lee, J. S.; Schwinghammer, H.; Alivisatos, A. P.; Talapin, D. V. *J. Am. Chem. Soc.* **2007**, *129*, 11354-11355.

(16) Kravchyk, K.; Protesescu, L.; Bodnarchuk, M. I.; Krumeich, F.; Yarema, M.; Walter, M.; Guntlin, C.; Kovalenko, M. V. *J. Am. Chem. Soc.* **2013**, *135*, 4199–4202.

(17) Neyvasagam, K.; Soundararajan, N.; Venkatraman, V.; Ganesan, V. *Vacuum* **2007**, *82*, 72-77.

(18) Sridhar, K.; Chattopadhyay, K. *J. Alloys. Compd.* **1998**, *264*, 293-298.

(19) Li, B.; Xie, Y.; Huang, J.; Liu, Y.; Qian, Y. *Chem. Mater.* **2000**, *12*, 2614-2616;

(20) Silva, J. L. F. D.; Wei, S. H.; Zhou, J.; Wu, X. *Appl. Phys. Lett.* **2007**, *91*, 091902;

(21) Mulvaney, P. *Langmuir* **1996,** 12, 788–800.

(22) Luther, J. M.; Jain, P. K.; Ewers, T.; Alivisatos, A. P. *Nat. Mater.* **2011,** 10, 361-366.

(23) Pelaz, B.; Grazu, V.; Ibarra, A.; Magen, C.; del Pino, P.; de la Fuente, J. M. *Langmuir* **2012**, *28*, 8965-8970.

(24) Di Corato, R.; Palumberi, D.; Marotta, R.; Scotto, M.; Carregal-Romero, S.; Rivera_Gil, P.; Parak, W. J.; Pellegrino, T. *Small* **2012**, *8*, 2731-2742.

(25) Martínez-Boubeta, C. *Sci. Rep.* **2013**, *3*, 1652.

(26) Pellegrino, T.; Manna, L.; Kudera, S.; Liedl, T.; Koktysh, D.; Rogach, A. L.; Keller, S.; Radler, J.; Natile, G.; Parak, W. J. *Nano. Lett.* **2004**, *4*, 703-707.

(27) Zhang, F.; Lees, E.; Amin, F.; Rivera-Gil, P.; Yang, F.; Mulvaney, P.; Parak, W. J. *Small* **2011**, *7*, 3113-3127.

Conclusions

This dissertation has focused mainly on the synthesis of shape and size-controlled Cu chalcogenide nanocrystals and intensive explorations of their functional properties used in rich variety applications. The conclusions can be extracted as following:

(1) The Cu_xS nanoparticles with different morphologies (nano-spheres, disks, polyhedrons including tetradecahedrons and dodecahedrons) can be successfully obtained by simply tuning the precursor (Cu) concentration. It can attribute to the low nucleation rate of nanocrystals which results in a high monomer concentration remaining in solution after nucleation and ensure a moderately slow but continuous growth of the nanocrystals. The established focusing regime with diffusion-reaction model is tested experimentally here for copper sulphide polyhedrons growing in a so slow way. The selection of Cu precursor along with the choice of oleylamine as both solvent and stabilizer is vital in this synthesis. The use of Di-tert-butyl disulfide (TBDS) as a ligand and sulphur precursor is shown to be critical to form the monodisperse shaped nanoparticles.

(2) The formation of a novel geometry of Cu_xSe, namely the nanocube was described in detail. The foreign ions of Al^{3+} play the critical role during the grow process which catalyzed the formation of the final nanocubes. This is also the first report using metal ions to control the morphology of semiconductors. The result is significant and it establishes a totally new strategy for shape control in semiconductor nanocrystal synthesis.

(3) The research of binary Cu chalcogenide is extended to another material: Cu_xTe. It's a new synthetic method proposed to produce binary semiconductor nanocrystals based on the use of $LiN(SiMe_3)_2$ which has been demonstrated playing a crucial role for the control of copper telluride nucleation and growth process. To be specific, the $-N(SiMe_3)_2$ groups induce the burst nucleation event where Li-oleylamido complex is crucial to control the shape and size of Cu_xTe nanocrystals. The copper telluride nanocubes and plates possess narrow size distribution and show localized surface plasmon resonance in near-IR region, in accordance with copper selenide presented in Chapter 5. The results provide significant progress not only on synthetic methods but also on the application of these nanomaterials produced. Both the nanocubes and nanoplates yielded good SERS signal with a millionfold enhancement compared to that of noise spectra whereas no any signal was detected from Au as classic probe. In photothermal therapy test, disruption of cell viability was observed after laser irradiation which indicates the potential interests of these nanocrystals as cytotoxic and photothermal agent.

Curriculum Vitae

PERSONAL DATA

Wenhua Li

Birthday: 8th November of 1982

Nationality: Chinese

Adress: C. Lope de Vega, 98, P2 1a, 08005, Barcelona. (Spain)

Phone number: +34 688003082

E-mail: liwhhappy@gmail.com, liwenhua@irec.cat

ACADEMIC TRAINING

09/2002 -06/2006	Degree in Chemistry.	Lanzhou University, Lanzhou, China.
09/2006- 07/2009	Master in Physical Chemistry	ShanDong University, Jinan, China
02/ 2010-Present	PhD Program	University of Barcelona, Barcelona, Spain.

FELLOWSHIPS

07/2003-07/2005	School scholarship	Chinese Government
11/2008- 01/2009	Mobility Grant. Max Planck Institute of colloid and interfaces (Potsdam, Germany)	German Government
02/2010- 02/2014	PhD Fellowship	Energy Research Institute of Catalonia -IREC

PROFESSIONAL EXPERIENCE

Period	**Position/University/Advisor**	**Research topic**
09/2006-07/2009	Junior researcher. Key Laboratory of Colloidal and Interface Chemistry, Ministry of Education. ShanDong University. China. *Prof. Renjie Zhang*	**The fabrication of Chitosan-Sodium alginate microcapsules via layer by layer technique and their characterisation.**
11/2008- 01/2009	Visiting researcher. Interfaces. Max Planck Institute of colloid and interfaces. Potsdam, Germany. *Director of the group Interfaces-Helmuth Möhwald.*	**The fabrication and characterisation of the PAH-PSS microcapsules.**
03/2011-07/2011	Visiting researcher. Physics Department. Ludwig-Maximilians-Universität München. *Head of the group-Jochen Feldmann.*	**Synthesis of copper chalcogenide nanoparticles and their optical properties studies.**

12/2012	Visiting researcher. Physics Department. Philipps University Marburg, Germany. *Head of the group-Wolfgang J. Parak*	**Transfer the hydrophobic colloidal Cu_xSe and Cu_xTe nanocrystals in aqueous solution by the polymer coating procedures**.

RESEARCH INTEREST

Synthesis and characterization of semiconductor and metalic nanocrystals: The control at the nanoscale of the size, morphology, composition and crystallinity of copper chalcogenides in a colloidal solution so as to make their optical and optoelectronic properties tunable by editing the electron energy state; one main part is focused on the copper binary nanocrystals and their plasmonic properties.

Energy-related applications of nanomaterials: Applications of semiconductor and metallic nanomaterials in photoelectronics, photovoltaic, thermoelectric and catalytic applications. Charge and heat transport in nanocrystal solids.

Plasmonic-related applications of nanocrystals: Applications as Surface Enhanced Raman Scattering sensors, photothermal therapy based on the heat induced by the incident light.

PUBLICATIONS

1. **W. Li**, R. Zamani, P. Rivera-Gil, B. Pelaz, M. Ibáñez, D. Cadavid, A. Shavel, R. A. Alvarez-Puebla, W. J. Parak, J. Arbiol, and A. Cabot; *"CuTe Nanocrystals: Shape and Size Control, Plasmonic Properties, and Use as SERS Probes and Phototherma Agents" J. Am. Chem. Soc.* **2013**, 135, pp 7098-7101.

2. **W. Li**, R. Zamani, M. Ibáñez, D. Cadavid, A. Shavel, J. R. Morante, J. Arbiol, and A. Cabot; "*Metal Ions to Control the Morphology of Semiconductor Nanoparticles: Copper Selenide Nanocube" J. Am. Chem. Soc.* **2013**, 135, pp 4664-4667.

3. M. Ibáñez, D. Cadavid, U. Anselmi-Tamburini, R. Zamani, S. Gorsse, **W. Li**, A. Shavel, A. M. López, J. Arbiol, J. R. Morante, and A. Cabot; "*Colloidal Synthesis and Thermoelectric Properties of Cu_2SnSe_3 Nanocrystals*" *J. Mater. Chem. A* **2013***,* 1, pp 1421-1426.

4. M. Ibáñez**,** D. Cadavid, U. Anselmi-Tamburini, R. Zamani, S. Gorsse, **W. Li**, A. Shavel, A. M. López, J. Arbiol, J. R. Morante, and A. Cabot; "*Crystallographic Control at the Nanoscale to Enhance Funcionality: Polytypic Cu_2GeSe_3 Nanoparticles as Thermoelectric Materials" Chem. Mater. 2012*, 24, pp 4615–4622.

5. M. Ibáñez, R. Zamani, **W. Li**, A. Shavel, J. Arbiol, J. R. Morante, and A. Cabot; "*Extending the Nanocrystal Synthesis Control to Quaternary Compositions*" *Cryst. Growth. Des.* **2012**, 12, pp 1085-1090.

6. M. Ibáñez, R. Zamani, A. LaLonde, D. Cadavid, **W. Li**, A. Shavel, J. Arbiol, J. R. Morante, S. Gorsse, G. J. Snyder, and A. Cabot; "*$Cu_2ZnGeSe_4$ Nanocrystals: Synthesis and Thermoelectric Properties" J. Am. Chem. Soc.* **2012**, 134, pp 4060–4063.

7. M. Ibáñez, D. Cadavid, R. Zamani, N. García-Castelló, V. Izquierdo-Roca, **W. Li**, A. Fairbrother, J. D. Prades, A. Shavel, J. Arbiol, A. Pérez-Rodríguez, J. R. Morante, and A. Cabot; "*Composition Control and Thermoelectric Properties of Quaternary Chalcogenide Nanocrystals: The Case of Stannite $Cu_2CdSnSe_4$*" *Chem. Mater.* **2012**, 24, pp 562–570.

8. M. Ibáñez, J. Fan, **W. Li**, D. Cadavid, R. Nafria, A. Carrete, and A. Cabot; *"Means and limits of control of the shell parameters in hollow cadmium chalcogenides obtained by the Kirkendall effect"; Chem. Mater***. 2011**, 23, pp 3095–3104.

9. **W. Li**, A. Shavel, R. Guzman, R. Guzman, J. Rubio-Garcia, C. Flox, J. Fan, D. Cadavid**,** M. Ibáñez, J. Arbiol, and A. Cabot; *"Morphology Evolution of $Cu_{2-x}S$ Nanoparticles: From Spheres to Dodecahedrons"* *Chem. Commun***. 2011**, 47, pp 10332-10334.

10. **W. Li**, Maria Ibañez, Javier Rubio-Garcia, Joan Ramon Morante, and Andreu Cabot; *"Colloidal Synthesis and Functional Properties of Quaternary Cu-Based Semiconductors: $Cu_2HgGeSe_4$"* Under Review

11. **W. Li**, Maria Ibañez, Doris Cadavid, Joan Ramon Morante, and Andreu Cabot; *"I_2-II-IV-VI_4 Nanoparticles: The case of $Cu_2HgSnSe_4$",* submitted.

PARTICIPATION IN CONFERENCES AND SEMINARS

1. **W. Li**, M. Ibáñez, R. Zamani, D. Cadavid, J. Arbiol, and A. Cabot; *Colloidal synthesis of Quaternary chalcogenide nanocrystals and their thermoelectric properties; EMRS-Spring meeting 2013;* Oral Presentation.

2. **W. Li**, R. Zamani, P. Rivera-Gil, B. Pelaz, M. Ibáñez, D. Cadavid, A. Shavel, R. A. Alvarez-Puebla, W. J. Parak, J. Arbiol, and A. Cabot; *Synthesis and Characterization of shape-controlled Cu_xTe nanoparticles ; EMRS-Spring meeting 2013;* Poster Presentation.

3. R. Zamani, M. Ibáñez, **W. Li**, D. Cadavid, J.R. Morante, A. Cabot and J. Arbiol; *Structural and morphological Changes in $I_2II\ IV\ VI_4$ adamantines for thermoelectric application; European Microscopy Congress 2012 (EMC2012),* Poster Presentation.

4. A. Cabot , M. Ibáñez, D. Cadavid, **W. Li**, A. Shavel, and J. R. Morante; *Bottom-up processing of nanocomposites for thermoelectric applications,* $NaNaX_5$ (*Nanoscience with Nanocrystals*) 2012; Poster Presentation.

Annex

Colloidal Synthesis and Functional Properties of Quaternary Cu-Based Semiconductors: $Cu_2HgGeSe_4$

Wenhua Li,[a] Maria Ibáñez,[b] Doris Cadavid,[a] Reza Zamani,[a,c] Javier Rubio-Garcia,[a] Stéphane Gorsse,[d] Joan Ramon Morante,[a,b] Jordi Arbiol [c,e] and Andreu Cabot *[a,b]

[a] Catalonia Energy Research Institute (IREC), Jardí de les Dones de Negre 1, Planta 2, E-08930, Sant Adria del Besos, Barcelona, 08930, Spain

[b] Departament Electronica, Universitat de Barcelona, Barcelona 08028, Spain

[c] Institut de Ciència de Materials de Barcelona (ICMAB-CSIC), Campus de la UAB, Bellaterra 08193, Spain

[d] CNRS, Université de Bordeaux, ICMCB, 87 avenue du Docteur Albert Schweitzer, 33608 Pessac Cedex, France

[e] Institució Catalana de Recerca i Estudis Avançats (ICREA), 08010 Barcelona, Spain

Corresponding author: Dr. Andreu Cabot

Phone: +34 625615115

Fax: +34 934021148

acabot@irec.cat

KEYWORDS:

Quaternary nanoparticles; $Cu_2HgGeSe_4$; thermoelectric.

ABSTRACT

Herein a colloidal synthetic route to prepare $Cu_2HgGeSe_4$ (CHGSe) nanoparticles and the results from their structural and optical characterization are presented. The high yield of the developed procedure allows the production of CHGSe colloidal nanoparticles at the gram scale. These nanoparticles were used as building blocks for the production of CHGSe bulk nanostructured materials, which thermoelectric properties were characterized in the temperature range from 300 to 730 K. CHGSe nanomaterials showed an optical band-gap of 1.6 eV, reached electrical conductivities up to $5x10^4$ Sm^{-1}, Seebeck coefficients above 100 $\mu V\ K^{-1}$ and thermal conductivities below 1.0 $Wm^{-1}K^{-1}$ what translated into thermoelectric figures of merit up to 0.34 at 730 K.

1. Introduction

The ample structural and chemical flexibility of ternary and quaternary compound semiconductors offer a potential pool for engineering their chemical and physical properties and to develop new and optimized technological applications. In this direction, tetrahedrally-coordinated ternary and quaternary copper-based chalcogenides are a particularly interesting family of materials [1-7]. They are p-type semiconductors with applications in the fields of photovoltaics [1,2,8], photocatalysis [9], and thermoelectricity [3,5,7,10]. Within this wide family, a relatively unexplored but potentially valuable material is $Cu_2HgGeSe_4$ (CHGSe). CHGSe is a p-type semiconductor which at room temperature shows a Seebeck coefficient (S) of 208 mV K^{-1}, an electrical conductivity (σ) of $8x10^4$ S m^{-1} and a thermal conductivity (κ) of 2.0 W m^{-1} K^{-1}, resulting in dimensionless thermoelectric figure of merit ($ZT=\sigma S^2/\kappa$) of 0.05 [11].

We present here a procedure to synthesize CHGSe nanoparticles (NPs) with controlled composition. While the synthesis of elemental and binary nanocrystals, including Cu-based binary chalcogenides, has reached a considerable maturity level [12-16], the production of ternary and quaternary nanocrystals still represents an important challenge. Herein, CHGSe colloidal NPs were used as building blocks to produce bulk nanostructured materials. We further characterized their electrical conductivity, Seebeck coefficient and thermal conductivity in the temperature range from 300 to 730 K.

2. Experimental details

Selenium solution (ODE:Se): A 0.8 M SeO_2-octadecene (ODE) solution was obtained by dissolving SeO_2 (8.87 g, 80 mmol) in 100 mL of ODE under argon atmosphere at 180 °C. The mixture was additionally stirred at 180 °C for 5 h to obtain a perfectly clear brownish orange solution.

Synthesis of $Cu_2HgGeSe_4$ nanocrystals: CuCl (0.25 mmol), $HgCl_2$ (0.125 mmol) and hexadecylamine (HDA, 5 mmol) where mixed with ODE (9 g) within a four-neck flask. The solution was heated under argon flow to 200 ºC and maintained at this temperature during 1 h to remove water and other low-boiling point impurities. Afterwards, the yellowish transparent solution was cooled down to 120 ºC and 0.125 mmol of $GeCl_4$ in 0.25 mL ODE was injected. Then the solution was heated up to 285 ºC and 2 mL of the 0.8 M SeO_2-ODE solution was injected. The solution was allowed to react for 5 min. The formation of CHGSe NPs could be qualitatively followed by the color change of the mixture from an initial light yellow to green and eventually to the black color of the solution containing CHGSe NPs. 3 mL of oleic acid (OA) was added to the mixture during the cooling step, at ~70 °C, to replace the weakly bound

HDA.

Characterization: Transmission electron microscopy (TEM) and High-resolution TEM (HRTEM) micrographs were obtained using a Jeol 2010F field-emission gun microscope with a 0.19 nm point- to-point resolution at 200 keV with an embedded Gatan image filter for electron energy loss spectroscopy (EELS) analyses. Powder x-ray diffraction (XRD) patterns were obtained with Cu Kα (λ = 1.5406 Å) radiation in a reflection geometry on a Bruker D8 operating at 40 kV and 40 mA. Scanning electron microscopy (SEM) was performed using a ZEISS Auriga with an energy dispersive X-ray spectroscopy (EDX) detector to study composition. Raman scattering measurements were obtained in backscattering geometry with dispersive spectrometer Jobin-Yvon LabRam HR 800, coupled to an optical microscope Olympus BXFM. Excitation was provided by an argon-ion laser operating at a wavelength of 532.0 nm with a low incident power to avoid thermal effects. Seebeck coefficients and electrical conductivities were measured simultaneously using a Linseis - LSR 3 system. Analyses were carried out under helium atmosphere. The Seebeck coefficient was measured using a static DC method. The electrical conductivity was measured using a standard four probe technique. Thermal conductivity values were obtained from flash diffusivity measurements (Netzsch LFA-457 Microflash) using the mass density and the Dulong-Petit approximation to determine the specific heat capacity.

3. Results and discussion

CHGSe NPs were prepared by reacting metal-amine complexes with an excess of selenium in ODE as detailed in the experimental section. Figure 1A shows a representative TEM micrograph of the 35 ± 3 nm CHGSe NPs prepared by the above described procedure. TEM analysis showed

the NPs to have tight size distributions with size dispersions below 10 %. CHGSe NPs were polycrystalline and showed a poly-tetrahedral morphology. HRTEM showed the NPs crystal structure to have tetragonal-symmetry with I42m space group [22] and further confirmed the CHGSe NPs to contain multiple twin defects (Figure 1A).

NPs composition was determined by EDX and EELS. When using stoichiometric ratios of precursors, the final NPs were systematically Hg-deficient: $Cu_{2.3}Hg_{0.7}Ge_{1.0}Se_{4.2}$. To produce stoichiometric NPs, the presence of excess amounts of $HgCl_2$ in the precursor solution was found necessary. Figure 1B shows a representative TEM micrographs of the stoichiometric CHGSe NPs obtained with a nominal Cu:Hg:Ge precursor concentration of 2:2:1. Setting the reaction time to 5 min, an excess of Hg in the precursor solution resulted in 17 ± 3 nm single-crystal NPs. Excess amounts of Hg were experimentally observed to prevent the formation of twin defects by accelerating the overall reaction. As a result, smaller but single-crystalline NPs were obtained. Single NP chemical analyses using EELS confirmed the presence of the 4 elements within each NP and showed their distribution to be homogeneous across the whole NP (Figure 1C).

The evolution of the NP composition with the reaction time was followed by extracting and chemically analyzing multiple aliquots. Upon injection of the 0.8 M SeO_2-ODE solution, $Cu_{2-x}Se$ NPs were immediately formed. With the reaction time, Hg and Ge ions gradually diffused into the crystallographic structure, which evolved from the cubic berzalite $Cu_{2-x}Se$ to the tetragonal $Cu_{2+x}Hg_{1-x}GeSe_4$.

XRD analysis (Figure 2A) confirmed the crystal structure of the CHGSe NPs to have a tetragonal-symmetry with I42m space group (JCPDS: 01-074-8343) [17]. The XRD pattern of stoichiometric NPs obtained in an excess of $HgCl_2$ showed additional reflections associated to the cubic HgSe phase. To further determine the material phase purity, the materials were

characterized by Raman spectroscopy (Figure 2B). The Raman spectra of CHGSe NPs showed two main peaks at 175.6 and 198.7 cm^{-1}, which corresponds to the A symmetry modes of the CHGSe crystal structure, in analogy with the $Cu_2ZnSnSe_4$ (CZTSe) case [18]. No clear evidence of other secondary phases was obtained by this technique.

The experimental optical band-gap of CHGSe was estimated from UV-vis spectroscopy at 1.6 eV (Figure 2C). The absorption band extending from 100 nm to wavelengths above 2500 nm was associated to the presence of the low-band gap HgSe secondary phase.

The described synthetic route was easily scaled up to produce CHGSe NPs at the gram scale with identical size and composition control. To characterize their functional properties roughly 2 g of stoichiometric and copper-rich CHGSe NPs were prepared. NPs were intensively washed by multiple precipitation and re-dispersion steps until they were no longer soluble in organic solvents. Then they were annealed at 500 °C for 2 h under argon atmosphere, grinded into a fine powder and consolidated into bulk nanocrystalline materials under a 2 tons load at room temperature. The relative densities of the obtained pellets were in the range between 80 and 85 %.

With the annealing treatment, the crystal domain size increased roughly a factor 1.7 as calculated from the fitting of the XRD patterns, and no change of composition or crystallographic phase was observed. The combustion of the residual organic ligands resulted in residual carbon amounts between 0.5 and 1 % in the final pellet, as measured by elemental analysis.

The electrical conductivity of the Cu-rich, $Cu_{2.3}Hg_{0.7}Ge_{1.0}Se_{4.2}$, nanocrystalline pellets was higher than the stoichiometric $Cu_2HgGeSe_4$ (Figure 3A). We associated this increase of electrical

conductivity to the higher hole concentration obtained by the replacement of Hg^{2+} by Cu^{1+} ions. Such partial replacement or intrinsic doping is a key strategy to control the Fermi level in bottom-up assembled multi-valence nanomaterials, as the introduction of extrinsic dopants in colloidal NP building blocks remains a non-solved challenge.

As expected in a heavily doped semiconductor, when increasing the carrier concentration by the Hg-by-Cu replacement, the Seebeck coefficient decreased (Figure 3B). Despite the reduction of the Seebeck coefficient, the power factor (σS^2) of copper-rich nanomaterials was much higher than for stoichiometric compounds, up to 0.381 $mW/m \cdot K^2$.

We further calculated the thermal conductivity of the Cu-rich nanocrystalline material from flash diffusivity measurements. We used the material's mass density and the Dulong-Petit approximation for its specific heat capacity (Cp= 0.34 $J \cdot g^{-1}K^{-1}$). Figure 3C and 3D display the thermal conductivity and the calculated thermoelectric figure of merit, ZT, of $Cu_{2.3}Hg_{0.7}Ge_{1.0}Se_{4.2}$ nanocrystalline materials, which reached up to 0.34 at 460 ºC.

4. Conclusion

To summarize, a synthetic route to produce CHGSe NPs was detailed. The proposed route required excess amounts of Hg to obtain stoichiometric CHGSe compositions. CHGSe NPs showed a band-gap at 1.6 eV. They were used as building blocks to produce bulk nanocrystalline materials. Cu-rich CHGSe nanocrystalline materials reached electrical conductivities up to $5x10^4$ Sm^{-1}, Seebeck coefficients above 100 $\mu V\ K^{-1}$ and thermal conductivities below 1.0 $Wm^{-1}K^{-1}$ what translated into thermoelectric figures of merit up to 0.34 at 460 ºC.

Acknowledgements

The research was supported by the European Regional Development Funds (ERDF, "FEDER Programa Competitivitat de Catalunya 2007-2013").

References

(1) Shavel, A.; Arbiol, J.; Cabot, A. *J. Am. Chem. Soc.* **2010**, *132*, 4514-4515.

(2) Shavel, A.; Cadavid, D.; Ibáñez, M.; Carrete, A.; Cabot, A. *J. Am. Chem. Soc.* **2012**, *134*, 1438-1441.

(3) Ibáñez, M.; Zamani, R.; LaLonde, A.; Cadavid, D.; Li, W. H.; Shavel, A. *J. Am. Chem. Soc.* **2012**, *134*, 4060-4063.

(4) Singh, A.; Geaney, H.; Laffir, F. R.; Ryan. K. M.; *J. Am. Chem. Soc.* **2012**, *134*, 2910-2913.

(5) Ibáñez, M.; Zamani, R.; Li, W. H.; Gorsse, S.; Katcho, N. A.; Shavel, A. *Chem. Mater.* **2012**, *24*, 4615-4622.

(6) Ibáñe, M.; Zamani, R.; Li, W. H.; Shavel, A.; Arbiol, J.; Morante, J. R.; Cabot, A. *Cryst. Growth. Des.* **2012**, *12*, 1085-1090.

(7) Ibáñez, M.; Cadavid, D.; Zamani, R.; Castelló, N. G.; Roca, V. I.; Li, W. H.; *Chem. Mater.* **2012**, *24*, 562-570.

(8) Mitzi, D. B.; Gunawan, O.; Todorov, T. K.; Wang, K.; Guha, S. *Sol. Energ. Mat. Sol. C* **2011**, *95*, 1421-1436.

(9) Yokoyama, D.; Minegishi, T.; Jimbo, K.; Hisatomi, T.; Ma, G.; Katayama, M. *Appl. Phys. Express.* **2010**, *3*, 101202-101204.

(10) Liu, M. L.; Chen, I. W.; Huang, F. Q.; Chen, L. D. *Adv. Mater.* **2009**, *21*, 3808-3812.

(11) Hirai, T.; Kurata, K.; Takeda, A. *Solid-State. Electronics. Pergamon.* **1967**, *10*, 975-981.

(12) Yin, Y.; Alivisatos, A. P. *Nature* **2004**, *437*, 664-670.

(13) Li, W. H.; Shavel, A.; Guzman, R.; Garcia, J. R.; Flox, C.; Fan, J. D. *Chem. Commun.* **2011**, *47*, 10332-10334.

(14) Ibáñez, M.; Guardia, P.; Shavel, A.; Cadavid, D.; Arbiol, J.; Morante, J. R. *J. Phys. Chem. C* **2011**, *115*, 7947-7955.

(15) Li, W. H.; Zamani, R.; Ibáñez, M.; Cadavid, D.; Shavel, A.; Morante, J. R. *J. Am. Chem. Soc.* **2013**, *135*, 4664-4667.

(16) Li, W. H.; Zamani, R.; Gil, P. R.; Pelaz, B.; Ibáñez, M.; Cadavid, D. *J. Am. Chem. Soc.* **2013**, *135*, 7098-7101.

(17) Olekseyuk, I. D.; Gulay, L. D.; Dydchak, I. V.; Piskach, L. V.; Parasyuk, O. V.; Marchuk, O. V. *J. Alloys. Compd.* **2002**, *340*, 141-145.

(18) Redinger, A.; Hönes, K.; Fontané, X.; Izquierdo-Roca, V.; Saucedo, E.; Valle, N. *Appl. Phys. Lett.* **2011**, *98*, 1019030-1019037.

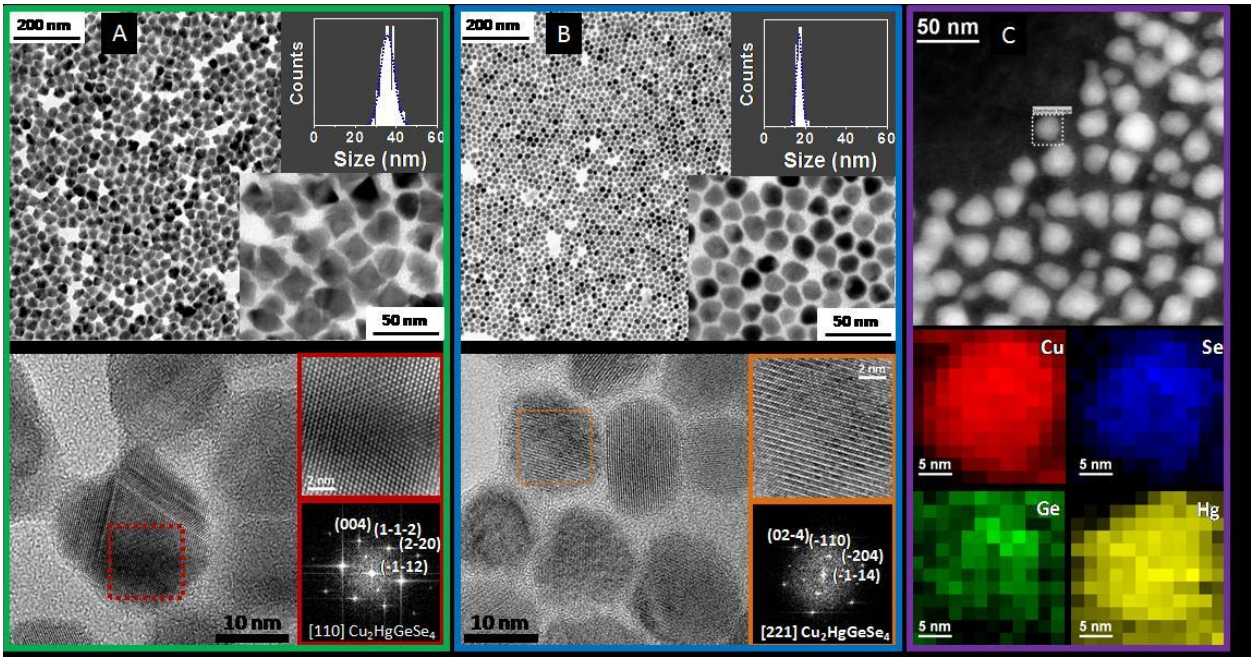

Fig 1. Representative TEM micrographs (top) and HRTEM (bottom) of $Cu_{2.3}Hg_{0.7}Ge_{1.0}Se_4$ (A) and $Cu_2HgGeSe_4$ NPs (B). HAADF image of $Cu_2HgGeSe_4$ NPs and single NP compositional maps (C).

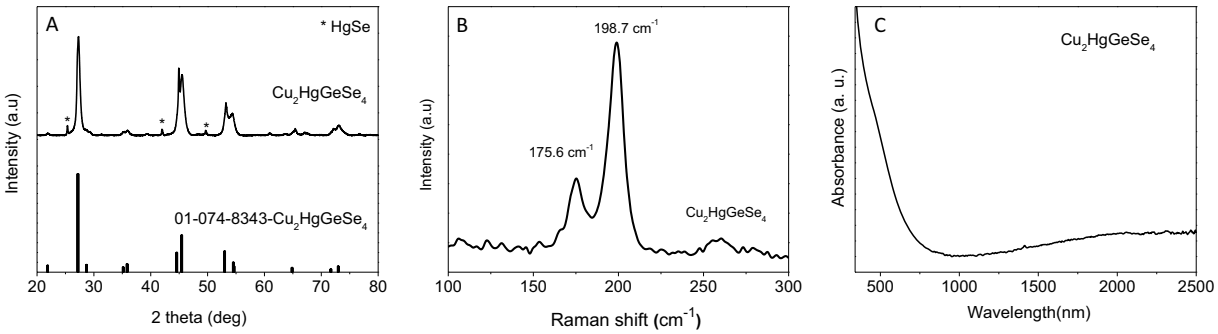

Fig 2. XRD pattern (A), Raman spectrum (B) and UV-vis spectrum (C) of $Cu_2HgGeSe_4$ NPs.

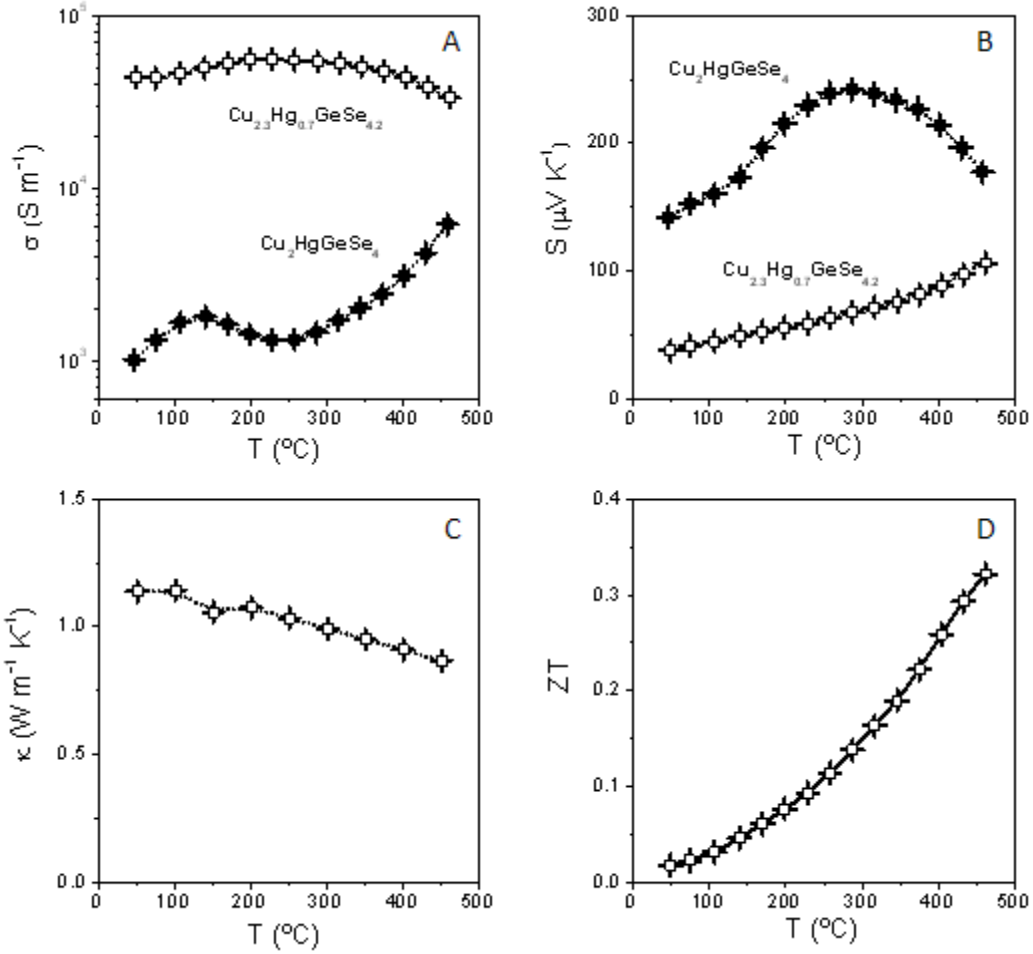

Fig 3. Electrical conductivity (A) and Seebeck coefficient (B) of the $Cu_{2.3}Hg_{0.7}Ge_{1.0}Se_{4.2}$ and $Cu_2HgSnSe_4$ bulk nanostructured materials. Thermal conductivity (C) and thermoelectric figure of merit (D) of $Cu_{2.3}Hg_{0.7}Ge_{1.0}Se_{4.2}$ bulk nanomaterial.

I_2-II-IV-VI_4 Nanoparticles: The case of $Cu_2HgSnSe_4$

Wenhua Li,[a] Maria Ibáñez,[a] Reza Zamani,[a,b] Doris Cadavid,[a] Nuria García-Castelló,[c] Joan Daniel Prades,[c] Stephane Gorsse,[d] Jordi Arbiol[b,e] and Andreu Cabot[a,c*]

[a] *Catalonia Institute for Energy Research, IREC, 08930 Sant Adria del Besos (Barcelona), Spain;*

[b] *Institut de Ciència de Materials de Barcelona, ICMAB-CSIC, Campus de la UAB, Bellaterra, 08193, Spain.*

[c] *Departament d'Electrònica, Universitat de Barcelona, 08028 Barcelona, Spain*

[d] *CNRS, Université de Bordeaux, ICMCB, 87 avenue du Docteur Albert Schweitzer, 33608 Pessac Cedex, France*

[e] *Institució Catalana de Recerca i Estudis Avançats (ICREA), 08010 Barcelona, Spain*

*E-mail: acabot@irec.cat

Abstract

The compositional versatility of I_2-II-IV-VI_4 tetrahedrally-coordinated compounds allows accommodating their electronic, optic, optoelectronic and thermoelectric properties to numerous technological applications. In particular, $Cu_2ZnSnSe_4$ is used in the field of photovoltaics and $Cu_2CdSnSe_4$ has been proved an excellent thermoelectric material. The third compound of this family, $Cu_2HgSnSe_4$, remains relatively unexplored. $Cu_2HgSnSe_4$ is believed to be a low band gap semiconductor with potential for infra-red optical detection and thermoelectrics, although no experimental results support these assumptions. Herein, a synthetic route to produce $Cu_2HgSnSe_4$ nanoparticles with narrow size distribution and controlled composition is presented. Their physical, chemical and optical properties were characterized. $Cu_2HgSnSe_4$ nanoparticles were further used as building blocks to produce bulk nanocrystalline materials, which thermoelectric properties were analyzed. A very preliminary adjustment of the material composition yielded Seebeck coefficients up to 160 μVK^{-1}, electrical conductivities close to 10^4 Sm^{-1} and thermal conductivities down to 0.5 $Wm^{-1}K^{-1}$.

1. Introduction

The ample chemical and structural freedom of multinary semiconductors allows engineering their functional properties to fulfill numerous applications.[1-4] In particular, Cu-based I_2-II-IV-VI_4 tetrahedrally-coordinated compounds can be found at the origin of various technological innovations. $Cu_2ZnSnSe_4$ (CZTSe) is the main low-cost and environmental friendly alternative to conventional photovoltaic materials, i.e. Si, CdTe, $CuIn_{1-x}Ga_xSe_2$.[5,6] CZTSe combines numerous advantageous characteristics for optoelectronic applications, such as a direct band gap at 1.0-1.4 eV,[4] a high optical absorption coefficient up to 10^5 cm^{-1},[5] a low toxicity and the relative high abundance of its elements. A second compound of this family, $Cu_2CdSnSe_4$ (CCTSe), shows excellent thermoelectric properties, with ZT values up to 0.7 at 700 K.[7-11] The third compound of this family, $Cu_2HgSnSe_4$ (CHTSe), remains relatively unexplored.

While they all are p-type semiconductors, the optoelectronic and thermoelectric properties of Cu_2ASnSe_4 (A=Zn, Cd, Hg) compounds strongly depend on the II element (Table 1).[12] The three compounds are characterized by high absorption coefficients and direct band gaps which narrows with the atomic weight of the II element, from 1.0-1.4 eV for CZTSe to 0.17 eV theoretically predicted for CHTSe.[13] Crystallographically, the three compounds have a diamond-like phase.[14, 15] However, the distribution of the cations within the unit cell depends on the nature of the II element.[16, 17] The CZTSe most stable phase is the chalcopyrite-like kesterite.[17,18] On the other hand, the most energetically favorable structure for CCTSe and probably CHTSe is that of stannite.[13, 17] In the stannite structure atoms arrange forming tetrahedral layers of electrically conductive [Cu_2Se_4] and electrically insulating [$ASnSe_4$] units. Such layered structure provides the material with considerable high Seebeck coefficients and relatively large hole mobilities,

while maintaining the intrinsically low thermal conductivities associated with complex quaternary structures. Moreover, the possibility to control the hole concentration of such multivalence quaternary compounds by replacing A by Cu atoms has been demonstrated as an effective strategy to further maximize their thermoelectric figures of merit (ZT).[9, 19] In this scenario, while the maximum ZT achieved for CZTSe was 0.45,[8] a 45 % increase, up to 0.7 eV, was obtained for CCTSe.[9] We hypothesize that by using a larger divalent ion such as Hg, an additional reduction of the thermal conductivity could be obtained, further increasing the material's ZT. Furthermore, while there is no systematic study of the thermoelectric properties of CHTSe, this material was reported to achieve very high Seebeck coefficients up to 1700 $\mu V\ K^{-1}$, thus pointing out its high potential as a thermoelectric material.[20]

Owing to the technological interest of I_2-II-IV-VI_4 semiconductors, the development of solution-based routes to produce I_2-II-IV-VI_4 nanoparticles has become a topic of high interest both from a fundamental and a technological point of view.[21-25] From the technological point of view, solution-processing and bottom-up assembly technologies offer advantages in terms of cost, yield and production scalability.[26-34] On the other hand, from a fundamental point of view, thermoelectric measurements offer an exciting platform to study the influence of nanoparticle composition, size and shape on the material electrical and thermal properties. Indeed, the crystal domain shape and especially size do matter in the thermoelectric field, being most of the currently best thermoelectric materials nanostructured.[35, 36] Such an interest in small structures certainly please the nanomaterials and nanotechnology community.

In the present work, we detail a colloidal synthesis route to produce CHTSe nanoparticles. The developed method allows preparing CHTSe nanocrystals at the gram scale and with controlled

composition. Nanoparticles were used as building blocks to produce bulk nanocrystalline materials, which thermoelectric properties were characterized in the temperature range from 300 to 700 K.

Table 1. Physical properties of Cu_2ASnSe_4 (A=Zn, Cd, Hg) tetrahedrally-coordinated compounds

	$Cu_2ZnSnSe_4$[8,11,13]	$Cu_2CdSnSe_4$[7,9,10,13]	$Cu_2HgSnSe_4$[13,20]
Density (Kg/m^3)	5689	5780	6514
Absorption coefficient	634	788	934
Band gap (eV)	1.00-1.44	0.89-0.96	0.17
Seebeck coefficient ($V K^{-1}$)	156-300	160-298	1700
Thermal conductivity ($Wm^{-1}K^{-1}$)	0.82-2.11	0.29-1.01	
Electrical Conductivity ($S m^{-1}$)	$2.25x10^4$-$8.10x10^4$	1,670-22,000	

2. Experimental

Chemicals: Copper (I) chloride (≥99 %, Sigma-Aldrich), mercury (II) chloride (Reag. Ph Eur, ACS, Merck Millipore), tin (IV) chloride pentahydrate (98 %, Strem), selenium (IV) oxide (99.8 %, Strem), hexadecylamine (HDA, 90 %, Aldrich) and octadecene (ODE, 90 %, Aldrich) were used as received without further purification. Solvents such as chloroform, and isopropanol were of analytical grade and obtained from various sources. All syntheses were carried out using standard airless techniques: a vacuum/dry argon gas Schlenk line used for the syntheses and an argon glove-box for storing and handling air and moisture-sensitive chemicals.

Selenium solution (ODE:Se): A 0.8 M SeO_2-ODE solution was obtained by dissolving SeO_2 (8.87 g, 80 mmol) in 100 mL of ODE under argon at 180 °C. Dissolution required around 5 h until a perfectly clear brownish-orange solution was obtained.

CHTSe nanoparticles: In a typical synthesis, CuCl (0.25 mmol), $SnCl_4 \cdot 5H_2O$ (0.125 mmol), $HgCl_2$ (0.25 mmol), 1.2 g of HAD (5 mmol) and 9 g of ODE were loaded into a four-neck flask and heated to 200 ºC at a rate of 17 ºC/min under an argon flow to produce a yellowish transparent solution. The solution was maintained at 200 ºC for 1 h for purification. Afterwards, temperature was raised to 285 ºC and then 4 mL of a 0.8 M SeO_2-ODE solution were injected. The solution was kept at 285 ºC for 5 min to allow the nanoparticles growth before it was rapidly cooled down. The resulting nanoparticles were isolated and purified using the standard solvent/non-solvent procedure with chloroform/isopropanol.

Characterization: Transmission electron microscopy (TEM) and high-resolution TEM (HRTEM) micrographs were obtained using a Jeol 2010F field-emission gun microscope with a 0.19 nm point- to-point resolution at 200 keV with an embedded Gatan image filter

for electron energy loss spectroscopy (EELS) analyses. Images were analyzed by means of Gatan Digital micrograph software. The powder XRD patterns were obtained with Cu Kα (λ = 1.5406 Å) radiation in a reflection geometry on a Bruker D8 operating at 40 kV and 40 mA. Scanning electron microscopy (SEM) was performed using a ZEISS Auriga with an energy dispersive X-ray spectroscopy (EDX) detector to study composition. Raman scattering measurements were obtained in backscattering geometry with dispersive spectrometer Jobin-Yvon LabRam HR 800, coupled to an optical microscope Olympus BXFM. Excitation was provided by an argon-ion laser operating at a wavelength of 532.0 nm with a low incident power to avoid thermal effects. X-ray power diffraction (XRD) analyses were carried out on a Bruker AXS D8 ADVANCE X-ray diffractometer with Cu Kα1 radiation (λ = 1.5406 Å).

CHTSe bulk nanocrystalline materials: CHTSe bulk nanomaterials were produced by the bottom-up assembly of CHTSe nanoparticles. To prepare the relatively large amounts of material needed for thermoelectric characterization, the synthesis procedure detailed above was straightforward scaled up using 6 times larger amounts of all precursor, surfactant and solvent. Nanoparticles were thoroughly purified by multiple precipitation and re-dispersion steps and they were finally dried under argon atmosphere. Afterward, the nanocrystals were heated to 500 ºC for 2 h under an argon flow inside a tube furnace. The obtained nanopowders were then pressed into 10 mm diameter and 1 mm thick disks under 2 tones of force. Pressure was applied for 5 min at room temperature. The relative densities of the obtained pellets were in the range 80-85 %.

Thermoelectric characterization: Seebeck coefficients and electrical conductivities were measured simultaneously using a Linseis - LSR 3 system. Analyses were carried out under

helium atmosphere. The Seebeck coefficient was obtained using a static DC method. The electrical conductivity was measured using a standard four probe technique. Thermal conductivity values were obtained from flash diffusivity measurements (Netzsch LFA-457 Microflash) using the mass density and the Dulong-Petit approximation to determine the specific heat capacity. The thermal conductivity was calculated as $\kappa = DC_pd$, where D is thermal diffusivity, C_p is heat capacity, and d is density.

3. Results and discussion

CHTSe nanoparticles were obtained by reacting the metal chlorides with a Se solution in ODE. Figure 1a shows representative TEM and HRTEM micrographs of CHTSe nanoparticles obtained by the above detailed procedure. The synthetic route reported here yielded nanoparticles with tetragonal shapes, average size of 14 ± 2 nm and narrow size distributions (inset Figure 1a). The overall composition of the nanoparticles, determined by EDX, was close to the stoichiometric one as observed by EDX. Further EELS analysis confirmed the 4 elements to be present in every single nanoparticle analyzed in approximately the same concentration and to be homogeneously distributed within each nanoparticle (Figure 2). HRTEM characterization (Figure 1a) showed the nanoparticles to have a tetragonal crystallographic structure with space group $I4_2m$. XRD analysis (Figure 3a) confirmed the CHTSe nanoparticles to have the tetragonal structure (JCPDS: 01-074-8343). Additional Raman scattering spectra was obtained to disregard the existence of secondary phases. The Raman spectrum of CHTSe showed three main peaks at 171 cm^{-1}, 189 cm^{-1} and 230 cm^{-1} (Figure 3c). In analogy with the well studied CZTSe case, we assigned the 171 cm^{-1} and the 189 cm^{-1} peaks to the two main A symmetry modes of the CHTSe tetragonal structure and the 238 cm^{-1} peak to one or two E/B symmetry modes.[37] No secondary

phases were obtained by either XRD or Raman characterization.

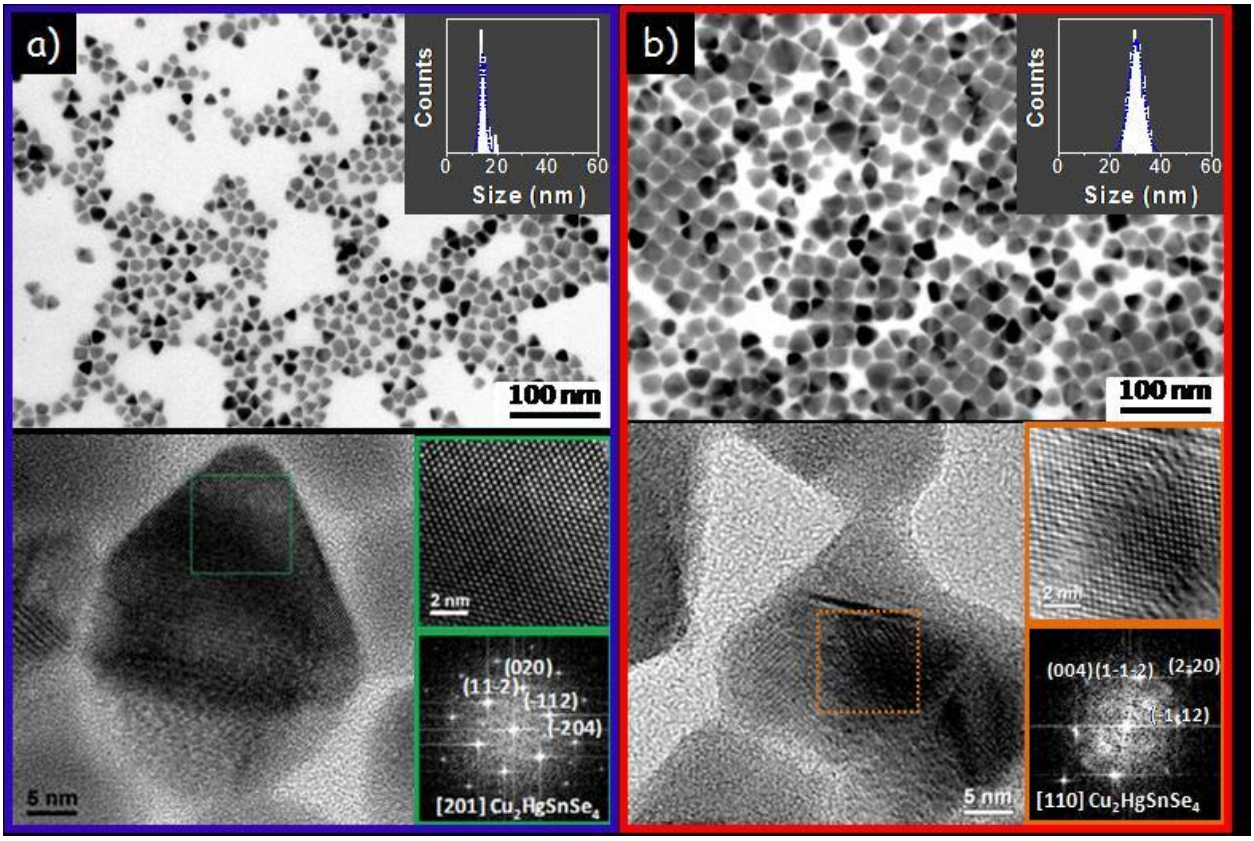

Figure 1. TEM and HRTEM micrographs of $Cu_2HgSnSe_4$ and $Cu_{2.3}Hg_{0.7}SnSe_{3.8}$ nanoparticles.

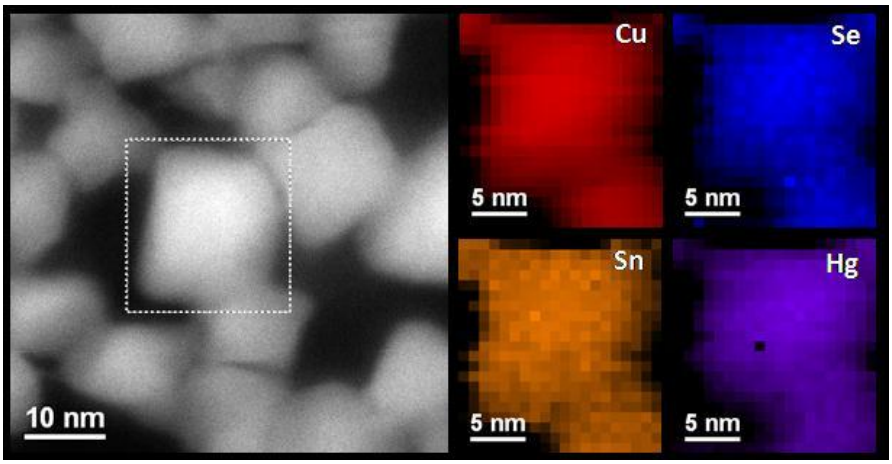

Figure 2. High Angle Annular Dark Field (HAADF) STEM image of a few CHTSe nanoparticles and a single nanoparticle EELS compositional map.

The carrier concentration of multivalence I_2-II-IV-VI_4 compounds can be modified by tuning the ratio of the different elements within the crystal structure. In particular, the partial substitution of monovalent Cu by divalent Hg allows increasing the hole concentration, shifting the Fermi level towards the valence band. This intrinsic doping strategy is especially convenient in bottom-up assembled nanomaterials, since the introduction of extrinsic dopants in colloidal nanoparticles is still an unsolved challenge. Cu-rich and Hg-poor nanoparticles were prepared by reducing the amount of $HgCl_2$ in the precursor solution. Figure 1b shows representative TEM micrographs of $Cu_{2.3}Hg_{0.7}Sn_{1.0}Se_{3.8}$ nanoparticles produced with a lower $HgCl_2$ concentration. Cu-rich nanoparticles were polycrystalline and were characterized by larger sizes, 30 ± 5 nm, but conserved their excellent monodispersity. We speculate that at an early growth stage tetrahedral nanoparticles are formed like in the stoichiometric composition. Twins at the surface of these tetrahedrons change the crystal growth direction and act as seeds for the growth of reversed tetrahedron. In this way, multi-tetrahedron nanoparticles are formed. We experimentally observed that in the Cu-rich precursor solution larger nanocrystal growth rates were obtained, thus accelerating the formation of larger nanocrystals and probably the dissolution of the smallest ones. Single-particle EELS analyses were performed to demonstrate that all nanoparticles contained the 4 elements and that they were homogeneously distributed across the particle. No secondary crystallographic phases were observed by either EELS, HRTEM, XRD or Raman spectroscopy.

Figure 3c displays the UV-vis spectrum of CHTSe nanoparticles. The measured optical band gap was close to 1.2 eV, much higher than the values theoretically calculated.

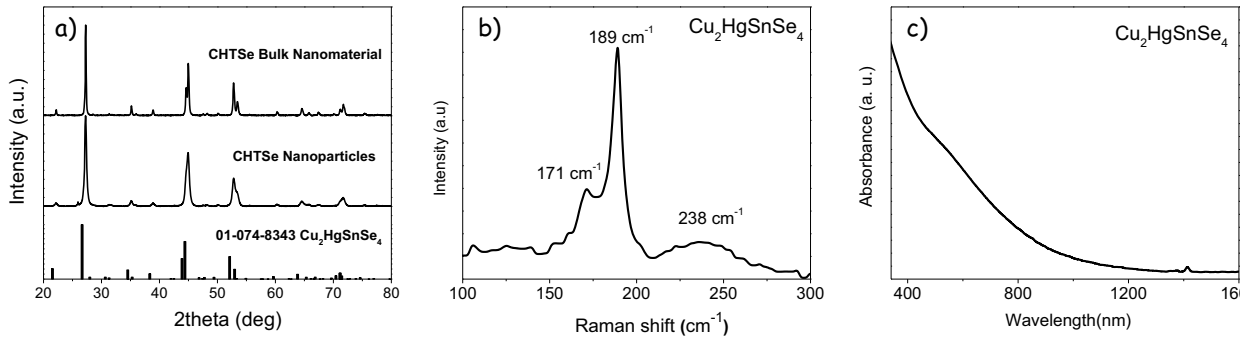

Figure 3. (a) XRD pattern of CHTSe nanoparticles and bulk nanomaterials after annealing at 500 ºC for 2 h. (b) Raman spectrum of CHTSe nanoparticles obtained using 532 nm excitation. (c) UV-vis spectrum of the CZTSe nanoparticles.

To characterize the thermoelectric properties of CHTSe nanomaterials, the described synthetic routes were scaled up to produce CHTSe nanoparticles at the gram scale. Macroscopic CHTSe nanomaterials were obtained from the bottom-up assembly of 1 g of colloidal CHTSe nanoparticles. After sintering, CHTSe nanoparticles were thoroughly purified, dried and annealed at 500 ºC for 2 h. The obtained CHTSe nanopowder was consolidated into dense disk-shaped pellets with 10 mm of diameter and 1 mm thickness using a hydraulic press. The relative densities of the samples obtained in these conditions were in the range 80-85 %. During this process, the CHTSe crystal domains underwent a factor 2.25 growth: from 14 nm to approximately 32 nm as calculated from the XRD pattern using Scherrer equation (Figure 3a). Upon heat treatment of the pellet, no additional secondary phases were observed (Figure 3a).

Figure 4 displays the electrical conductivity and Seebeck coefficient (S) of the CHTSe nanomaterials obtained from the bottom-up assembly of CHTSe nanoparticles. As expected, stoichiometric nanomaterials showed much lower electrical conductivities than Cu-rich CHTSe due to the large concentration of carriers introduced when replacing Hg^{2+} ions by Cu^{+}. The positive Seebeck coefficients measured from nanocrystalline pellet demonstrated the p-type

character of the obtained materials. Relatively high Seebeck coefficients were measured, especially for the stoichiometric material, which reached values up to 350 V K^{-1}. While much higher Seebeck coefficients were obtained for the stoichiometric compound, the much higher electrical conductivity of the Cu-rich material translated into higher power factors, thus only the non-stoichiometric sample was considered for further characterization. Figure 5 displays the thermal conductivity and dimensionless thermoelectric figure of merit ($ZT=S^2/$) for the $Cu_{2.3}Hg_{0.7}SnSe_{3.8}$ nanomaterial. Relatively low thermal conductivities, down to 0.42 $Wm^{-1}K^{-1}$, were obtained for this nanomaterial. These low thermal conductivities were related with the complex crystallographic structure of the quaternary compound, the point defects introduced by the replacement of Hg by Cu, the large density of crystallographic interfaces, and the sample porosity. With this very preliminary optimization of the material composition, figures of merit up to 0.20 at 450 ºC were calculated.

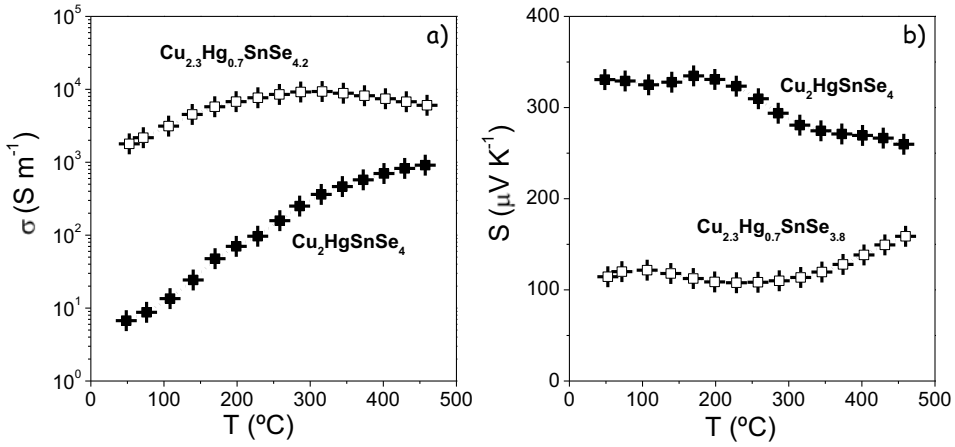

Figure 4. (a) Electrical conductivity and (b) Seebeck coefficient (S) of the CHTSe nanomaterials obtained from the bottom-up assembly of CHTSe NCs.

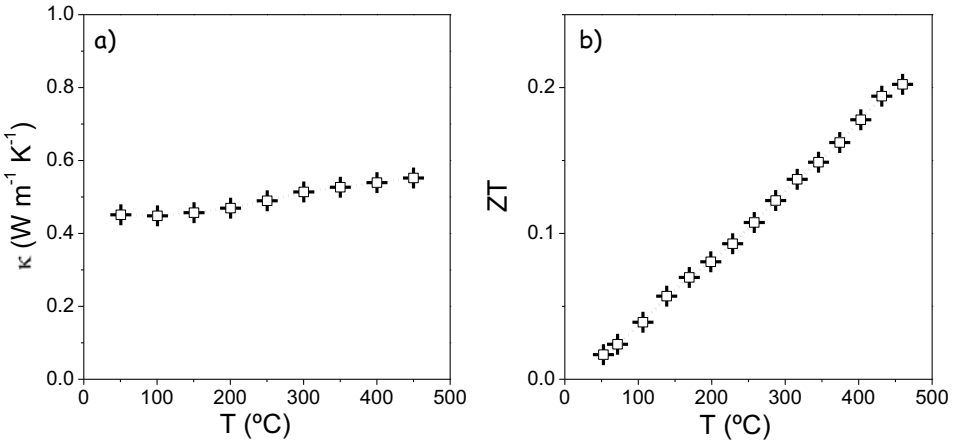

Figure 5. (a) Thermal conductivity and (b) thermoelectric figure of merit (ZT) of the CHTSe nanomaterials obtained from the bottom-up assembly of $Cu_{2.3}Hg_{0.7}SnSe_{3.8}$ nanoparticles.

Ab initio density of states calculations was performed to better understand the origin of the high Seebeck coefficients and clarify the mechanisms behind the variation of the thermoelectric properties with the nanocrystal composition. Our density of states calculations consistently revealed a gradual downshift of the Fermi level towards the valence band when replacing Hg by Cu ions (Figure 6a). In Figure 6b, the contribution of each element to the total CHTSe density of states is shown. The main contribution to the valence band maximum (VBM) comes from Cu. Figures 6c and 6d show the localization of the states contributing to the VBM and those contributing to the conduction band minimum (CBM), respectively. Notice how, in such a quaternary crystal structure, the states contributing to the electrical conductivity are strongly localized in Cu-Se slabs (hybridization of Cu3d Se4p orbitals). On the other hand, Hg and Sn introduce deep levels inside the valence band, thus not contributing to the electrical conductivity. Therefore, CHTSe may be regarded as composed of tetrahedral [Cu_2-Se_4] electrically conductive slabs separated by tetrahedral [Hg-Sn-Se_4] electrically insulating slabs. Such layered structure is

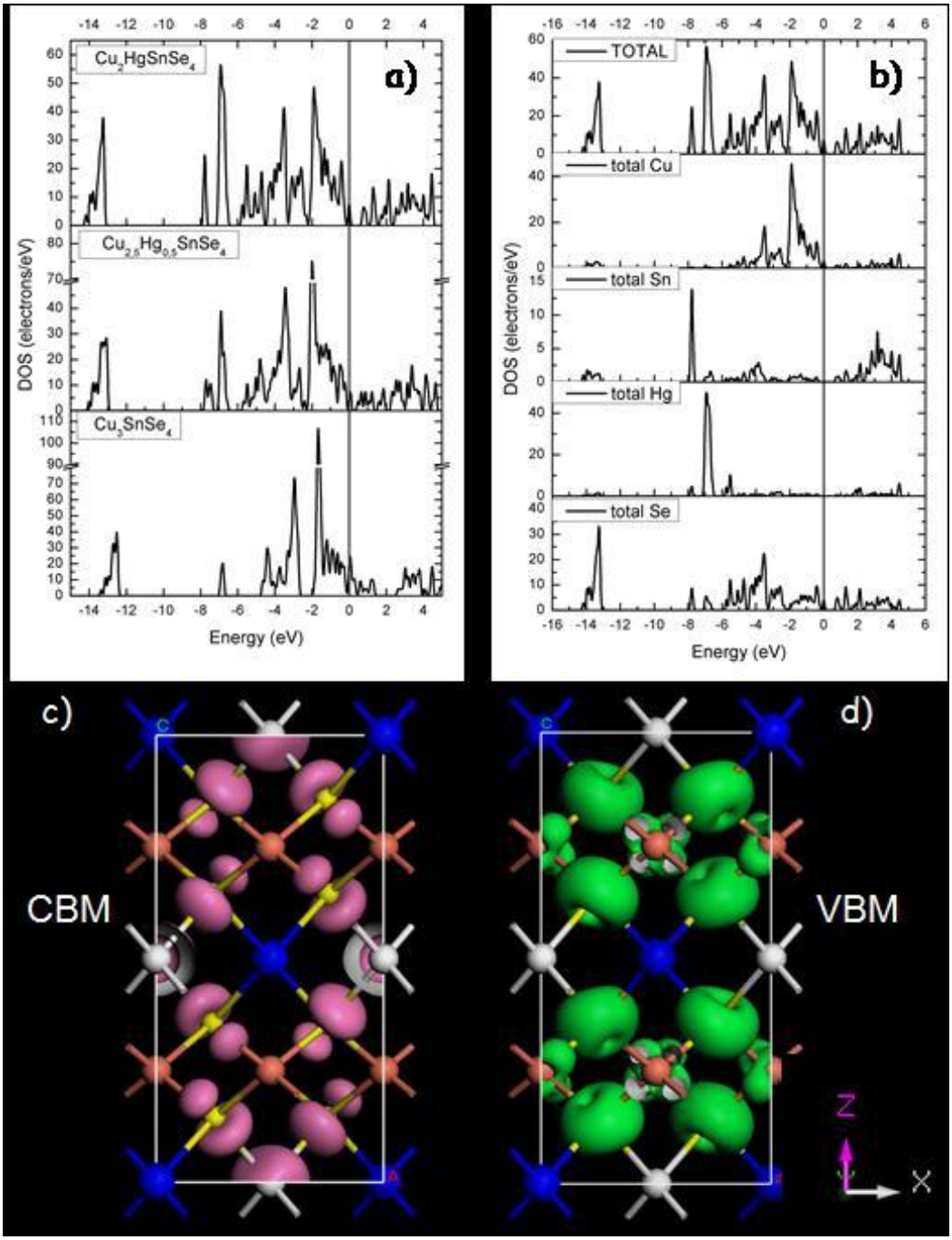

Figure 6. (a) Total density of states for $Cu_2HgSnSe_4$, $Cu_{2.5}Hg_{0.5}SnSe_4$ and Cu_3SnSe_4. (b) Total density of states and projected densities corresponding to the different elements within the $Cu_2HgSnSe_4$ compound. (c) Localization of the orbitals contributing to the conduction band minimum (CBM). (d) Localization of the orbitals contributing to the valence band maximum (VBM).

equivalent to that observed on CCTSe. The localization of the conductive bands in slabs preserves the hole mobilities from being influenced by the crystal structure complexity, thus permitting the concurrence of relatively low thermal conductivities and high electrical conductivities. At the same time, the states contributing to the CBM, mostly associated to Se, are distributed across the whole unit cell. Hence, electron mobilities are more perturbed by the whole cell complexity. Such differential influence of the crystal structure on each charge carrier type should result in relatively high hole-to-electron mobility ratios, which partially explains the material's high Seebeck coefficient.

4. Conclusions

In summary, we detailed a synthetic procedure to produce CHTSe nanocrystals with narrow size distribution and controlled composition. Furthermore, the thermoelectric properties of the nanomaterials obtained after carefully washing the nanocrystals and pressing them into pellets were characterized. By partial replacement of Hg ions by Cu ions, the material's electrical conductivity could be tuned. ZT values up to 0.2 were obtained for the bottom-up assembly of $Cu_{2.3}Hg_{0.7}SnSe_{3.8}$ nanoparticles.

Acknowledgements

The research was supported by the European Regional Development Funds (ERDF, "FEDER Programa Competitivitat de Catalunya 2007-2013"). A. S. thanks the Catalan Government, Agència de Gestió d'Ajuts Universitaris i de Recerca (AGAUR), for financial support through the Beatriu i Pinos program.

References

(1) Sevik, C.; Cagin, T. *Appl. Phys. Lett.* **2009**, *95 (11)*, 112105.

(2). Mitzi, D. B.; Gunawan, O.; Todorov, T. K.; Wang, K.; Guha, S. *Sol. Energ. Mat. Sol. C.* **2011**, *95*, 1421-1436.

(3) Wang, J. J.; Hu, J. S.; Guo, Y. G.; Wan, L. J. *NPG. Asia. Mater.* **2011**, *4*, e2.

(4) Matsushita, H.; Maeda, T.; Katsui, A.; Takizawa, T. *J. Cryst. Growth.* **2000**, *208*, 416-422.

(5) Todorov, T. K.; Tang, J.; Bag, S.; Gunawan, O.; Gokmen, T.; Zhu, Y.; Mitzi, D. B. *Adv. Energy. Mater.* **2013**, *3*, 34-38.

(6) Barkhouse, D. A. R.; Gunawan, O.; Gokmen, T.; Todorov, T. K.; Mitzi, D. B. *Progress in Photovoltaics: Research and Applications.* **2012**, *20 (1)*, 6-11.

(7) Liu, M. L.; Chen, I. W.; Huang, F. Q.; Chen, L. D. *Adv. Mater.* **2009**, *21 (37)*, 3808-3812.

(8) Liu, M. L.; Huang, F. Q.; Chen, L. D.; Chen, I. W. *Appl. Phys. Lett.* **2009**, *94 (20)*, 202103.

(9) Ibáñez, M.; Cadavid, D.; Zamani, R.; García-Castelló, N.; Izquierdo-Roca, V.; Li, W.; Fairbrother, A.; Prades, J. D.; Shavel, A.; Arbiol, J.; Pérez-Rodríguez, A.; Morante, J. R.; Cabot, A. *Chem. Mater.* **2012**, *24 (3)*, 562-570.

(10) Fan, F. J.; Yu, B.; Wang, Y. X.; Zhu, Y. L.; Liu, X. J.; Yu, S. H.; Ren, Z. *J. Am. Chem. Soc.* **2011**, *133 (40)*, 15910-15913.

(11) Fan, F. J.; Wang, Y. X.; Liu, X. J.; Wu, L.; Yu, S. H. *Adv. Mater.* **2012**, *24*, 6158-6163.

(12) Sevik, C.; Çağın, T. *Phys. Rev. B* **2010**, *82* (4), 045202.

(13) Olekseyuk, I. D.; Gulay, L. D.; Dydchak, I. V.; Piskach, L. V.; Parasyuk, O. V.; Marchuk, O. V. *J. Alloys. Compd.* **2002**, *340 (1-2)*, 141-145.

(14) Shafer, C.; Nitsche, R. *Mat. Res. Bull.* **1974**, *9 (5)*, 645-654.

(15) Pamplin, B. *Prog. Crystal. Growth. Charact.* **1981**, *3,* 179-192.

(16) Chen, S.; Gong, X. G.; Walsh, A.; Wei, S. H. *Appl. Phys. Lett.* **2009**, 94 (4), 041903.

(17) Chen, S.; Gong, X. G.; Walsh, A.; Wei, S. H. *Phys. Rev. B* **2009**, *79 (16)*, 165211.

(18) Li, J.; Mitzi, D. B.; Shenoy, V. B. *ACS. Nano.* **2011***, 5* (11), 8613-8619.

(19) Ibáñez, M.; Zamani, R.; Lalonde, A.; Cadavid, D.; Li, W.; Shavel, A.; Arbiol, J.; Morante, J. R.; Gorsse, S.; Snyder, G. J.; Cabot, A. *J. Am. Chem. Soc.* **2012**, *134 (9)*, 4060-4063.

(20) Hirai, T.; Kurata, K.; Takeda, Y. *Solid. State. Electron.* **1967**, *10*, 975-981.

(21) Shavel, A.; Arbiol, J.; Cabot, A. *J. Am. Chem. Soc.* **2010**, *132*, 4514-4515.

(22) Shavel, A.; Cadavid, D.; Ibáñez, M.; Carrete, A.; Cabot, A. *J. Am. Chem. Soc.* 2012, *134*, 1438-1441.

(23) Ibáñez, M.; Zamani, R.; Li, W. H.; Shavel, A.; Arbiol, J.; Morante, J. R.; Cabot, A. *Cryst. Growth. Des.* **2012**, *12 (3)*, 1085-1090.

(24) Singh, A.; Geaney, H.; Laffir, F. R.; Ryan, K. M. *J. Am. Chem. Soc.* **2012**, *134*, 2910-2913.

(25) Aldakov, D.; Lefrançois, A.; Reiss, P. *J. Mater. Chem. C* **2013**, *1*, 3756-3776.

(26) Ibáñez, M.; Guardia, P.; Shavel, A.; Cadavid, D.; Arbiol, J.; Morante, J. R.; Cabot, A. *J. Phys. Chem. C* **2011**, *115 (16)*, 7947-7955.

(27) Li, W. H.; Zamani, R.; Rivera-Gil, P.; Pelaz, B.; Ibáñez, M.; Cadavid, D.; Shavel, A.; Alvarez-Puebla, R. A.; Parak, W. J.; Arbiol, J.; Cabot, A. *J. Am. Chem. Soc.* **2013**, *135*, 7098-7101.

(28) Li, W. H.; Zamani, R.; Ibáñez, M.; Cadavid, D.; Shavel, A.; Morante, J. R.; Arbiol, J.; Cabot, A. *J. Am. Chem. Soc.* **2013**, *135*, 4664-4667.

(29) Li, W. H.; Shavel, A.; Guzman, R.; Fan, J.; Cadavid, D.; Ibáñez, M.; Arbiol, J.; Cabot, A. *Chem. Commun.* **2011**, *47*, 10332-10334.

(30) Kovalenko, M. V.; Scheele, M.; Talapin, D. V. *Science* **2009**, *324*, 1417-1420.

(31) Ford, G. M.; Guo, Q.; Agrawal, R.; Hillhouse, H. W. *Chem. Mater.* **2011**, *23 (10)*, 2626-2629.

(32) Guo, Q.; Ford, G. M.; Yang, W. C.; Walker, B. C.; Stach, E. A.; Hillhouse, H. W.; Agrawal, R. *J. Am. Chem. Soc.* **2010**, *132 (49)*, 17384-17386.

(33) Riha, S. C.; Parkinson, B. A.; Prieto, A. L. *J. Am. Chem. Soc.* **2009**, *131 (34)*, 12054-12055.

(34) Guo, Q.; Hillhouse, H. W.; Agrawal, R. *J. Am. Chem. Soc.* **2009**, *131 (33)*, 11672-11673.

(35) Dresselhaus, M. S.; Chen, G.; Tang, M. Y.; Yang, R. G.; Lee, H.; Wang, D. Z.; Ren, Z. F.; Fleurial, J. P.;Gogna, P. *Adv. Mater.* **2007**, *19 (8)*, 1043-1053.

(36) Vineis, C. J.; Shakouri, A.; Majumdar, A.; Kanatzidis, M. G. *Adv. Mater.* **2010**, *22 (36)*, 3970-3980.

(37) Amiri, N. B. M.; Postnikov, A. *J. Appl. Phys.* **2012**, *112 (3)*, 033719.